SAINT-PETERSBURG UNIVERSITY

Timoshen Kirill Aleksandrovich

Films of fullerene C60 and its derivatives at the liquid-gas interface

Scientific specialty: 1.4.10. Colloid chemistry

Thesis is submitted for the degree of Candidate of chemistry sciences
Translation from Russian

Scientific supervisor:
Doctor of chemical sciences
Noskov B.A.

Saint Petersburg
2024

Table of contents

Introduction

Actuality. Fullerenes have unique properties and can be used in industry, for example, in micro- and optoelectronics, for modifying concrete, paints, lubricants, or as polymer fillers [1–19]. Also, the results of many studies have shown that fullerenes can be used in medicine as antimicrobial, antitumor agents and enzyme inhibitors [20–28]. Another promising area of application of fullerenes in medicine may be targeted delivery of drugs in a living organism. [29–32].

One of the problems when using fullerenes is their strong tendency to aggregate in aqueous systems, which makes it difficult, in particular, to obtain a homogeneous monolayer on the surface of water [33–35]. The Langmuir-Blodgett method, used to transfer films onto a solid substrate and form a regular structure, is inapplicable in this case, which makes it difficult to use for industrial purposes. The difficulty of using fullerenes for medical purposes is their extremely low solubility in water [36]. For fullerene C60 it is $1{,}3 \times 10^{-13}$ (г/л) at 298 K [37]. The concentration of fullerenes in aqueous systems can be increased by creating water-soluble complexes where fullerenes are placed in a matrix of amphiphilic compounds [33]. For this purpose, complexes of fullerenes with polymers are usually used. [38]. Chemical modification is also used when hydrophilic fragments are added to fullerene molecules to form covalent bonds [39]. To date, various fullerene derivatives have been synthesized, containing, for example, hydroxyl [40], carboxyl groups, fragments of crown ethers, calixarenes, oligopeptides, polyethylene glycols, amphiphilic polymer chains (conjugates of fullerenes and amphiphilic polymers) [41]. In addition, a number of studies are devoted to the production of fullerene microaggregates of various shapes [42,43].

Due to the increasing number of applications of fullerenes, there is a need to form thin organized films of these molecules. Such films must be stable and homogeneous. This can be achieved by forming adsorption or deposited films of water-soluble fullerene derivatives, as well as mixed films of fullerene with amphiphilic substances. Such systems can be used to simulate the interaction of fullerenes and their derivatives with biological objects, for example, with biological membranes. On the other hand, data on the properties of films of fullerene derivatives, as well as films of fullerene complexes with amphiphilic polymers on a water surface, are necessary for the development of technologies using the Langmuir-Blodgett method to create regular structures on a solid surface. At the moment, information about the

structure of such films and the kinetics of relaxation processes in these systems turns out to be rather scarce. As far as is known from the literature, films of fullerene microaggregates on a water surface have not been studied to date.

Purpose and tasks of the work. The purpose of this work is to partially fill the above-mentioned gap in existing knowledge about the properties of aqueous systems containing fullerenes and their derivatives, i.e. in determining the properties of films of fullerene C_{60}, its derivatives, mixed films of C_{60} with amphiphilic substances and microaggregates of fullerene C_{60} of various shapes on a water surface.

To achieve this goal, the following tasks were set:

1. Determination of surface pressure and dynamic elasticity of films of fullerene derivatives and its mixtures with amphiphilic polymers on a water surface;
2. Determination of the mechanism of adsorption of water-soluble fullerene derivatives;
3. Determination of the morphology of surface films of fullerene C_{60}, its derivatives and mixed films containing fullerene;
4. Assessment of changes in the microscopic structure of films during their compression-tension.
5. 5. Determination of the properties of films of C_{60} fullerene microaggregates on a water surface.

The scientific novelty of the work. For the first time, the properties and morphology of adsorption films of carboxylated and polyhydroxylated derivatives of C_{60} fullerene, its mixed films with two amphiphilic polymers, as well as deposited films of microrods and microtubes of C_{60} fullerene on an aqueous surface were determined. It is shown that, although the adsorption films of the studied fullerene derivatives are macroscopically homogeneous, they consist of interconnected nanoaggregates. For solutions of fullerenol $C_{60}(OH)_{20}$, an anomalously high dynamic surface elasticity (~ 300 mN/m) was found, which decreases with an increase in the number of hydroxyl groups in the molecule. Carboxyfullerene, unlike hydroxyfullerenes, is characterized by high surface activity and forms liquid-like layers at the interface. It is shown that the mixed layer of C_{60} fullerene/amphiphilic polymer at low surface pressures, below the characteristic value corresponding to the displacement of the polymer into the subphase, consists of two immiscible surface phases. The high stability of the fullerene

layer at high surface pressures up to a surface pressure of ~ 70 mN/m is associated with the hydroxylation of fullerene molecules in contact with water.

The theoretical and practical significance of the work lies, first of all, in determining the properties of systems that model the behavior of C60 fullerene and its derivatives in biological membranes. Although many medical applications of fullerenes involve the transport of these substances across cell membranes, the mechanism of this process has not yet been studied. The results obtained on the kinetics of adsorption of fullerene derivatives, on the surface activity of these substances and on the interaction of fullerene with polymers at the interface provide information necessary to determine the mechanism of transfer of fullerene and its derivatives in biological systems and, thereby, to assess the effectiveness of fullerene-based drugs. In addition, the resulting surface films of fullerene derivatives on a water surface can be used to create regular Langmuir–Blodgett films of a given thickness for optical devices.

Thesis structure. The dissertation includes an introduction, literature review, experimental part, discussion of results and conclusion. The introduction reveals the relevance of the research, characterizes the degree of scientific development of the topic, defines the purpose and objectives of the work, and reveals the theoretical and practical significance. The literature review describes the chemical and physical properties of fullerenes, their classification, behavior in aqueous solution, considers the properties of films of pure C_{60} fullerene at the air/gas interface, its interaction with amphiphilic polymers, as well as the production of its aggregates in the form of rods and nanotubes. The experimental part describes methods for obtaining fullerene derivatives and its aggregates, their characterization, methods for forming surface films, selecting samples to study their morphology, methods for determining the surface properties and structure of deposited and adsorption films. Chapter 3, “Surface properties of solutions of C_{60} fullerene derivatives,” describes the properties of adsorption films of chemically modified fullerene. It has been shown that derivatives with hydroxyl groups form a macroscopically homogeneous adsorption layer with high dynamic surface elasticity, but their surface activity is low. In this case, the layer turns out to be quite fragile and contains a large number of surface microaggregates. The surface activity of a fullerene derivative with carboxyl groups is much higher, and the adsorption layer is less fragile. Chapter 4, “Properties of films of a mixture of C_{60} fullerene with amphiphilic polymers and films of C_{60} microaggregates on a water surface,” discusses the properties of deposited films

containing unmodified fullerene and films of C_{60} fullerene microaggregates. The properties of films of unmodified C_{60} fullerene at the water-air interface indicate its strong adhesion to water. The applied layers can withstand high surface pressure. The dynamic elasticity of the films reaches very high values (~ 400 mN/m). The addition of polymers leads to a change in surface properties and the formation of a more stable film. The properties of deposited films of fullerene microaggregates strongly depend on the shape of the aggregates. The text of the dissertation partially uses materials from the final qualifying work of the author of the dissertation (level of education - graduate school).

Methodology and research methods. To study the structure, surface properties and adsorption kinetics, the work used classical methods of surface tensiometry together with dilatational surface rheology, as well as ellipsometry and various types of microscopy: Brewster angle microscopy, atomic force microscopy, scanning electron microscopy, transmission electron microscopy.

Approbation of the research. All results obtained within the framework of the dissertation are new. Their reliability is ensured by the use of reliable experimental methods, repeatedly tested in the study of various classes of systems. The results of the work were published in four articles and were presented in the form of three oral and two poster presentations at international and all-Russian scientific conferences:

- K.A. Timoshen, B.A. Noskov, A.V. Akentiev, N.S. Chirkov, SY Lin, V.P. Sedov, A.A. Borisenkova, I.M. Dubovsky, V.T. Lebedev / “Dynamic surface properties of Fullerenol solutions”, XXII International Conference on Chemical Thermodynamics in Russia (RCCT-2019), Saint Petersburg, Russia, 19-23 June 2019.
- Timoshen K.A., Noskov B.A., Akentiev A.V., Chirkov N.S., Lin S.Y., Sedov V.P., Borisenkova A.A., Dubovsky I.M., Lebedev V.T. / “Rheological properties of fullerenol adsorption layers”, Mendeleev 2019, Petergof, Russia, 9-13 September 2019.
- Тимошен К.А., Акентьев А.А., Носков Б.А. / “Динамические поверхностные свойства смешанных пленок полимер/фуллерен C_{60} на границе жидкость/газ”, Полимеры в стратегии научно-технического развития РФ "Полимеры-2020", Тверь, Россия, 9 - 13 ноября 2020.

- Носков Б.А., Тимошен К.А., Быков А. Г. / “ Динамические поверхностные свойства ленгмюровских пленок фуллерена С60 и его смесей с амфифильными полимерами”, Супрамолекулярные стратегии в химии, биологии и медицине: фундаментальные проблемы и перспективы, Казань, Россия, 3 - 6 октября 2022.
- B.A. Noskov, K.A. Timoshen, A.G. Bykov / “Dynamic surface properties of fullerene mixed films with polymers”, p. 275. XXIII International Conference on Chemical Thermodynamics in Russia, Kazan, Russia, August 22-27 2022.

Publications:

- B.A. Noskov, K.A. Timoshen, A. V. Akentiev, N.S. Chirkov, I.M. Dubovsky, V.T. Lebedev, S.Y. Lin, G. Loglio, R. Miller, V.P. Sedov, A.A. Borisenkova, Dynamic Surface Properties of Fullerenol Solutions, Langmuir. 35 (2019) 3773–3779.
- V. Akentiev, S.B. Gorniaia, N.A. Isakov, V.T. Lebedev, O.Y. Milyaeva, V.P. Sedov, K.N. Semenov, K.A. Timoshen, B.A. Noskov, Surface properties of fullerenol C60(OH)20 solutions, J Mol Liq. 306 (2020).
- B.A. Noskov, K.A. Timoshen, A.G. Bykov, Langmuir layers of fullerene C60 and its mixtures with amphiphilic polymers, J Mol Liq. 320 (2020) 114440.
- K.A. Timoshen, A.D. Khrebina, V.T. Lebedev, G. Loglio, R. Miller, V.P. Sedov, B.A. Noskov, Dynamic surface properties of carboxyfullerene solutions, J Mol Liq. 372 (2023) 121174.

Thesis statements to be defended.

1. Features of dilatation rheological properties of adsorption films of chemically modified fullerene derivatives and deposited films of mixtures of C_{60} fullerene with amphiphilic polymers on a water surface;
2. Interpretation of kinetic dependences of dynamic surface elasticity of solutions of chemically modified fullerene derivatives and its mixtures with amphiphilic polymers;
3. Mechanism of formation of adsorption films on the surface of solutions of chemically modified fullerene derivatives;
4. Features of the morphology of films of chemically modified fullerene derivatives and its mixtures with amphiphilic polymers on the water surface.
5. Mechanism of collapse of deposited fullerene films on a water surface at high surface pressures.

6. Properties of deposited films of nanotubes and fullerene microrods at the water-air interface.

Main scientific results. This work shows that the surface activity of $C_{60}(OH)_{30}$ is low. Molecules of fullerenol $C_{60}(OH)_{30}$ form a macroscopically homogeneous adsorption layer at the solution-air interface with high dynamic surface elasticity, which is characterized by a nonlinear response even to small amplitude fluctuations in the surface area. The surface properties of its solutions are very sensitive to small mechanical disturbances of the surface. The adsorption layer at the microlevel is heterogeneous and contains surface microaggregates consisting of two or three layers of fullerenol molecules. Surface $C_{60}(OH)_{30}$ aggregates are not adsorbed from the bulk phase, but are formed in the surface layer. The slow adsorption of fullerenols is determined by the electrostatic adsorption barrier.

The surface elasticity of $C_{60}(OH)_{20}$ solutions turns out to be significantly higher than that of $C_{60}(OH)_{30}$ solutions. Small changes in surface tension are accompanied by a large increase in dynamic surface elasticity. Adsorption of $C_{60}(OH)_{20}$ occurs faster due to the lower charge of the molecules and, therefore, a lower adsorption barrier. The adsorption layer of $C_{60}(OH)_{20}$ is more fragile than the layer of $C_{60}(OH)_{30}$. The adsorption layer of $C_{60}(OH)_{20}$ is heterogeneous on a microscopic scale and contains surface aggregates.

The surface activity of $C_{60}(C(COOH)_2)_3$ significantly exceeds the surface activity of fullerenols. The adsorption of carboxyfullerene occurs much faster; the kinetic dependences of surface properties do not have an induction period. The dynamic surface elasticity of carboxyfullerene solutions changes within several hours after surface formation, while the surface tension remains almost unchanged after an initial rapid decrease. The adsorption layer of carboxyfullerene is less fragile than the adsorption layers of fullerenols, and its properties change to a lesser extent under external mechanical influences. The adsorption layer $C_{60}(C(COOH)_2)_3$ contains numerous surface aggregates, the size and number of which increase during the adsorption process.

The properties of deposited films of unmodified C_{60} fullerene at the water-air interface indicate its strong adhesion to water. The dynamic elasticity of the films reaches very high values. Fullerene film consists of multilayers.

The dependences of dynamic elasticity on surface pressure of mixed deposited C_{60} films with amphiphilic polymers PVP and PNIPAM have two local maxima and can be divided into two parts, for which the surface elasticity is determined by the polymer or fullerene, respectively. The properties of deposited C_{60} and C_{60}/polymer films at high surface pressure are due to the strong adhesion of the layers to water.

The properties of deposited layers of fullerene nanotubes on an aqueous surface are very different from the properties of fullerene deposited from a solution in toluene. In the first case, the dynamic surface elasticity turns out to be several times lower. A plateau region appears on compression isotherms, corresponding to a two-dimensional phase transition.

Chapter 1 Literature review

1.1 Properties of fullerenes

The fullerene molecule consists entirely of carbon atoms, forming a unique structure in the form of, for example, a hollow sphere, ellipsoid or tube. The most famous and well-studied fullerene is Buckminsterfullerene, also known as C_{60}, which consists of 60 carbon atoms arranged in a football shape with hexagonal and pentagonal rings.

This class of compounds was discovered in 1985 by a team of researchers including Harold Croteau of the University of Sussex, James R. Heath, Sean O'Brien, Robert Curl and Richard Smalley of Rice University [44]. They discovered these molecules in the soot left behind after carbon evaporates in a helium atmosphere using mass spectrometry. The soot spectrum consisted of discrete peaks corresponding to molecules containing sixty and seventy carbon atoms, which they called "buckyballs." This name is given in honor of the American architect Buckminster Fuller, who used pentagons and hexagons in the design of a geodesic dome. The C60 molecule was named "Buckminsterfullerene". The suffix "ene" was added to indicate that the carbon atoms in fullerene molecules bond to only three other atoms instead of the usual four. Eventually, the name "fullerene" came to refer to the entire family of molecules. For the discovery of fullerenes, Kroto, Curl and Smalley were awarded the Nobel Prize in Chemistry in 1996.

Fullerene C_{60} is an allotropic modification of carbon with a mass of 720 amu. In this molecule, the carbon atoms are located at the vertices of hexagons and pentagons, forming a spherical surface.

The most common fullerene is Buckminsterfullerene C_{60} of sixty carbon atoms. It resembles a soccer ball, consisting of 12 pentagons and 20 hexagons [44]. Fullerenes satisfy Euler's theorem, according to which a polyhedron having a closed structure of pentagons and hexagons must contain exactly 12 pentagons. Following this rule, the smallest stable fullerene is C60. The C_{60} molecule has high symmetry [45]. There are two types of bonds in fullerene: C5-C5 single bonds (1.45 ± 0.015 Å) in pentagons and C5-C6 double bonds (1.40 ± 0.015 Å) in hexagons [46]. Each carbon atom forms a bond with three neighboring atoms with sp2 hybridization. The set of orbitals is centered in the xy plane. Thus, delocalized pi electrons stabilize the spheroid structure through resonance [47]. The molecule has a diameter of about 7

Å. C_{60} condenses to form a solid of loosely bound molecules. This crystalline state is called fullerite. In its solid state it is a yellow powder that turns pink when dissolved in toluene. When exposed to strong ultraviolet radiation, C_{60} polymerizes, forming bonds between adjacent beads. In the polymerized state, C_{60} is no longer soluble in toluene [48]. Chemically, the fullerene molecule is quite stable. Temperatures above 1000 °C are required to destroy it. When fullerenes are heated to 1500 °C in the absence of oxygen, they transform into graphite.

In addition to C_{60}, fullerenes containing from 30 to 980 carbon atoms with different properties and applications are known. As hexagons are added or removed from the basic structure of a soccer ball, the molecule begins to lose its roundness. The C_{70}, which has 25 hexagons, is shaped more like a rugby ball. With loss of roundness comes loss of stability. In addition to C_{60} and C_{70}, C_{76}, C_{78}, C_{84}, and C_{86} were isolated and studied in detail. Fullerenes have extremely low solubility in water [37]. Good solvents for them are carbon disulfide, o-dichlorobenzene, toluene and xylene. [49,50]. The color of fullerene solutions is explained by the electronic π-π transition.

Insolubility in aqueous media is considered the main obstacle to many applications of fullerenes. There are several methods for increasing their concentration in the aqueous phase: preparation of two-phase colloidal solutions, synthesis of fullerene derivatives, fullerene polymers, encapsulation in special carriers (cyclodextrins, calixarenes, polyvinylpyrrolidone, micelles, liposomes and some others) [51].

1.2 Classification of fullerenes

There are many different classifications of fullerenes. Among them, fullerenes doped with alkali metal atoms can be distinguished. C_{60} easily forms compounds with electron donors because it has high electronegativity. In this case, alkali metal atoms fill the space between the C_{60} atoms and donate a valence electron to the neighboring molecule. If the alkali metal atoms are potassium (K) or rubidium (Rb), then the corresponding compounds are superconductors, for example, K_3C_{60}, Rb_3C_{60} [52].

If other atoms are confined within the hollow shell of fullerenes, this results in the formation of compounds known as endohedral fullerenes. When the atom contained inside is a metal, they are called metallofullerenes. Most endohedral materials produced are composed of C82, C84 or even higher-grade fullerenes [53].

Of all types of fullerene derivatives, exohedral fullerenes are of the greatest practical interest. These are derivatives of fullerenes, to which additional atoms and groups of atoms are attached outside the fullerene framework. Since fullerenes have a conjugated π-system of electrons, two main types of primary chemical transformations are possible on the surface of the molecule: addition reactions and redox reactions leading to covalent exohedral adducts and salts, respectively [54].

Another fundamental group of modified fullerenes is heterofullerenes. They are heteroanalogues of fullerenes C60 and higher, where one or more carbon atoms of the framework are replaced by heteroatoms, for example, trivalent nitrogen or boron atom [55]. The simplest derivative of nitrogen-containing fullerene is the C59N fullerene and its dimer $(C_{59}N)_2$.

Another important byproduct of fullerenes is carbon nanotubes [56,57]. These systems consist of graphite sheets rolled seamlessly into cylinders. The diameter of nanotubes varies from 0.4 to 3 nm for single-walled nanotubes (SWNTs) and from 1.4 to 100 nm for multi-walled nanotubes (MWNTs) [58,59]. Nanotubes are also quite rigid and have high tensile strength.

1.3 Hydration of fullerenes and the formation of their aqueous dispersions

The processes of interaction between C_{60}-C_{60} particles and adsorption of C_{60} on various surfaces are of fundamental importance. The chemical nature of the surface affects the adsorption of C_{60} [60]. The interaction of fullerene with surrounding water molecules and other chemicals leads to its transformation from a hydrophobic molecule into a highly negatively charged polar form, which is called Aqu/C_{60} [61,62]. During the formation of Aqu/C_{60}, negatively charged colloidal fullerene aggregates are formed after stirring in water for a certain time [63].

Unlike the surface tension of a liquid, when measuring the surface energy of a solid body, difficulties arise due to the low accuracy of determining this quantity at the boundary of the solid body and the fluid phase. Young's equation relates surface energy to macroscopic contact angles, which can be easily measured using various liquids. Contact angle measurement provides an accurate and repeatable indication of surface properties. For powdered materials such as C_{60}, directly determining the contact angle of liquids is

problematic because powders do not have a smooth surface to accommodate liquid droplets. Consequently, contact angle measurements provide only an apparent average value for heterogeneous powder materials.

When C_{60} is dispersed in water, kinetically stable particles ranging in size from several nanometers to hundreds of nanometers in diameter are formed [64,65]. These clusters of aggregates consist of smaller particles with a diameter of about 4 nm, which contain approximately 33 C_{60} molecules. These aggregates are believed to represent the most stable structures among hydrated particles due to their lowest chemical potential. The value of free energy of hydration ΔGpw for such units is 90,5 mJ/m2 [66]. Hydrophobic C_{60} particles tend to interact with water, which is confirmed by the significant free energy of hydration. The strong affinity of water molecules for C_{60} powder is experimentally confirmed by adsorption/desorption isotherms of water vapor [67]. When large particles enter water, they are broken down into smaller aggregates. Simultaneous interactions of C_{60}-C_{60} and C_{60}-water lead to the formation of kinetically stable C_{60} aggregates with hydration shells. The presence of a stable hydrophilic shell also weakens the interaction of C_{60} with hydrophobic molecules of non-polar organic solvents. Fullerene can be dispersed in water by transfer from an organic solvent using sonication without the need for stabilizers or chemical modifications [65].

Aqueous solutions of fullerenes are needed for biomedical research. In addition to extraction and direct dispersion in water, micelles of surfactants, as well as covalent modification of fullerenes, can be used for dissolution [68]. Indeed, the addition of several OH groups lead to the formation of so-called fullerenols, for example $C_{60}(OH)_{18}$ and $C_{60}(OH)_{24}$, which are much more soluble in water [69–73]. Solubility also increases in the case of malonic acid derivatives. [74,75]. The existence of $C_{60}(OH)_{18}$ and $C_{60}(OH)_{24}$ in water in the form of aggregates [69] indicates the importance of the hydrophobic effect and intermolecular attraction.

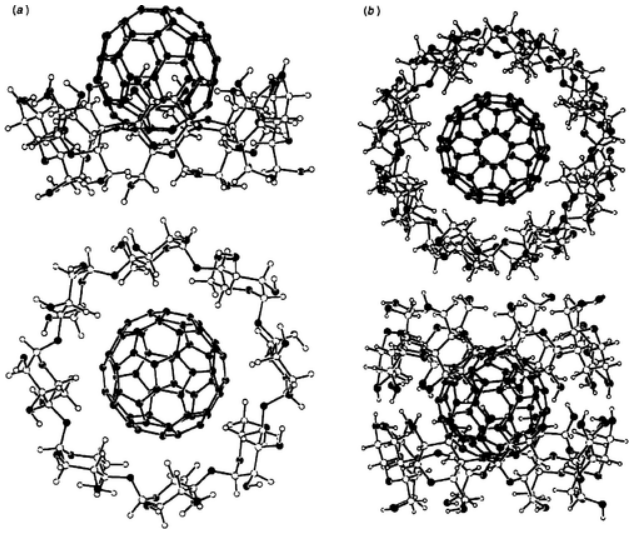

Figure 1. Structures of 1:1 and 2:1 complexes between γ-cyclodextrin and C60 from modeling experiments [76].

Covalent modification can change many properties of fullerenes [77]. Therefore, non-covalent modification methods are also relevant. This approach avoids changes in chemical properties. It was reported in [78] that the dissolution of C_{60} in water can occur as a result of the formation of a complex with γ-cyclodextrin. This gave impetus to the study of host + guest interactions (figure 1) [76,79–90]. The hydrophobic cavity of cyclodextrin is close to the size of the C60 molecule. In addition to the 1:1 complex, a 2:1 cyclodextrin-fullerene association is also possible. The work [90] reports the use of a set of γ-cyclodextrin thioesters with additional hydrophilic groups to transfer C_{60} into water. In addition to hydrophobic interactions, the stability of the complex may also be due to charge transfer from oxygen atoms to C_{60} [79].

Ionic water-soluble calixarenes can also be used to transfer C_{60} molecules into water in the form of host + guest complexes [91,92]. Solubilization of water-insoluble compounds using surfactant-based complexes is a widely used procedure that has been repeatedly applied to fullerene. Micelles [80,81,93–97] and microemulsion droplets [98,99] have often been used to transfer C_{60} into water, both with and without sonication. The use of vesicles of different types of charge also allows the transfer of C_{60} molecules into the aqueous environment [93,94] Non-ionic and cationic colloidal surfactants have also been used to solubilize C_{70}, C_{76} and C_{78} [100]. Single-walled carbon nanotubes were transferred into water using sodium dodecylbenzenesulfonate [101,102] and melamine sulfonate [102].

The position of C_{60} in the micellar pseudophase was discussed based on the study of UV-visible spectra [81,93,94]. On the one hand, a hydrophobic all-carbon molecule must be

located within a micellar hydrocarbon core. On the other hand, charge transfer interactions of highly electron-withdrawing C_{60} can lead to its location near the hydrophilic part of the micelle. At the same time, many authors discovered particles of two different sizes in surfactant solutions. For example, in aqueous solutions of Triton X-100 and its reduced form, both molecular particles and colloidal particles with a diameter of about 10 nm were recorded [80,81]. Particles with sizes of 5.9 – 7.6 and 98 – 180 nm were recorded in solutions of a number of nonionic surfactants [97].

This phenomenon reflects the occurrence of two different processes: (1) dispersion of C60 in water, enhanced by the stabilization of crushed solid particles by adsorbed surfactant molecules, and (2) solubilization of single fullerenes in small surfactant micelles. A gradual transition from dispersion (large particles) to solubilization (much smaller particles) along with increasing surfactant concentration was demonstrated in the work [97]. With the addition of sodium dodecyl sulfate, only large colloidal particles (79 – 122 nm) were obtained. [97]. UV-visible spectra demonstrate the difference between fullerene-surfactant systems obtained in the presence of oxygen or in a nitrogen atmosphere [94].

Another approach to increasing the concentration of fullerene in an aqueous system is to use water-soluble polymers or oligomers [95,97,103–108]. For example, obtaining a suspension of sucrose or dextran in a solution of C_{60} in CCl_4 followed by evaporation of the solvent, mixing in a mortar, adding water and centrifugation made it possible to obtain water-soluble fullerene-carbohydrate complexes with a total concentration of C_{60} up to $1{,}3 \times 10^{-4}$ M [104]. Such procedures can also lead to the production of polymer-stabilized fullerene aggregates dispersed in water. The use of sodium carboxymethylcellulose also makes it possible to obtain a suspension of C_{60} in water, producing particles tens of nanometers in size [103].

Effective solubilizers (or dispersants) of fullerene are polyethylene glyco [105] and polyvinylpyrrolidone (PVP) [97,106–109]. The physicochemical properties of fullerene/PVP complexes and their possible medical applications were considered in the works [110–112].

1.4 Fullerene films on a water surface

Since most applications of fullerenes involve the formation of thin films, studying the surface properties of these systems seems to be an urgent task. One of the possible approaches to obtaining structurally ordered fullerene assemblies is the production of Langmuir films at the air-water interface and their subsequent transfer to solid substrates [113]. However, studies of films of pure fullerenes at the air-water interface have revealed the formation of clusters of various thicknesses on the water surface, resulting from strong hydrophobic fullerene-fullerene interactions. For the first time, the formation of Langmuir films of fullerene C_{60} at the liquid/gas interface was considered in the work [34]. The existence of mono- and multilayer films at the liquid/gas interface has been reported. To form films, 100 μl of a 0.05-0.1 mM solution of C_{60} in benzene was applied to approximately 400 cm^2 of water surface in a Langmuir bath. Fully compressed monolayer C_{60} films were extremely stiff and withstand surface pressures greater than 65 mN/m (figure 2). The molecular radius calculated from compression isotherms turned out to be 5.6 ± 0.7 Å[34]. Films obtained with large deposition volumes had values of the order of 3.5 Å2 and became visible to the naked eye at the edges of the cuvette, appearing as yellow crystals. In accordance with these observations, it was assumed that bi- or multilayers of C_{60} were formed instead of a monolayer at deposition volumes greater than 100 μl. Such multilayers withstood surface pressures greater than 100 mN/m for 8 h without film destruction. The behavior of single-layer and multilayer fullerene films was reproduced in different experiments.

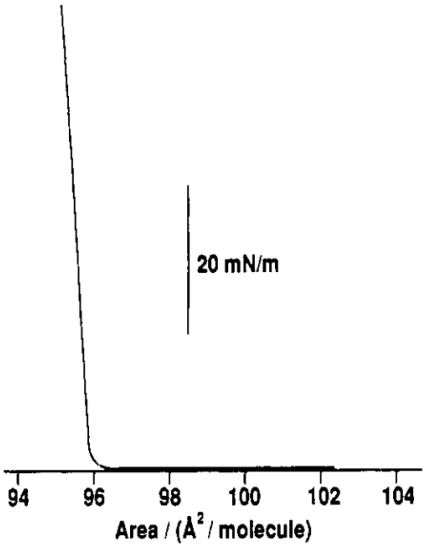

Figure 2. Surface pressure isotherm of a C_{60} fullerene film at 25 °C [34].

The authors of another work observed the formation of only multilayer films [114]. Manipulations such as the use of low initial surface concentrations, increasing the evaporation time of the solvent used for deposition or its volume, or increasing the temperature do not lead to the formation of fullerene monolayers. All isotherms show only low surface pressure (<1 mN/m) with an area per molecule corresponding to the expected formation of a monolayer (figure 3).

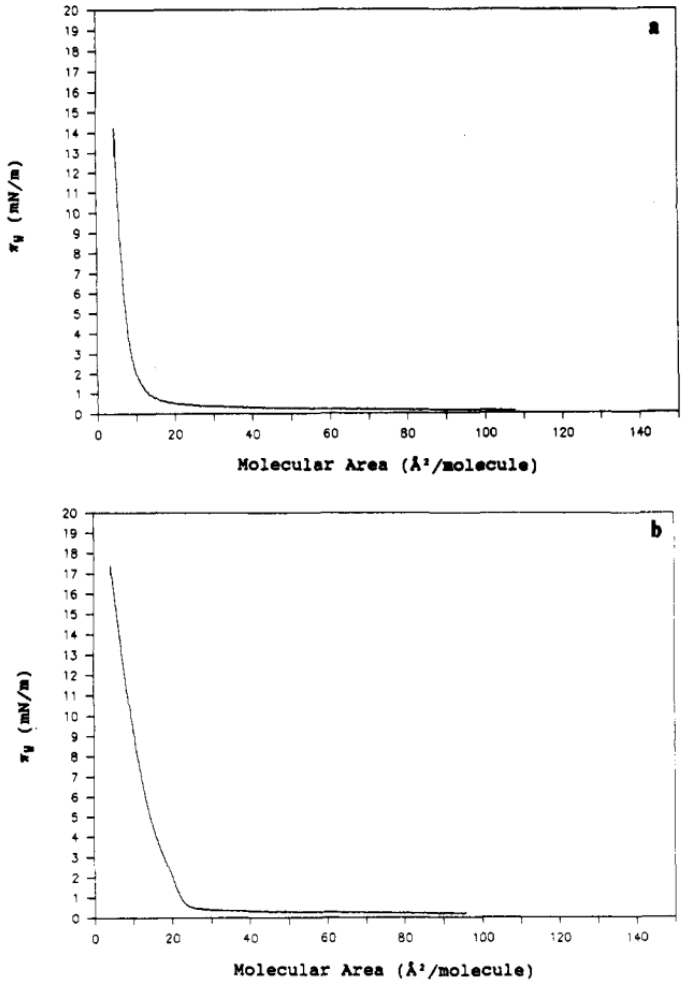

Figure 3. Compression isotherms of films a) C_{60} and b) C_{70} [114].

Significant surface pressure appears only when applying a mass of fullerene equivalent to five or more monolayers (figure 4). The compression isotherm turns out to be linear. For a multilayer film, you can consider several options for its possible structure. First, the molecules can be organized in a system of relatively uniform monolayers. Secondly, they can form ordered domains (islands), each of which consists of several layers. The first situation is unlikely, since the surface pressure at global surface concentrations corresponding to the formation of a fullerene monolayer on the water surface is zero.

The isotherm of pure C_{70}, in contrast to the isotherm of C_{60}, has a distinct break, indicating a two-dimensional phase transition. The nature of the compression isotherm in the region of this kink changes with temperature. The fracture becomes more noticeable as the surface pressure increases and the temperature decreases. The results of deposited fullerene films on a water surface indicate strong adhesion of the film to water [141].

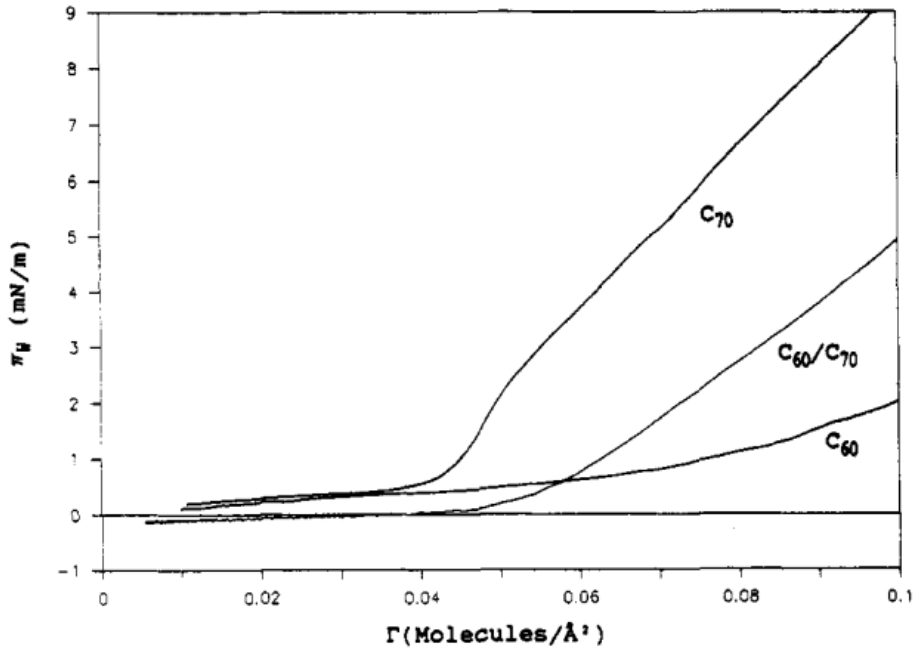

Figure 4. Dependence of surface pressure on average surface density [114].

To overcome the problems associated with the aggregation of fullerene molecules at the liquid/gas interface, two approaches are used. The first is to incorporate fullerenes into the matrix of an amphiphilic compound to obtain mixed Langmuir films. Long chain fatty acids or alcohols were used for this purpose [115]. It should be noted that the expected protection is not always effective, and aggregation of fullerenes remains a problem. Amphiphilic molecules containing a cavity capable of containing a fullerene, such as crown ethers [116] or calixarenes [117], turned out to be the most suitable matrices for the production of fullerene-containing composite Langmuir films.

The second approach is to chemically modify the fullerene molecule, typically by covalently attaching the hydrophilic head group of an amphiphilic compound to produce an addict. In this case, many properties of fullerenes important for their application are retained at a low degree of functionalization. The addition of a hydrophilic head group to the fullerene core leads to a significant improvement in the characteristics of the film on the water surface.

The polar head group is responsible for attraction to the aqueous subphase, thereby preventing three-dimensional aggregation and allowing the formation of monolayers at the air-water interface [118]. However, in most cases, when fullerene nuclei come into contact with each other in compressed Langmuir films, their irreversible aggregation occurs, and the monolayer does not return to its original stretched state. The resulting films also turn out to be rigid, which makes them difficult to transfer to solid substrates. An example is fullerene derivatives bearing dendritic glucose branches [119]. The dendritic part is sufficiently voluminous to prevent contact between adjacent fullerenes when the film is compressed, so the irreversible aggregation usually observed for amphiphilic fullerene derivatives does not occur. Fullerenes can also attach to the branched shell of a diblock structure [120]. In this case, the fullerene units are embedded in the middle of a dendritic structure, which is able to provide a dense insulating layer around the fullerene cores, thereby preventing irreversible three-dimensional aggregation.

1.5 Interaction of fullerene with amphiphilic polymers

Many of the unique properties of fullerenes cannot be used in practice due to its low solubility in water. One way to solve this problem is to form complexes or conjugates of fullerenes with amphiphilic polymers, such as poly-N-isopropylacrylamide (PNIPAM), polyvinylpyrrolidone (PVP) and polyethylene glycol (PEG).

1.5.1 Interaction with poly-N-isopropylacrylamide (PNIPAM)

The C_{60}-PNIPAM conjugate exhibits a rapid and reversible temperature-dependent soluble/insoluble transition over a narrow temperature range in the region of the lowest critical solution temperature (LCST), induced by the phase transition of the PNIPAM chain bound to C60.

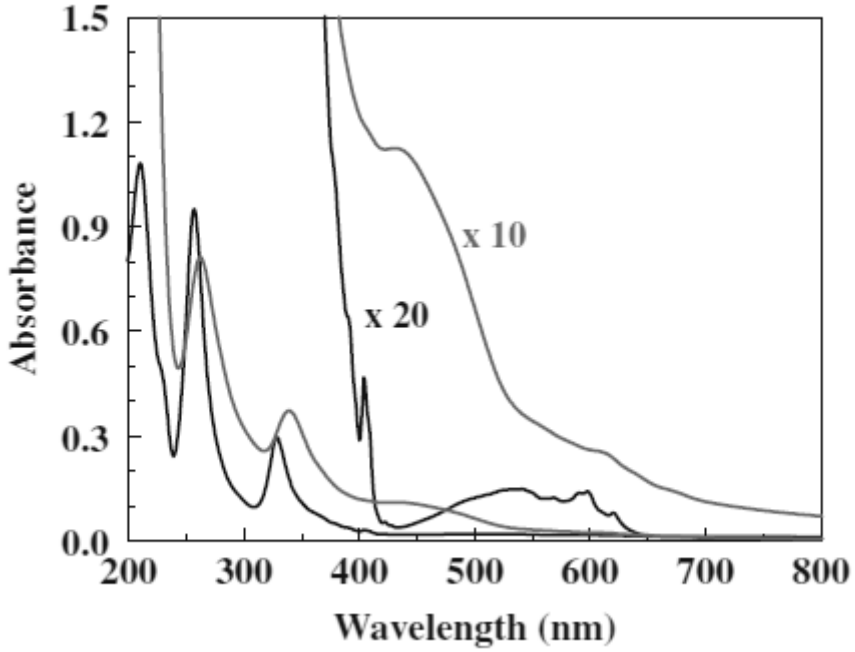

Figure 5. UV-visible absorption spectra of the C_{60}-PNIPAM complex in aqueous media (blue line) and pure C_{60} in hexane (black line) at 20 °C. Insets represent the same spectra at the indicated magnifications. [121].

Turbidity and dynamic light scattering (DLS) measurements showed that below the LCST, C60-PNIPAM forms a micelle-like structure with the C_{60} molecule as the inner core, whereas above the LCST, the micelles aggregate, resulting in a turbid solution. Below its LCST, the polymer hydrates and expands in water. Above the LCST, PNIPAM transforms into a compact form due to dehydration and inter- and intramolecular hydrophobic interactions [122,123]. The LCST of a polymer strongly depends on its chain length and end groups [124,125]. PNIPAM with a longer chain or a more hydrophobic end group has a lower LCST. When comparing the absorption spectra of the C60/PNIPAM complex and pure fullerene in hexane, a characteristic absorption band was discovered around 430 nm (figure 5). Due to the presence of a carbonyl group, PNIPAM interacts with C_{60}, forming a charge transfer complex [121]. Dynamic light scattering measurements showed that the particle size of the C_{60}/PNIPAM complex increased with increasing PNIPAM chain length. Using the DLS method, the dependence of the diameter and ζ-potential of C_{60}–PNIPAM complexes on their molecular weight was obtained [121]. The particle size of the C_{60}–PNIPAM complex increases in proportion to the molecular weight of the polymer fragment, since when longer PNIPAM chains are used, the number of fullerene fragments interacting with the polymer increases. A complex with a large number of polymer

units and, accordingly, a larger particle size has higher stability in an aqueous system. The ζ potential of the C_{60}–PNIPAM complexes shifts from a negative to a more neutral value with increasing polymer chain length. It is assumed that C_{60} acquires charge due to charge transfer from oxygen atoms in water. Thus, the negative zeta potential of the complex is caused by the C_{60} fragments. The stability of the complexes under consideration is achieved due to the steric repulsion of PNIPAM chains adsorbed on fullerene. At the same time, long PNIPAM chains led to an increase in the stability of the complex dispersion. Similar to the behavior of the C_{60}/PNIPAM conjugate dispersion in aqueous solutions, the C_{60} aqueous dispersion with PNIPAM exhibited rapid and reversible changes in the degree of aggregation in response to changes in temperature in the LCST region [121].

The effect of reversible temperature changes on the absorption curve profile was also studied. [121]. The solution was heated and then cooled. It became cloudy when heated and then became clear when cooled. At the same time, on the optical transmission curve (figure *6*) Hysteresis occurred, and for the conjugate with 4 polymer units it was greater than for the conjugate with 20.

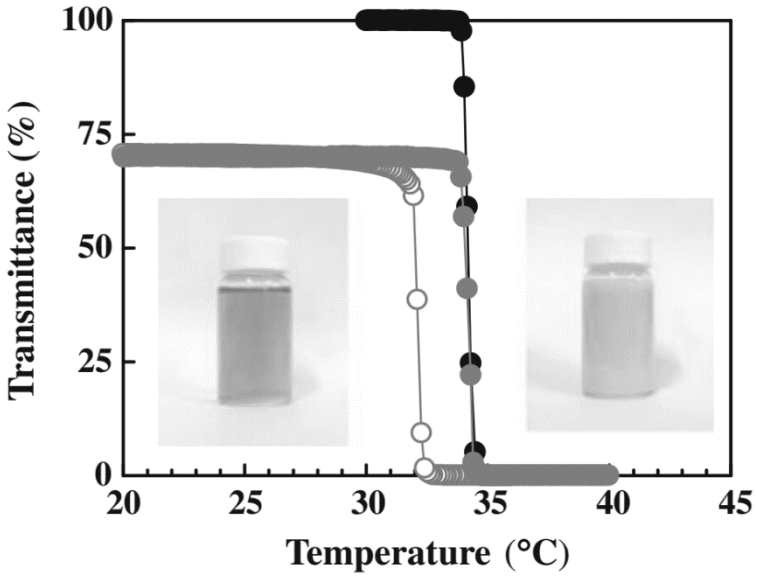

Figure 6. Temperature dependence of optical transmittance at 600 nm of the C_{60}/PNIPAM complex in aqueous media at a heating (orange line, including dark circle)/cooling (orange line, including open circle) rate of 0.5 °C/min in the temperature range from 20 °C to 40 °C. As a control, the change in the transmittance of PNIPAM itself upon heating is shown (black line). The insets show aqueous solutions of the C_{60}/PNIPAM complex (left at 20 °C, right at 40 °C) [121].

C60/PNIPAM conjugates in water were studied using gel permeation chromatography (GPC) [126]. FI-4 и FI-20 – designations of C_{60} conjugates with PNIPAM oligomers containing 4 and 20 monomers, respectively. The chromatogram for FI-4 has two peaks (figure *7*). The second peak belongs to the so-called unimer – a C_{60}–PNIPAM conjugate with an oligomer containing 4 monomers, and the first peak indicates the existence of aggregates with a higher molecular weight. It is assumed that FI-4 can form core–shell structures with a fullerene core and a PNIPAM shell. This structure exists below the NCTR.

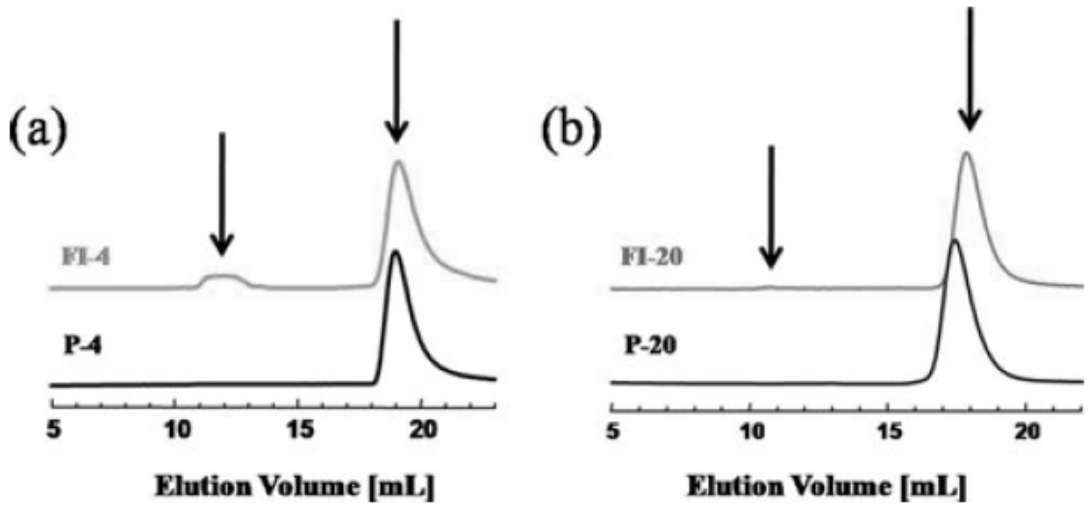

Figure 7. GPC curves for (a) FI-4 and (b) FI-20. These measurements were carried out at a concentration of 5.0 mg/ml at 25 °C [126].

At a temperature of 25 C°, unimers and micelle-like aggregates of the core-shell type coexist in water. Unlike FI-4, the chromatogram for FI-20 contains only one peak (figure *7*). This means that as the chain length increases, the tendency to form core-shell aggregates decreases. This is due to the fact that as the length of the polymer chain increases, the interactions between fullerene molecules weaken. At the same time, there is an increasing tendency for the polymer to wrap fullerene molecules through the formation of a charge transfer complex through the carbonyl group of PNIPAM to the surface of the fullerene molecule. The effect of polymer chain length on the temperature phase transition was investigated by analyzing the dependence of optical transmittance on temperature for different concentrations of conjugates.

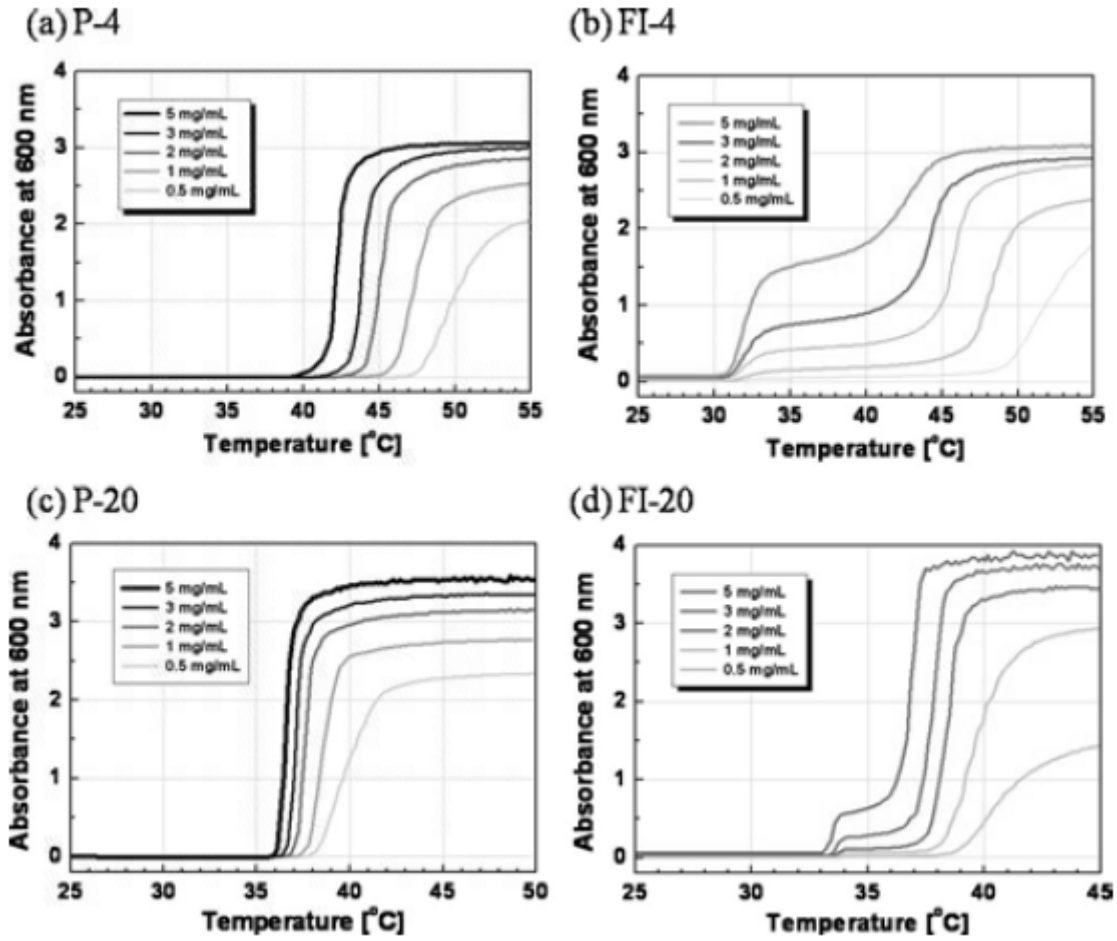

Figure 8. Dependence of optical transmittance on temperature for FI-4 (b) and FI-20 (d)[126].

This dependence shows two phase transitions (figure 8). The temperature of the first transition is almost independent of concentration. At the same time, the temperature of the second transition strongly depends on the concentration of the conjugate. This suggests that the first and second phase transitions are associated with the coexistence of unimers and micelles, respectively. The changes in the absorption band in the optical transmittance dependences for the first transition are greater for FI–4 than for FI–20. With the second transition, the situation is the opposite - the absorption value for FI –20 is greater than for FI –4. This means that the LCST of PNIPAM, synthesized by radical polymerization with atom transfer, shifts towards lower temperatures with an increase in the number of units of the polymer chain.

1.5.2 Interaction with polyvinylpyrrolidone (PVP)

In dilute solutions of a mixture of polyvinylpyrrolidone (PVP) and C_{60} fullerene, strong intermolecular interactions arise [127]. Studies of dilute aqueous solutions of polyvinylpyrrolidone/C_{60}PVP fullerene complexes using static (SLS) and dynamic light scattering methods have shown the presence of strong intermolecular interactions, effective at distances of about 45–50 nm. In these solutions, two concentration ranges are clearly distinguished. Above a critical concentration, fluctuations in solutions are difficult and in DLS experiments only one, diffusion, regime is observed. Upon dilution, this single structure breaks up into large fragments and a slow mode gradually appears, associated with long-range concentration fluctuations. The angular and concentration dependences of the slow mode diffusion coefficient indicate the presence of strong intermolecular interactions.

C_{60}PVP is a charge transfer complex. The fullerene is an acceptor, and the polymer is an electron donor. Transfer occurs through the N–C=O fragment of PVP to the surface of the C_{60} core [128]. Analysis of DLS data shows that the size of pure fullerene aggregates in water is larger than PVP molecules (K-25, 28 kDa). This promotes efficient adsorption of the polymer on C_{60} aggregates. A solution of pure PVP in water has a ζ potential of 7.1 mV. A solution of pure fullerene in water without adding polymer – (– 15 MV). When a polymer is added to a fullerene solution, a noticeable change in this value is observed - (- 18.8 MV), which is explained by the transfer of electrons from the N–C=O fragment of the polymer to the fullerene surface during the formation of the complex. Scanning the ζ-potential signal for the fullerene complex with PVP leads to three different values: – 3.68 mV, – 18.44 mV, – 29.62 mV (figure 9). The first value corresponds to PVP bound to encapsulated C_{60}. The second refers to PVP dissolved in water, the third refers to a polymer layer (<8 nm) formed around the fullerene core in solution.

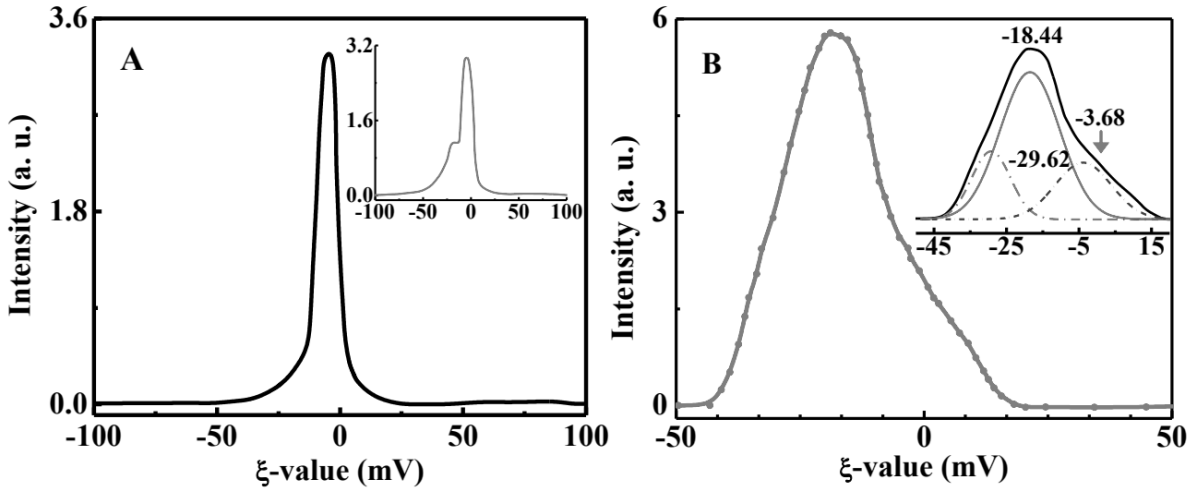

Figure 9. Distribution of ζ-bands in a 40.0 g/L PVP nanofluid (A) before and (B) after addition of 4.0 μM C_{60} in water, with the distribution in a pure sample of 4.0 μM C_{60} in water in inset A. Inset B describes sweeping the signal into three components [128].

Using transmission electron microscopy, it was discovered that C_{60} clusters have a shape close to spheroids with sizes ranging from 200 to 250 nm [128]. When PVP is added, the spheroidal structure is retained, and the cluster sizes increase slightly to 200-300 nm. Fullerene clusters with PVP have a core-shell structure with a polymer shell thickness of 30-50 nm and a fullerene core with a diameter of 200-250 nm.

The mechanism of dissolution of C_{60}–PVP complexes in water can be represented as follows. In PVP dispersed in a weakly polar solvent (n-butanol) (figure 10a), electron transfer occurs N → O through the O=C–N group in the lactam ring, since oxygen is more electronegative than nitrogen. This is the process of keto-enol tautomerism (figure 10b) with the formation of a reactive form of PVP (figure 10c). As a result, when added to electron-deficient C_{60}, the electron-rich PVP molecule is easily adsorbed on the surface of C_{60}, forming a polymeric surface layer. This is shown schematically in the diagram (figure 11), where is the reactive lactam ring (figure 11a) when combined with a C_{60} particle (figure 11b) forms a C_{60}-PVP complex (figure 11c). In this model, PVP is adsorbed on the molecular surface of a C_{60} aggregate and then forms an interconnected network with it. An electron-rich surface, i.e. a surface with a negative charge, ultimately results from the retention of C=O n electrons on the C_{60} surface. In the future, the hybrid structure (figure 11d) acquires a surface-modified C60 molecule with a stable adhesive PVP surface layer upon complete removal of the solvent and drying at low pressure. Drying facilitates solvent removal by electron transfer in the

pyrrolidone ring (figure 11c). Adsorbed hydrophilic PVP surface layer on C_{60} surface (figure 11d) promotes the solubilization process in water through the N atom of the pyrrolidone group with the formation of an aqueous C_{60}–PVP nanofluid (figure 11e). When the dried mass is dissolved in water, which also acts here as a nucleophile, electron transfer N → O occurs in it along the O=C–N< fragments in the pyrrolidone ring. As a result, the electrons of the surrounding water molecules (O_2 n-electrons) are added to the O=C–N< fragment of the pyrrolidone compound and thereby promotes the dissolution of C_{60} in water in the form of a stable nanofluid.

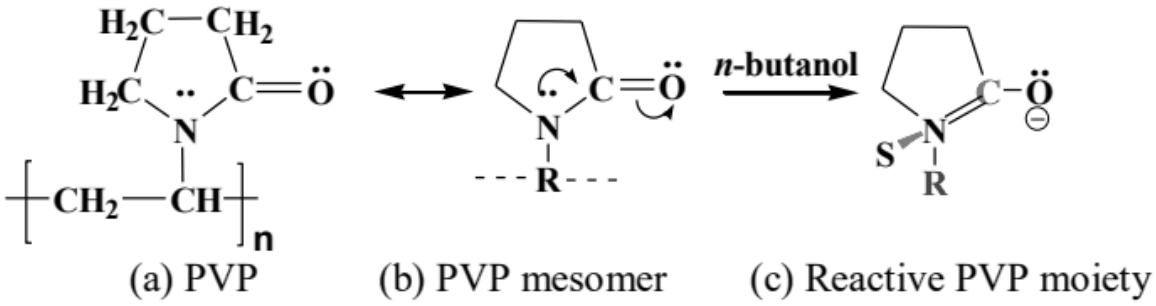

Figure 10. Creation of a reactive site in (a) PVP in n-butanol by mesomerism in the (b) lactam ring so that it serves as (c) an efficient electron donor. R is part of the PVP carbon chain and S is n-butanol, which is weakly bonded to nitrogen atoms [128].

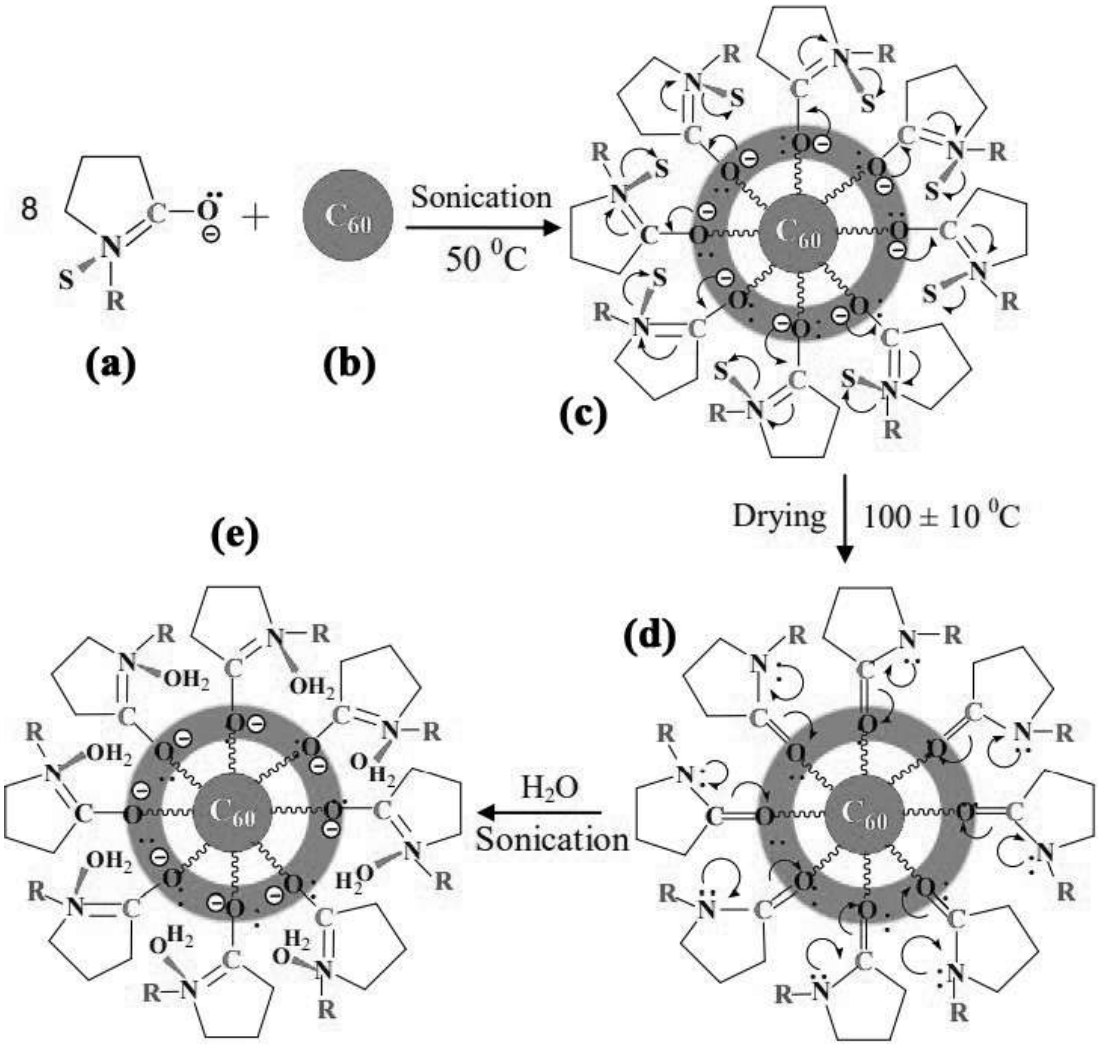

Figure 11. Model of adsorption of (a) electron donor PVP on (b) a nascent C_{60} surface during the formation of (c) an encapsulated C_{60} molecule in n-butanol. The dried mass (d) forms (e) aqueous C_{60} nanofluid when redispersed in water. The actual number of PVP molecules adsorbed on the surface of C_{60} may be greater than that shown in the figure. [128].

Insight into the cluster conformation of C_{70}-PVP complexes in aqueous solution was obtained using a combination of dynamic and static light scattering methods [129]. The clusters have relatively large sizes (on average ~100 nm) and a loose network structure, where fullerenes serve as junction points for two or more PVP molecules. C_{70}-PVP clusters are stable and do not disintegrate when diluted.

In this system, two diffusion processes take place. Slow diffusion is associated with the movement of large C_{70}-PVP clusters, whereas fast diffusion is associated with the presence of single polymer molecules or small C_{70}-PVP complexes containing a single PVP chain. The molar mass and size of C_{70}-PVP clusters increase with increasing fullerene content. However, at a constant fullerene content, an increase in the molar mass of the matrix PVP does not affect

the mass and size of the clusters. Dilution of C_{70}-PVP solutions also has no effect. In C_{70}-PVP there is a certain molar ratio between the C70 molecules and the polymer units. This ratio (≈ 200) does not depend either on the molar mass of the PVP matrix or on the fullerene content. This ratio probably cannot be exceeded, otherwise free fullerene molecules not associated with PVP will appear. PVP chains are saturated with fullerene, and fullerene molecules cease to dissolve in water. At lower fullerene concentrations, free PVP molecules can exist in solutions. The size and molar mass of clusters increase with increasing fullerene content in the complex. However, if the fullerene content is kept constant, none of the cluster parameters is affected by an increase in the molar mass of the matrix PVP.

1.6 Fullerene derivatives

To date, many different fullerene derivatives have been synthesized, for example, fullerenols containing hydroxyl groups [40], as well as molecules containing carboxyl groups (carboxyfullerenes), fragments of crown ethers, hydrophilic porphyrins, calixarenes, oligopeptides, polyethylene glycols, and amphiphilic polymer chains (conjugates of fullerenes and amphiphilic polymers) [33].

1.6.1 Polyhydroxylated fullerenes

Polyhydroxylated fullerenes, or fullerenols, occupy a special place in a relatively small group of water-soluble fullerene derivatives. Fullerenols have a relatively simple structure, and their solubility can be changed from almost zero to about 60 g/L at room temperature by increasing the number of hydroxyl groups [130]. They are characterized by high adhesion to metals and semiconductors, form thin films on their surface, due to which they can be used in micro- and optoelectronics [131]. On the other hand, fullerenols improve the mechanical properties of materials and are used as modifiers for concrete and paints [40]. The most important are probably the medical applications of fullerenols. Their antioxidant properties have been known for more than 20 years. [132,133]. In addition, their radioprotective effect was discovered [134].

Fullerenols have a fairly simple structure (figure 12), are characterized by low toxicity and wide possibilities for subsequent modification, which makes them convenient for practical use.

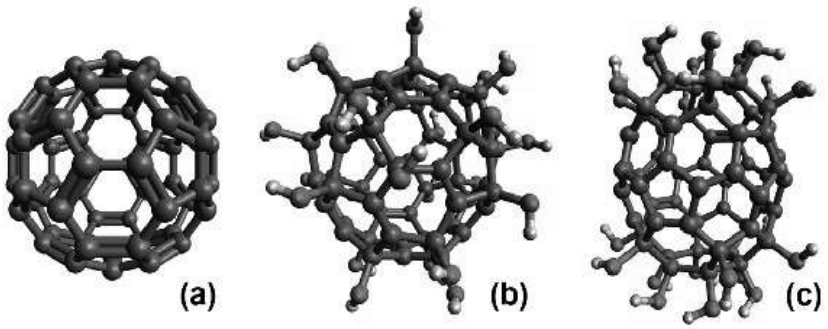

Figure 12. Structures of a) C_{60} fullerene; b) fullerenol $C_{60}(OH)_{24}$ with uniformly distributed hydroxyl groups; c) fullerenol $C_{60}(OH)_{24}$ with hydroxyl groups distributed at the poles [135].

The term “fullerenol” includes various types of compounds. Firstly, fullerenols can be called derivatives of all fullerenes (C_{70}, C_{76}, C_{78}, C_{84}, C_{90} and others), and not just the most common fullerene C_{60}. Secondly, fullerenols can contain not only hydroxyl groups, but also carbonyl groups (=O) Cn(OH)xOy or salt groups, for example, Cn([OH)xOy](ONa)z [40].

Despite intensive studies of fullerenols for more than two decades, the information obtained on the properties of fullerenols and their aqueous solutions, primarily surface properties, appears to be insufficient. Until now, information about the dependence of these properties on the number of hydroxyl groups in the molecule is very limited. The main information in the literature relates primarily to fullerenol $C_{60}(OH)_{24}$.

One of the main properties of fullerenols is their solubility in water, and, therefore, the question arises about the influence of the number of hydroxyl groups on it. In [130] , fullerenol molecules with the number of OH groups of 8, 16, 24, 36, and 44 were studied using numerical methods. In an aqueous solution, water and fullerenol molecules are connected by hydrogen bonds of two types: (1) the oxygen atom of fullerenol interacts with the hydrogen atom of water and (2) the hydrogen atom of fullerenol interacts with the oxygen atom of water. The formation of hydrogen bonds can be considered the most important interactions in aqueous solutions of fullerenols. The length of both types of hydrogen bond is about 0.19 nm. This corresponds to a strong interaction between molecules, i.e. fullerenol molecules are highly hydrated in aqueous solution.

Based on the radial distribution functions of water molecules in the hydration shell of fullerenes with different numbers of OH groups, an assessment was made of the approach of water molecules to fullerenol. The smallest distances at which the radial distribution function is different from zero were observed for derivatives with 8 and 44 hydroxyl groups. In fullerenols $C_{60}(OH)_8$ and $C_{60}(OH)_{44}$ OH groups are located quite close to each other. It is assumed that a larger OH-OH distance in a fullerenol molecule leads to increased hydration.

Based on the calculated dependences of the Gibbs free energy, enthalpy and entropy factors on the number of hydroxyl groups, it was found that hydration is most effective in the case of $C_{60}(OH)_8$, when the Gibbs energy per hydrogen bond is 28 kJ/mol-1. As the number of OH groups increases, this energy gradually decreases, reaching 12 kJ/mol-1 in the case of $C_{60}(OH)_{44}$. Thus, the contribution of each OH group to the energy of the system decreases as their number increases. It is obvious that the solubility of fullerenols increases with increasing number of hydroxyl groups.

The solubility of fullerenols has been studied not only through computer modeling. Semenov and co-authors experimentally determined the dependence of the solubility and density of aqueous solutions of fullerenol $C_{60}(OH)_{24}$ on temperature [131]. It was shown that the density of a saturated fullerenol solution increases monotonically with increasing temperature. This dependence has a characteristic s-shaped form (figure 13).

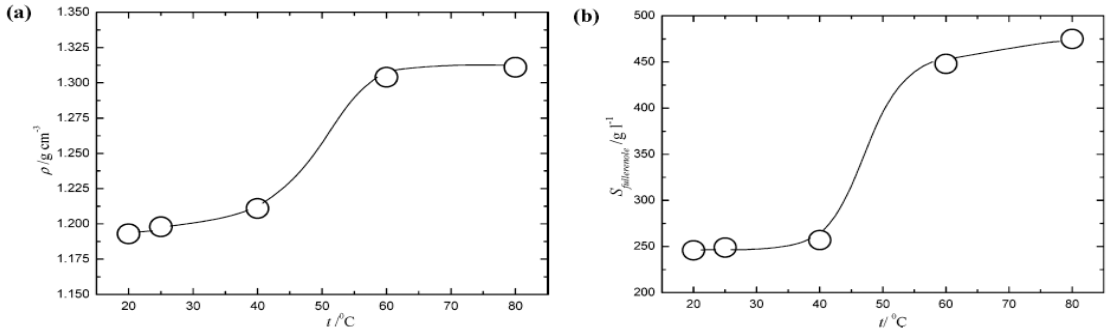

Figure 13. Temperature dependences of solution density (a) and fullerenol solubility in water (b) in the temperature range from 20 to 60°C [131].

The resulting dependence of the solution density on temperature can be explained by a decrease in the density of water and the density of fullerenol, an increase in the solubility of denser fullerenol in less dense water, as well as a weakening of van der Waals forces. The dependence of solubility on temperature also has an s-shape and is characterized by a monotonic increase in the solubility of fullerenol with increasing temperature. Thus, the

solubility of fullerenols turns out to be very high. At similar values of mass concentration and mass fraction, the solubility of fullerenol corresponds to the solubility values for salts such as sodium chloride. Moreover, the solubility of fullerenol in water increases significantly with increasing temperature above 50 °C and exceeds the solubility of sodium chloride at the same concentrations.

The size of fullerenol associates in an aqueous solution increases rapidly with increasing concentration, which was confirmed by DLS. No unassociated particles were found in the solution. This suggests that associates arise even in highly dilute solutions. From the results of a study of the electrochemical properties of fullerenol solutions, it follows that the generally accepted suffix “ol” inherent in alcohols is not entirely correct. In particular, from the dependence of the pH of solutions of fullerenol $C_{60}(OH)_{24}$ on molar concentration (figure 14), the following dissociation mechanism follows [136]:

$$C_{60}(OH)_{24} \rightarrow [C_{60}(OH)_{21-23}]^{+} + OH^{-}$$

In addition, even dilute solutions turn out to be highly alkaline. As the molar concentration increases, the rate of pH growth decreases. $C_{60}(OH)_{24}$ behaves as a medium-strength electrolyte at moderate concentrations (0.001 M - 0.07 M) and as a moderate-strength electrolyte at lower concentrations.

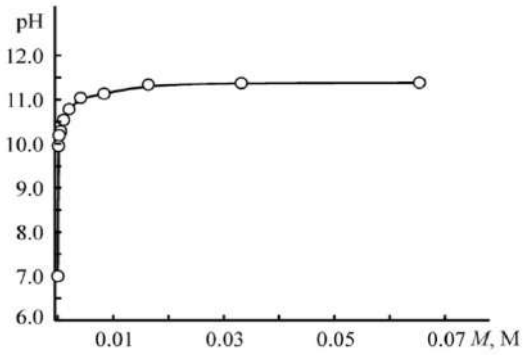

Figure 14. Dependence of the pH of solutions of fullerenols $C_{60}(OH)_{24}$ on their molar concentration [136].

1.6.2 Carboxylated fullerenes

Among various derivatives, carboxyfullerenes have also attracted considerable attention due to their extensive medical applications. For example, it has been shown that the ability to interact with enzymes allows C_3-tris-malonyl-C_{60}-fullerene and D_3-tris-malonyl-C_{60}-fullerene

to inhibit the formation of citrulline and NO, thereby affecting the relaxation of vascular smooth muscle [137]. These derivatives may also inhibit acrylamide toxicity in human neuroblastoma cells. According to [138], he cytotoxicity of acrylamide, including apoptosis, is closely related to the level of reduced glutathione (GSH) in cells of a triple cloned subline of the neuroblastoma cell line (SH-SY5Y). The authors suggested that carboxyfullerene suppresses toxicity by maintaining GSH content. In addition, this work highlights the advantage of carboxyfullerene over fullerenol in the inhibition process. Carboxyfullerene is also an effective radioprotective agent. The work [139] reported the protective effects of carboxyfullerene in irradiated mouse cells. The authors found that carboxyfullerene attenuates the radiation-mediated reduction of endogenous antioxidants such as superoxide dismutase and GSH and reduces malondialdehyde levels. The data obtained indicate the promise of carboxyfullerene as a radioprotector with high efficiency and low toxicity. Other studies describe the use of carboxyfullerene derivatives as antioxidants [140–142], cytoprotectors [143] and antimicrobial agents [108], membrane modifiers [144], inhibitors of streptococcal infection [145] and cerebral ischemia [146]. It has also been shown that topical application of carboxyfullerene is capable of inhibiting oxidative damage in biological organisms [147]. Along with this, carboxyfullerenes protect human keratinocytes from apoptosis induced by ultraviolet B [148].

Experimental and theoretical data on the physicochemical properties of carboxylated fullerenes and phase equilibria in systems containing these fullerene derivatives are very limited. Currently, there is a small number of works devoted to the physicochemical study of aqueous solutions of carboxyfullerenes, which contain information on such parameters as refractive indices, electrical conductivity, average and partial molar volumes of solution components, size distribution in aqueous solutions, as well as phase equilibria in binary and ternary systems containing carboxyfullerenes [149–155].

In [149,152] the average molar volumes of carboxylated fullerenes ($C_{70}[(C(COOH)_2]_3$ and $C_{60}[(C(COOH)_2]_3$)) and the partial molar volumes of the solution components (carboxylated fullerene and water) were calculated. Concentration dependencies partial molar volumes of solution components in the region of dilute solutions of carboxylated C_{70} have a rather complex character: in the concentration range of 0.002–0.003, the dependence of the partial molar volume of carboxyfullerene approaches the molar volume of the solid substance

$C_{70}[(C(COOH)_2]_3$, and in the range of mole fractions 10 -5–10−4 values of this quantity become negative (figure 15).

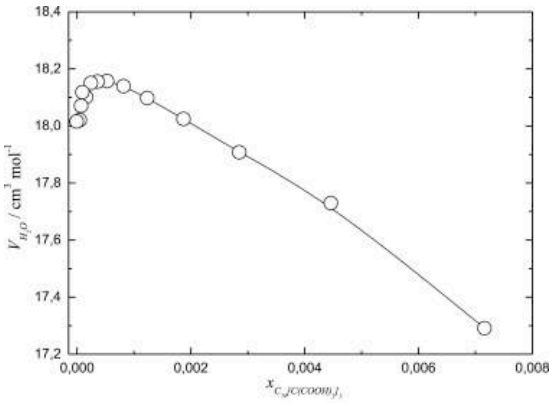

3.1

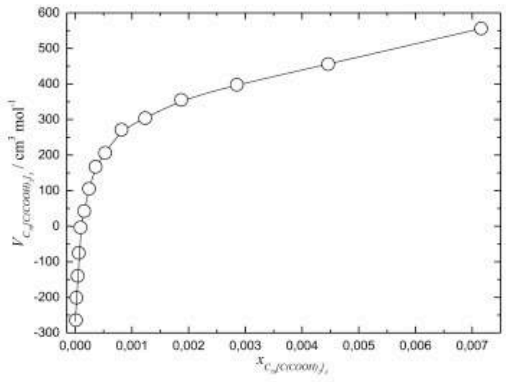

3.2

Figure 15. Molar dependences of partial volumes of solution components – H_2O (Fig. 3.1) and $C_{70}[(C(COOH)_2]_3$ (Fig. 3.2)[149].

Thus, the addition of the first portions of C_{70}-carboxyfullerene extremely compacts and structures the solution. The temperature dependences of the solubility of carboxylated fullerenes in water, presented in (figure 16), show the following: 1) the solubility of carboxylated fullerenes is extremely high (hundreds of g•dm^{-3}); 2) the dependence of solubility on temperature is non-monotonic; 3) solubility diagrams consist of two branches: low-temperature branches correspond to the crystallization of $C_{60}[(C(COOH)_2]3$ $3H_2O$ (in the case of a binary $C_{60}[(C(COOH)_2]_3$ - H_2O) system) and $C_{70}[(C($ $COOH)_2]_3$ $6H_2O$ (in the case of the binary system $C_{70}[(C(COOH)_2]_3$ - H2O); high-temperature branches correspond to the crystallization of unhydrated carboxylated fullerenes. The solubility diagrams have one non-variant point, corresponding to simultaneous saturation with both solid phases [149].

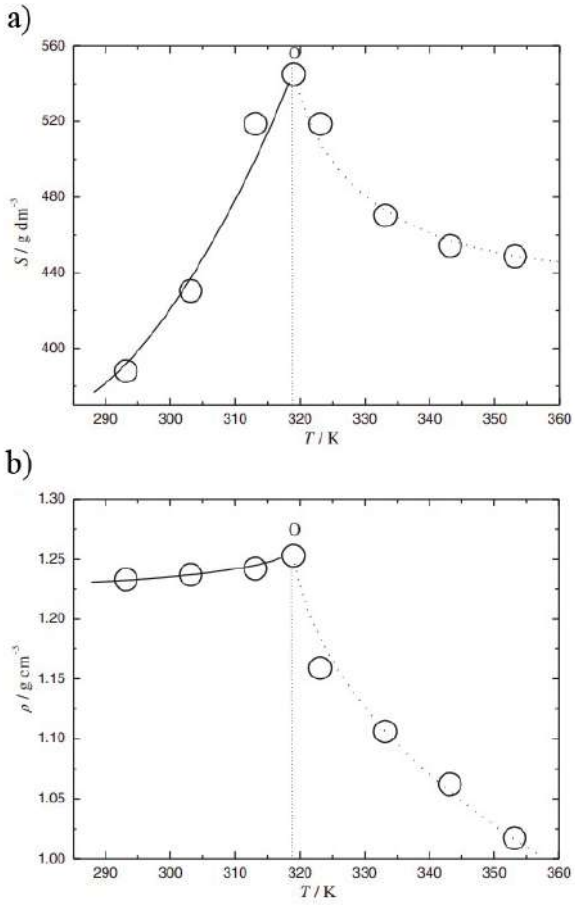

Figure 16. Temperature dependence of a) solubility (S) and b) density (ρ) of aqueous solutions of C_{70}-carboxyfullerene. The solid line corresponds to the crystallization of $C_{70}[C(COOH)_2]_3$ $6H_2O$, the dotted line corresponds to the crystallization of $C_{70}[C(COOH)_2]_3$. O—invariant point corresponding to simultaneous saturation with both solid phases [149].

From the experimental and calculated data, the following conclusions were made about the sizes of carboxyfullerene associates in aqueous solutions: 1) in all studied solutions of carboxylated fullerenes, no monomer molecules were found, even in a dilute solution; (2) a sequential hierarchical association model can be used to describe the association process. The authors of [149] believe that spherical monomer molecules successively form four types of spherical associates. First, aggregates of the first type are formed, then they form associates of the second type, etc. Associates of the fourth type correspond to the colloidal system. To confirm the microheterogeneity of solutions with a high concentration of malonic derivatives (>10 g dm^{-3}), the authors prepared films by crystallization of $C_{60}[(C(COOH)_2]_3$ from aqueous solutions during isothermal evaporation of water from the solution (a drop of the solution was applied to the surface of silicate glass) The microphotograph (figure 17) shows spherical formations (foci of crystallization) with linear dimensions corresponding to associates of the third type [151].

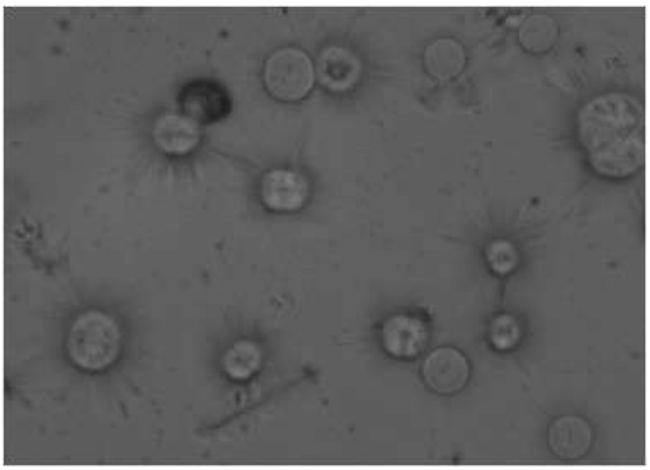

Figure 17. Micrograph of trismalonate derivative crystals in an optical polarizing microscope (thousandfold magnification). The concentration of the initial solution was C = 10 g• dm^{-3} [151].

The authors of [149] also studied a binary system containing water-soluble carboxylated fullerene $C_{70}[C(COOH)_2]_3$. Based on a comparison of these data with information obtained by the dynamic light scattering method, three states of $C_{70}[C(COOH)_2]_3$ associates in solution were identified: (1) in the first case, aqueous solutions of $C_{70}[C(COOH)_2]_3$ consist of clusters with linear dimensions of tens of nanometers and a small amount of hydrated monomer molecules, these solutions are stable; (2) aqueous solutions of $C_{70}[C(COOH)_2]_3$ additionally consist of second-order clusters with linear dimensions of hundreds of nanometers. These solutions begin to lose diffusion stability; (3) the solution consists of second- and third-order clusters with linear dimensions of the order of several micrometers. In this case, first-order clusters disappear from solutions. In this case, the solutions lose diffusion stability. From the data obtained, it was concluded that almost only associates of the first type of carboxylated fullerene participate in diffusion processes. Other types of associates are not labile enough for effective mass transfer (the second and third types of associates). The decrease in diffusion coefficients with increasing concentration of $C_{60}[C(COOH)_2]_3$ can be explained by the fact that the relative mass fraction of associates of the first type decreases with increasing concentration and at the same time the concentration of more massive particles increases.

The authors of [152] obtained experimental data on the viscosity of aqueous solutions of $C_{60}[C(COOH)_2]_3$ (figure 18). It can be seen that the dynamic viscosity decreases with increasing concentration in dilute solutions and becomes almost constant in more concentrated solutions ($w > 0.1$) at both temperatures (298.15 and 323.15 K).

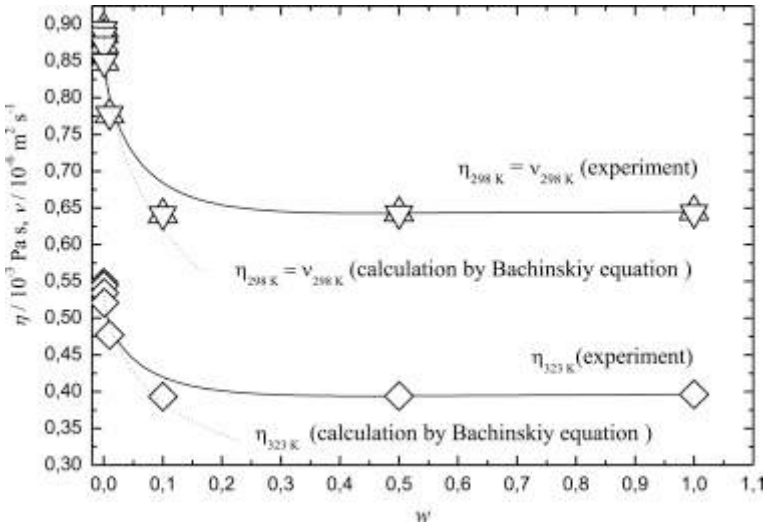

Figure 18. Dynamic (η) (upper curve) and kinematic (ν) (lower curve) viscosity of aqueous solutions of trismalonate C_{60} at 298.15 and 323.15 K. w - mass fraction of $C_{60}[C(COOH)_2]_3$ in aqueous solution [152].

The result was a fairly good agreement between the experimental and calculated data in relatively dilute aqueous solutions of carboxylated fullerene. In the concentration range from 0 to 0.1% wt. there is a rapid decrease in η with increasing concentration. Such a decrease in the function η(w) even in dilute solutions is atypical for solutions with high molecular weight. In more concentrated solutions (from 0.1 to 1.0% wt.), the discrepancy between experiment and calculation increases. These facts can be explained as follows: (1) the destruction of hydrogen bonds between solvent molecules can reduce η (in dilute solutions this effect is stronger); 2) an increase in the concentration of the main structures involved in mass transfer (in the direction perpendicular to the velocity vector of the liquid layers) can increase η (in more concentrated solutions this effect is enhanced). In the concentration range $1.0 \geq w \geq 0.1\%$ wt. these two factors are of approximately equal importance, and the function η(w) passes through a “soft” minimum.

1.7 Surface properties of fullerene derivatives solutions

Aliphatic amino acids can be used to modify fullerene. Thus, in [156] , the surface properties of fullerene derivatives modified with acid residues of arginine and L-lysine were studied. The results obtained showed that C60-arginine has greater surface activity and faster adsorption kinetics than C60-lysine. These differences can be explained by the large number of amino acid residues attached to the fullerene molecule in the first case. An important feature of

the properties of the adsorption layers of C60-arginine and C60-lysine conjugates is the significantly greater dynamic elasticity in the first case. Surface elasticity of 200 mN/m and higher is characteristic of compact packing of strongly interacting nanoparticles at the interface. Approximately halving the C60-arginine adsorption layer with an elasticity of 220 mN/m resulted in a decrease in this value to 140 mN/m. At the same time, the surface tension also decreased to 60 mN/m. Even a small subsequent expansion of the surface by about 10% led to an increase in surface tension to the initial value (before compression).

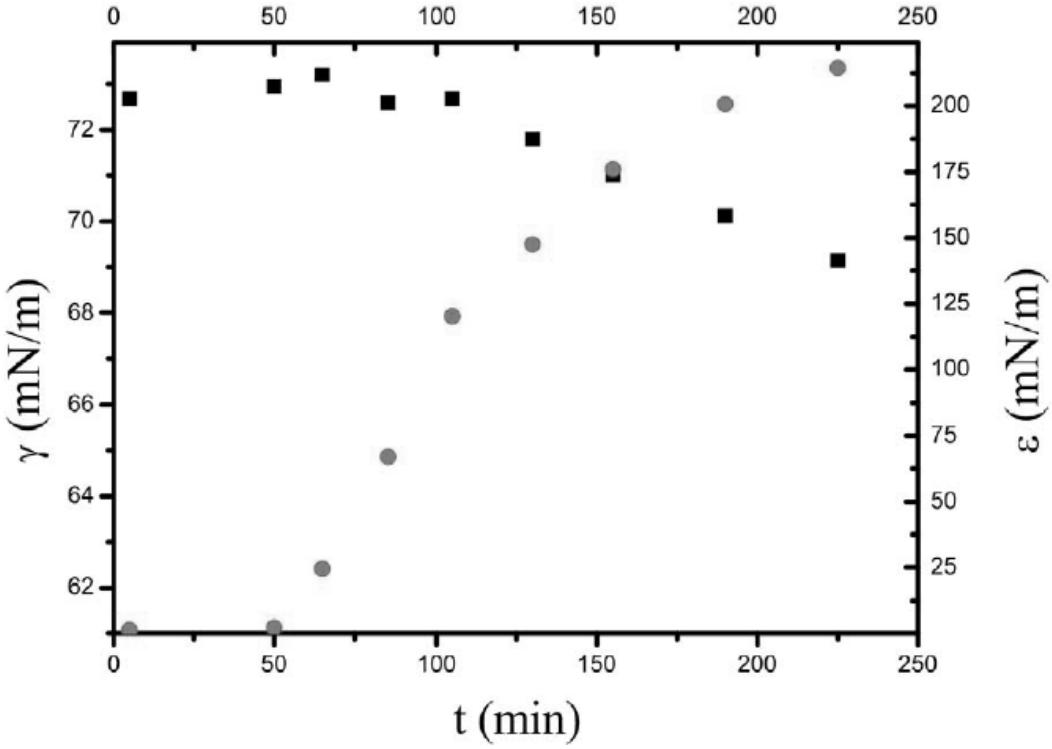

Figure 19. Dependences of surface tension and dynamic surface elasticity on the surface lifetime for a C_{60}-arginine solution with a concentration of 0.5 g/l [156].

Direct measurements of quasi-static surface elasticity during slow compression of the surface of the studied C_{60}-arginine solutions at equilibrium lead to significantly lower values (~ 10 mN/m) than the dynamic surface elasticity for the same adsorption layers measured by the oscillating barrier method. The observed differences can be explained by the formation of an elastic dynamic network of molecules of fullerene derivatives or their aggregates with a relaxation time of mechanical stresses significantly exceeding 10 seconds, even in the case when the surface pressure is close to zero.

Observation of the adsorption layer of the C_{60}-arginine conjugate using a Brewster angle microscope confirms its higher rigidity compared to the layers of the C_{60}-lysine conjugate. A

60% compression of the equilibrium layer on the surface of a 0.1 g/L C_{60}-arginine conjugate solution results in the appearance of a large number of bright spots on the surface (figure 20a). These spots apparently represent areas of multilayers formed when the layer collapses under compression. The sudden expansion of the surface destroys the continuous adsorption layer, leading to the formation of macroscopic cracks (figure 20b). Small aggregates move freely in these cracks, indicating that they are not covered by a continuous film. Similar cracks can be observed after destruction of the adsorption layer of the C_{60}-arginine conjugate with a thin stick (figure 20c).

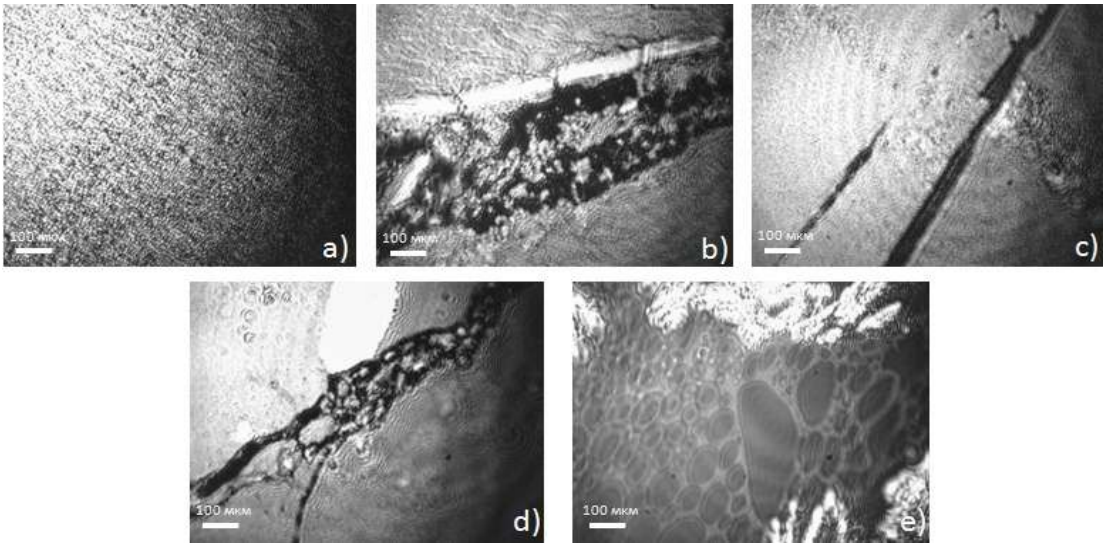

Figure 20. Images of the adsorption film of the C_{60}-arginine conjugate obtained using a microscope at Brewster angle for a solution with a concentration of 0.1 g/L [156].

The amphiphilic nature of fullerenols with a relatively small number of hydroxyl groups leads to their surface activity. In particular, fullerenols with a low number of hydroxyl groups can form insoluble monolayers on the water surface. Films of fullerenol $C_{60}(OH)_{12}$ on a water surface were studied by a group of authors [157]. The results of the neutron reflection experiment confirmed the monolayer nature of the films. Also, using atomic force microscopy, the morphology of Langmuir-Blodgett films was determined. The film thickness turned out to be 12 ± 2 Å (figure 21b), which agrees well with the diameter of the fullerenol molecule (13 Å). In this case, the area per molecule in a monolayer is 190 $Å^2$/molecule. The results of the use of atomic force microscopy confirm that the film turns out to be a fairly homogeneous monolayer and is characterized by only small random fluctuations in thickness (figure 21a).

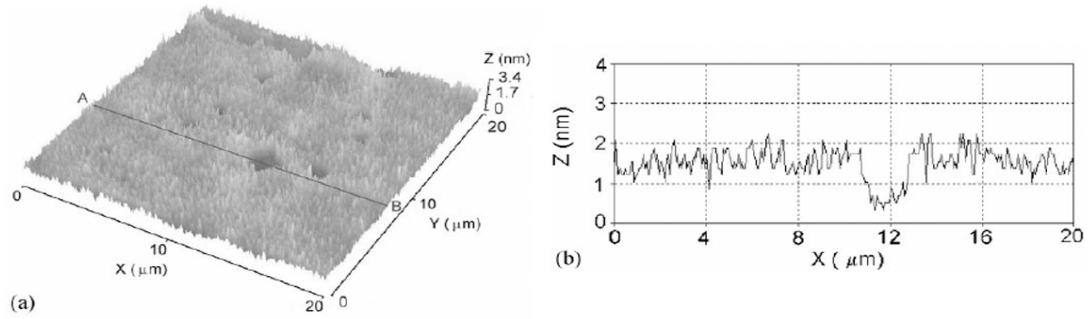

Figure 21. (a) AFM image of a $C_{60}(OH)_{12}$ film transferred to a mica surface, (b) corresponding film profile [157].

1.8 Microaggregates of fullerene C60 (rods and tubes)

Thin single-crystalline fibers consisting of C_{60} or "nanowhiskers" of C_{60} (C_{60}(NW)) were found in a colloidal solution of lead zirconate titanate (PZT) with the addition of C_{60} [158]. C60(NW) belong to the category of fullerene nanofibers (FNF). FNFs are thin fibers consisting of C_{60}, C_{70}, endohedral fullerenes or other fullerene molecules with functional groups. FNFs have a diameter of less than 1000 nm, and their length to diameter ratio is greater than three.

FNFs can have a single-crystalline, polycrystalline, or amorphous polymer structure. C_{60}(HW) are crystalline FNIs and are usually single crystalline. C_{60}(NW) is also called fullerene nanorods or fullerene nanowires [159–164]. Since their discovery, many works have been published on the creation of one-dimensional nanostructures based on fullerene molecules with unique properties. FNFs have a wide range of lengths from several micrometers to several millimeters or more.

Lead zirconate titanate (PZT) is a well-known ferroelectric ceramic material widely used in sensors and actuators. Fine fibrous precipitates were observed in PZT ash containing C_{60}. These fibrous structures have been identified as monocrystalline fibers composed of C_{60} and called C_{60} nanowhiskers [165]. The PZT solution contained toluene as the C_{60} solvent and isopropyl alcohol as the metal alkoxide solvent. A control experiment was conducted using isopropyl alcohol and a solution of C_{60} in toluene, where an interface was formed between the C_{60} solution and isopropyl alcohol in a transparent glass bottle [42]. Fine C_{60} precipitates appeared at the liquid-liquid interface and grew into long C_{60} nanocrystals about 1 mm in

length. This method of preparing C_{60}(NW) is called the liquid-liquid interfacial precipitation (LLIP) method.[42].

The authors of [166] were the first to synthesize C_{60} nanotubes (C_{60}(NT)) using the holes of a porous burning oxide membrane as a template. The resulting C_{60}(NT) were polycrystalline. The first single-crystalline nanotubes consisting of C_{60} or C_{70} were obtained by the MIL method by the authors [167,168]. Below are micrographs of this structure. (figure 22). The TEM image shows that C_{60}(NTs) have an outer diameter of several hundred nanometers and an inner diameter of several tens of nanometers to several hundred nanometers. The enlarged image (figure 22(b)) indicates the uniformity and straightness of C_{60}(NT).

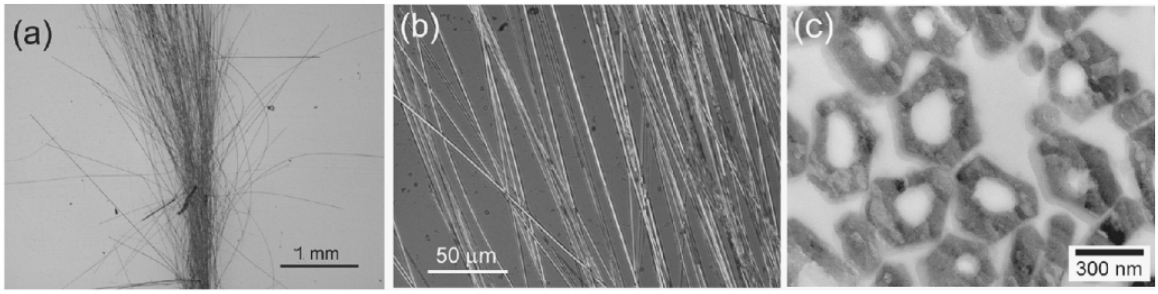

Figure 22. C_{60} nanotubes prepared by liquid-liquid interfacial deposition method. (a) and (b) - optical micrographs, (c) - TEM cross-sectional image [169].

The LLIP method has the following advantages:

(1) Synthesis can be carried out at room temperature in air.

(2) Various elements can be doped into nanofibers in solution.

(3) There is no need for expensive experimental equipment.

(4) Multicomponent FNFs consisting of various types of fullerene molecules can be obtained.

(5) The diameters of the FNFs can be changed by changing the types of solvents and the growth temperature.

(6) The MIL method can be used to obtain not only FNF, but also finely dispersed powders and nanosheets of fullerene [170].

The growth of C_{60}(NW) is noticeably enhanced when illuminated with room light [171]. In addition, it turned out that the growth of C_{60}(NW) was significantly promoted by irradiation of the solution with light with a wavelength from 600 to 625 nm [172].

C_{60}(NW) is prepared using the LLIP method as follows: 5 ml of a saturated solution in C_{60} toluene is poured into a transparent glass bottle, and 5 ml of isopropyl alcohol is carefully

added to it so that a liquid-liquid interface is formed. The liquid temperature is set below 21 °C. Small fullerene crystals nucleate at the liquid-liquid interface. The glass bottle is capped and stored for several days or more to grow C_{60}(NW) at temperatures below 25°C in an incubator. C_{60}(NW) obtained using this method turn out to be continuous [172].

Nanotubes consisting of fullerenes (C_{60} and C_{70}) can be made in a similar way. A typical procedure for obtaining fullerene C_{70} nanotubes is as follows: prepare 2 ml of a saturated solution of C_{70} in pyridine and place it in a transparent glass bottle, carefully add 6 ml of isopropyl alcohol to the pyridine solution to form a liquid-liquid interface at a temperature of about 10 ° C, after which the bottle is kept at 10°C in an incubator for several days [168].

The synthesis of C_{60}(NT) turns out to be more complex than C_{60}(NW). In this case, single-crystalline C_{60}(NT) can be synthesized using a modified method described in [43,169,173–175]. A saturated solution of C_{60} in pyridine is prepared. The fresh solution is purple in color but gradually turns brown. The color change is a prerequisite for the synthesis, which is greatly accelerated when illuminated with UV-visible light. 3 ml of brown C_{60} solution is placed in a transparent glass vessel with a capacity of 50 ml, 27 ml of isopropyl alcohol (IPA) is added, vigorously mixed in an ultrasonic bath for 1 min and kept in an incubator at 10 ° C. C_{60}(NT) appears at the bottom of the bottle after a few days [43].

The nucleation and growth process of C_{60}(NT) has been extensively studied for the effects of light illumination and temperature. [43]. As a result, the formation of C_{60}(NT) was noticeably improved when the initial solution of C_{60} in pyridine was illuminated with visible (436 nm) or ultraviolet light (UV, 302 nm). When the solution was illuminated with UV light, C60(NT) were formed in one day at all ratios of the volume of solution in pyridine to the volume of isopropyl alcohol (1:10, 1:9, 1:8, 1:7, 1:6) at a temperature of 5 ° C, while higher growth temperatures of 10°C and 15°C required more incubation time.

If a solution of C_{60} in pyridine was illuminated with visible light at a wavelength of 436 nm, it took longer to obtain C_{60}(NT) than in the case of irradiation with UV light. Thus, the nucleation of C_{60}(NT) is determined by supersaturation and the size of the cluster of C_{60} molecules in solution. The average diameter of C_{60}(NT) also varies depending on the volume ratio of the C_{60} solution in pyridine and IPA, i.e. finer C60 fibers were obtained by decreasing the amount of IPA added to the C_{60} solution in pyridine.

The procedure for the synthesis of C_{60}(NT) was significantly improved by changing the wavelength of light illuminated by the starting solution of C_{60} in pyridine. The highest yield (30–38 mg/l) of C_{60}(NT) was obtained when the solution was illuminated with light with a wavelength of 370 nm, which corresponds to the maximum absorption peak of solid C_{60} [169]. However, high yields (21–27 mg/L) of C_{60}(NT) were also obtained in the wavelength range 600–800 nm, where light absorption is lower.

The MIL method can also be used to produce C_{60} nanosheets [170]. C_{60} nanosheets of various sizes were synthesized using a solution of C_{60} in CCl_4 and alcohols (isopropyl alcohol, ethanol, methanol). The diameter of the resulting structures varies depending on the type of alcohol from 2.5 μm (C_{60} in CCl_4/ethanol) to 500 nm (C_{60} in CCl4/methanol). The liquid-liquid interface formed by a saturated solution of C_{60} and alcohol ensures the formation of nucleation centers. Heterogeneous nucleation centers can form not only at the liquid-liquid interface. The surface of solid materials, such as silicon, glass, or metal substrates, can be the site of nucleation of fullerene nanocrystals. For example, C_{60} nanocrystals were obtained by evaporating a fullerene solution on molybdenum, silicon or glass substrates, and thick columnar C_{60} crystals were obtained on a KBr substrate using a solution of C_{60} in benzene [176,177]. Авторы [178] синтезировали частицы C_{60}, напоминающие по форме цветы, на кремниевых подложках путем выпаривания капель раствора C_{60} в толуоле.

Chapter 2 Experimental Section

2.1 Preparation and characteristics of fullerenol $C_{60}(OH)_{30}$

Fullerenol C60(OH)X (X = 30 ± 2) was obtained at the St. Petersburg Institute of Nuclear Physics named after B.P. Konstantinov and was subsequently used without purification. For simplicity, it will be further denoted as $C_{60}(OH)_{30}$. The IR spectrum (figure 23) contains bands indicating the presence of hydroxyl groups attached to the fullerene core. An infrared spectrometer with Fourier transform (FSM 1201 LLS "Monitoring", Russia) was used.

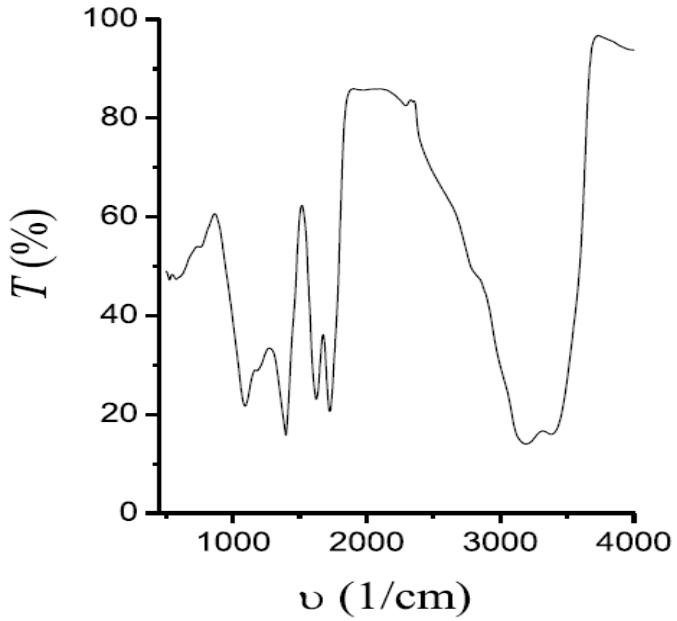

Figure 23. IR spectrum of fullerenols C60(OH)X (X = 30 ± 2).

The band at 1620 cm^{-1} corresponds to C-O stretching vibrations; weak bands at 1081 and 1390 cm^{-1} should be attributed to bending vibrations of bound C-O-H groups. The band at 1724 cm^{-1} is attributed to vibrations of C-C bonds in fullerenols, and the intense band at 3281 cm^{-1} should be associated with vibrations of the hydroxyl group associated with the core.

2.2 Preparation and characteristics of fullerenol $C_{60}(OH)_{20}$

The synthesis of fullerenol $C_{60}(OH)_{20}$ was carried out according to a scheme similar to the scheme for the synthesis of the more hydrophilic $C_{60}(OH)_{30}$. Thermal analysis (laboratory tubular furnace SNOL 0.2/1250 with a programmable thermostat, SNOL Therm, Russia) showed that fullerenol molecules contain 20 ± 1 hydroxyl group.

2.3 Preparation and characteristics of carboxyfullerene $C_{60}(C(COOH)_2)_3$

The preparation of carboxyfullerene was carried out according to the method described in [179]. The resulting carboxyfullerene was characterized by IR spectrometry on a Fourier transform spectrometer (FSM 1201 LLS “Monitoring”, Russia) and thermal analysis using a SNOL 0.2/1250 device (Snol-Term, Russia). The IR spectrum (figure 24) has a band at 623.5 cm^{-1}, corresponding to out-of-plane bending vibrations of the single O-H bond. The band at 1137 cm^{-1} corresponds to vibrations of the polar covalent bond C - O. Stretching vibrations of the C = O bond correspond to the band at 1720 cm^{-1}.

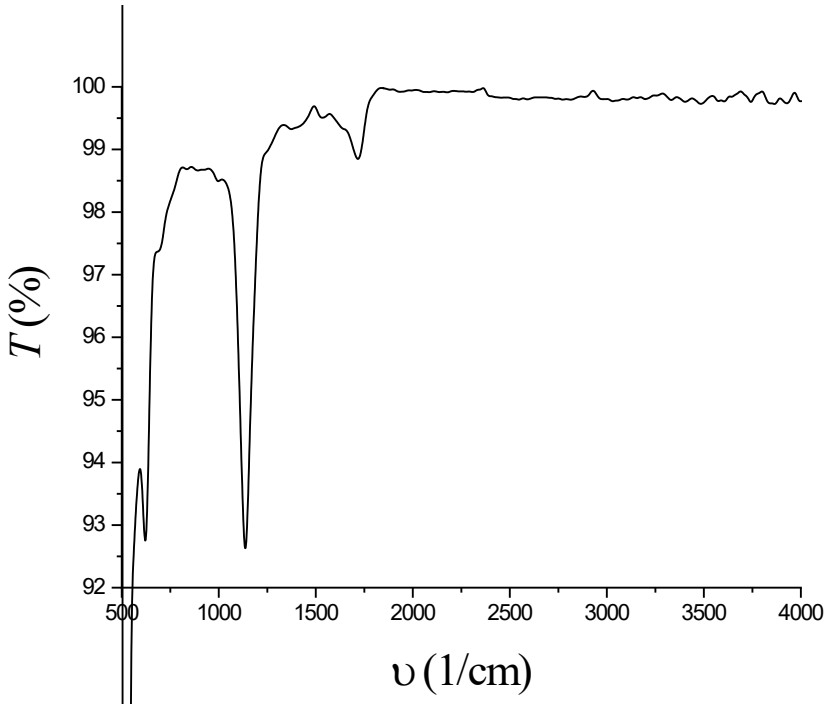

Figure 24. IR spectrum of carboxyfullerene $C_{60}(C(COOH)_2)_3$.

The content of carboxyl groups n was determined from the results of thermogravimetric analysis according to the following dependence

$$n = \frac{720}{x}\frac{m}{y} \quad (1)$$

where x and y are weight loss in% at temperatures of 170 and 570 °C, respectively, m is the molecular weight of the substituent.

From x = 9.0 and y = 25.3 it follows that n = 5.7 ≈ 6.

Thus, the chemical formula of the carboxyfullerene under study can be approximately written as $C_{60}(C(COOH)_2)_3$, although small impurities $C_{60}(C(COOH)_2)_2$ are also possible.

2.4 Preparation of C_{60} microaggregates of various shapes

Rod-shaped fullerene aggregates or microrods (MRC_{60}) were obtained using the LLIP method in accordance with the procedure described in [180] 40 ml of a saturated solution of C60 in toluene was prepared and placed in a 100 ml beaker. 40 mL of isopropyl alcohol was carefully added to the C60 solution using a pipette at approximately 21 °C, ensuring that the two solvents did not mix. At the same time, brown precipitates began to form.

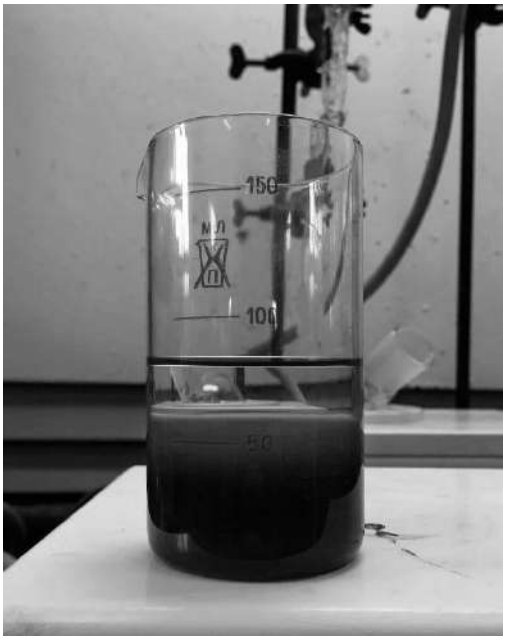

Figure 25. Reaction mixture during the synthesis of MRC_{60}.

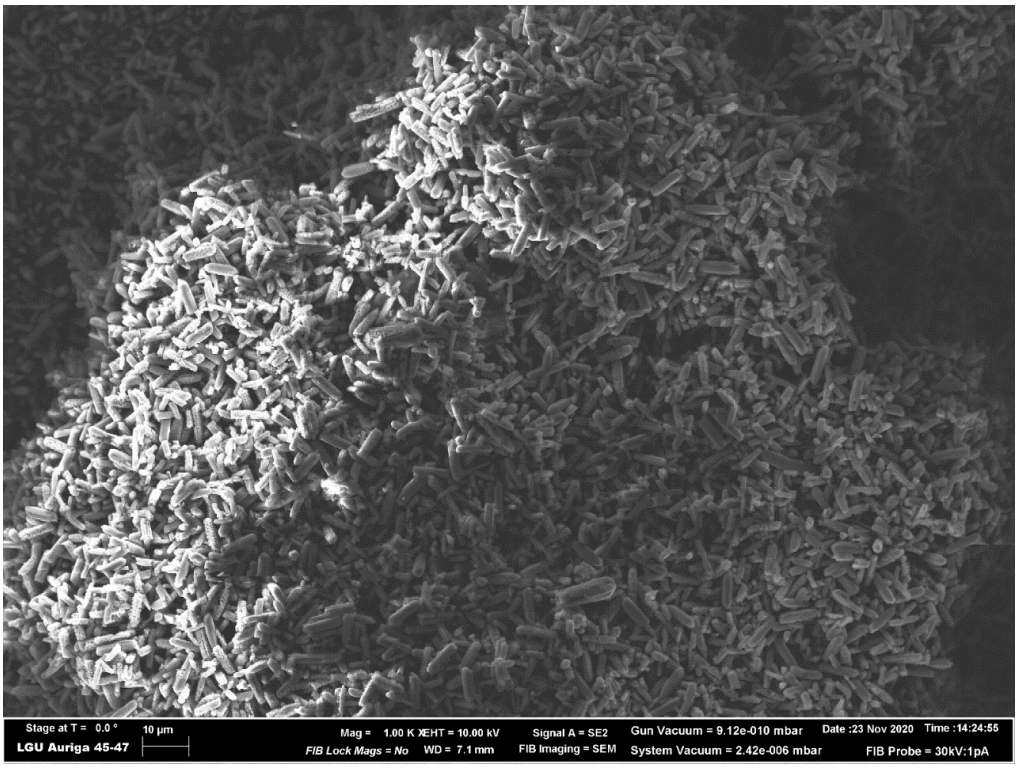

Figure 26. SEM micrograph of MRC_{60} obtained using the LLIP method.

The mixture was left undisturbed for several days. The fine brown precipitate at the bottom of the beaker was filtered off using a filter paper and dried at room temperature. The shape of the resulting aggregates was confirmed by scanning electron microscopy.

Tube-shaped fullerene aggregates or C_{60} nanotubes (NTC_{60}) were also obtained by the LLIP method based on the technique described in the work [181]. A saturated solution of C60 in pyridine was prepared (solubility 0.89 g/l). Dissolution occurred at 5 °C. Undissolved C60 was removed by filtration (filter pore size 450 nm). The prepared solution was exposed to visible light. A fresh solution of fullerene in pyridine had a purple color. It was considered ready for synthesis when the color changed to brown. Next, excess isopropanol (volume ratio 1:10) was slowly added on top of the fullerene solution. The mixture was prepared at a temperature of 5 °C. The alcohol and C60 solutions were cooled to 5 °C before mixing. The resulting mixture was sonicated for 1 minute, shaken 10 times by hand, and sonicated again for 1 minute, then stored at 5°C for several days. The shape of the resulting aggregates was confirmed by optical and scanning electron microscopy. (figure 27, figure 28).

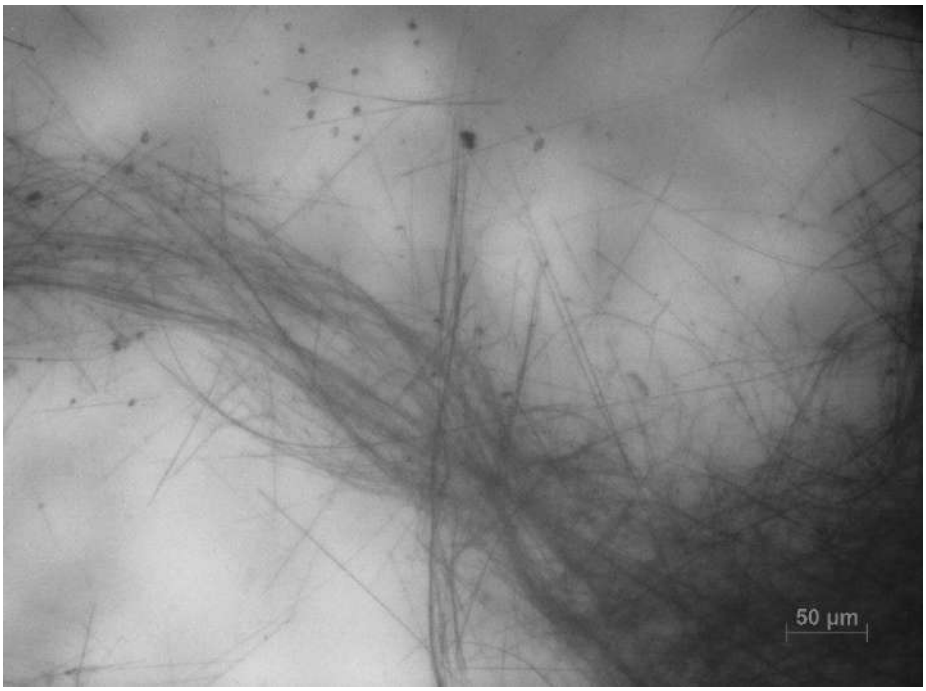

Figure 27. Microphotograph of NTC_{60} obtained by the LLIP method.

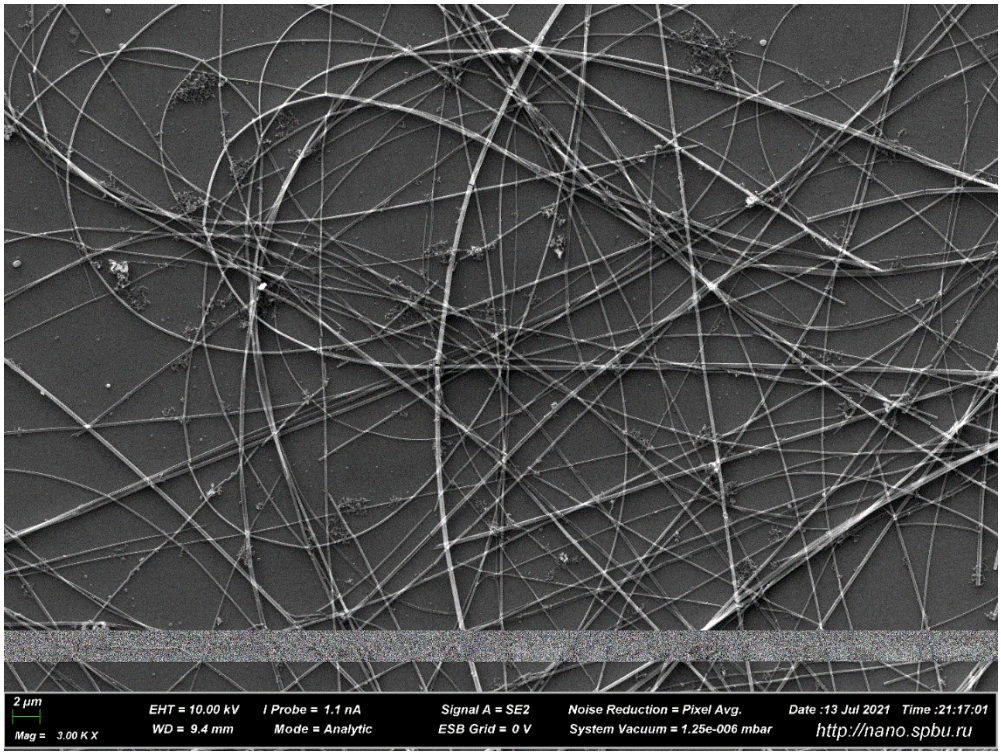

Figure 28. SEM-Microphotograph of NTC_{60} obtained by the LLIP method.

2.5 Preparation of solutions and formation of films on the water surface

All solutions of fullerenols $C_{60}(OH)_{30}$ and $C_{60}(OH)_{20}$ and carboxyfullerene $C_{60}(C(COOH)_2)_3$ were prepared in triple distilled water. A still, made of glass, was used for the last two stages of distillation. If aggregates were detected in the volume, the solution was treated in an ultrasonic bath for an hour immediately before the start of measurements. Solutions of polymers (PVP and PNIPAM) were also prepared in triple distilled water. Polymer solutions were stirred on a magnetic stirrer for 30 minutes before measurements. To form deposited films, solutions of fullerene, MRC_{60} in toluene, polymers (PVP and PNIPAM) in ethanol, and a dispersion of NTC_{60} in a solution of a mixture of pyridine and isopropyl alcohol in a ratio of 1:10 were used. The solvents were subjected to preliminary distillation. All applied films, except NTC_{60}, were formed by gradually dropping the solution onto the surface of the liquid using a syringe from Hamilton (Switzerland). Measurements of surface properties began 5 min after film deposition, the time required for the solvent to evaporate. The applied NTC_{60} films were formed by selecting 1 ml of their dispersion with a dispenser and then dropping it onto the surface of the liquid. Measurements began 15 min after surface formation.

2.6 Determination of surface tension by the Wilhelmy plate method

Surface tension was measured using the Wilhelmy plate method. When measuring surface tension by this method, a plate whose thickness is small compared to the perimeter of its horizontal section was placed in the liquid. The liquid, wetting the plate, formed a cylindrical unfolded meniscus along the perimeter. The plate was installed in such a way that the position of its lower edge coincided with the liquid level in the cuvette (figure 29).

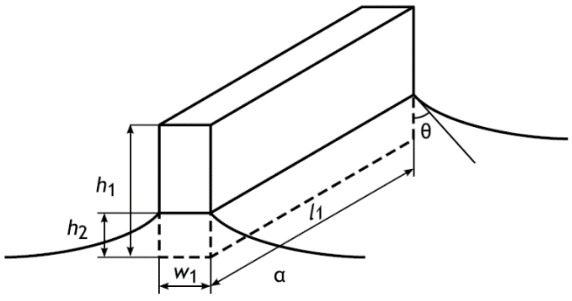

Figure 29. Pulling out a Wilhelmy plate, partially immersed in liquid.

The formation of the meniscus is due to the effective force of surface tension, which tends to pull the plate into the depth of the liquid. The total force required to hold a partially submerged plate in the liquid can be calculated using the equation

$$F_\gamma = P\gamma \cos\theta + g l_1 w_1 h_1 \rho_1 - g l_1 w_1 h_2 \rho_\alpha \quad (2)$$

where ρ_1, ρ_α – densities of the plate and solution, respectively; h_2 – depth of immersion of the plate into the liquid; g – gravitational acceleration, w_1, l_1, h_1 – thickness, length and height of the plate, respectively.

The second term on the right side of this equation represents the weight of the plate, and the third is the Archimedes force acting on its immersed part. The difference between the forces holding the plate at the same level in positions when its lower edge is at the level of the liquid and when it is at a depth h_2 is equal to

$$\Delta F = P\gamma \cos\theta - g l_1 w_1 h_2 \rho_\alpha \quad (3)$$

Thus, when $h_2 = 0$ the force difference is determined as follows

$$\Delta F = P\gamma \cos\theta \quad (4)$$

There are many varieties of the method, differing in different ways of determining ΔF. In this work, this value was determined using electronic scales at the moment when the immersion depth $h_2 = 0$.

2.7 Determination of dynamic surface elasticity using the oscillating barrier method

This method for determining dynamic surface elasticity is based on recording fluctuations in the surface tension of the liquid under study in a cuvette (Langmuir bath). Before measurements, the aqueous solution under study, in some cases after pretreatment in an ultrasonic bath, was placed in a cuvette. Immediately before the start of measurements, the surface was renewed using a water-jet pump and a Pasteur pipette, after which oscillations of the barrier were excited, which were recorded on a computer.

Complex dynamic surface elasticity was measured at a fixed frequency of 0.1 Hz. Fluctuations in the surface area of the solution in a Langmuir bath made of polytetrafluoroethylene (PTFE) were created by a movable PTFE barrier sliding along the polished edges of the cuvette. The moving part of the mechanical vibration generator was connected to the barrier with a steel rod. The barrier slid back and forth along the Langmuir bath and produced oscillations of the liquid surface with the required relative amplitude (2.5%, 5%, 7.5%). The induced fluctuations in surface tension γ were measured by the Wilhelmy plate method described above. Complex dynamic surface elasticity ε was calculated using the following relationship

$$\varepsilon(\omega) = \frac{\delta\gamma}{\delta \ln A} \quad (5)$$

where δγ and δA are the increments of surface tension and surface area, respectively.
If the phase shift between fluctuations in surface area and surface tension is known, then it is possible to determine the real and imaginary parts of the dynamic elasticity of the surface, which in the general case is a complex quantity.

2.8 Measurements of surface pressure and dynamic surface elasticity using the KSV NIMA device

Measurements of surface pressure and dynamic surface elasticity of solutions of fullerene complexes with PNIPAM, as well as mixed films of fullerene with PVP and PNIPAM, were also carried out on an ISR device (KSV NIMA, Finland) (figure 30). Fluctuations in the surface area of the liquid in a fluoroplastic cuvette (1) were excited by the reciprocating movement of two fluoroplastic barriers (2) along the surface of the cuvette. Surface pressure was determined by a Wilhelmy plate (3) suspended on an electronic balance (4). Fluctuations in surface tension were recorded in the PC memory and displayed on the monitor screen (5). Dilational surface elasticity was calculated in the same way as in the case of the standard oscillating barrier method described above. The oscillation frequency of the two barriers used was 30 MHz. During measurements, the barriers oscillated in antiphase

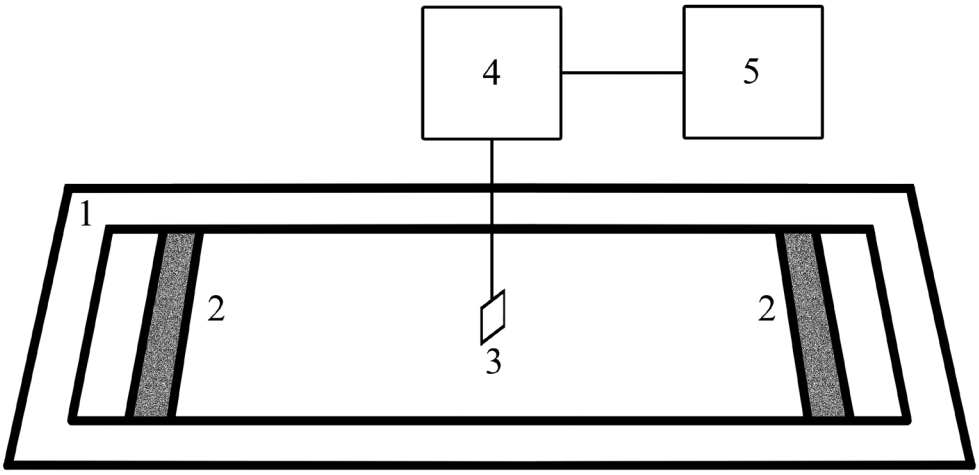

Figure 30. Diagram of the KSV NIMA device (Finland): 1 – fluoroplastic cuvette, 2 – fluoroplastic barriers, 3 – platinum plate, 4 – electronic scales, 5 – PC.

The test solution was poured into a fluoroplastic cuvette (1) with an area of 690 × 75 mm^2. In the case of deposited films, the test substance was applied with a microsyringe from Hamilton (Switzerland) by dropping onto the surface of water or a polymer solution. The change in surface concentration could also occur due to the movement of barriers (2) towards each other at a constant speed to a minimum surface area of 30 × 75 mm^2.

2.9 Determination of attenuation coefficient and length of capillary waves

Capillary waves were excited on the surface of the liquid in a fluoroplastic cuvette. Approximately in the middle of the cuvette, a metal blade was fixed in a special microlift clamp, with which you can smoothly change the distance between the blade and the surface of the liquid in the range of 0.5 - 10 mm. When an alternating electric field is created between the liquid and the blade, capillary waves are excited at the surface of the liquid with a frequency corresponding to the frequency of the alternating voltage. In the experimental setup used, an alternating sinusoidal voltage of a given frequency from a standard precision low-frequency generator GZ-110 is supplied to a special circuit for generating high-voltage pulses. This circuit consists of a power amplifier, a step-up transformer and a half-wave rectifier. A sinusoidal signal is input to this circuit. The rectifier suppresses the signal for half the period. As a result, a periodic high voltage signal (about 400 V) of the same frequency appears at the output. One output of this circuit is connected to the blade, the other is connected to a platinum

wire immersed in liquid. This allows you to create an alternating electric field in the gap between the surface of the liquid and the blade.

The laser beam mounted on a movable optical stage passes through a translucent mirror, is reflected from mirror 3 and falls vertically down onto the surface of the liquid (figure 31). The reflected beam hits the displacement sensor, passing through a system of mirrors 3–4. If capillary waves propagate over the surface of the liquid, the reflected beam performs harmonic oscillations along the surface of the sensor 5, which converts the optical signal into alternating voltage. The frequency of the resulting electrical signal is equal to the frequency of capillary waves. The amplitude of the sinusoidal signal is proportional to the amplitude of the waves A for small deviations of the shape of the liquid surface from the plane.

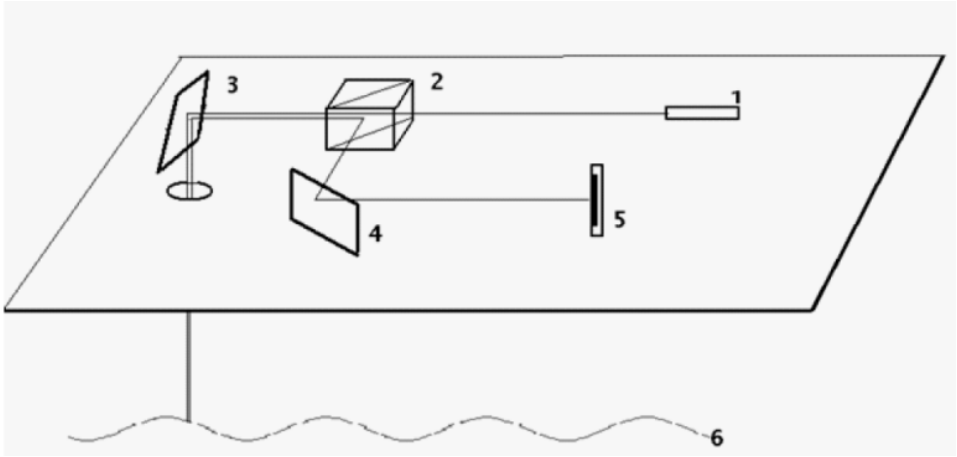

Figure 31. Optical diagram of the setup for determining the characteristics of capillary waves: 1 – laser, 2 – translucent glass, 3 and 4 – mirrors, 5 – beam position sensor, 6 – liquid surface.

To improve the signal-to-noise ratio, the signal is amplified by a selective amplifier. Its function is to cut out a narrow band from the broadband spectrum of the signal in the vicinity of a given frequency of capillary waves. As a result, at the output of the selective amplifier, the signal I is determined by the relation

$$I = KA\exp(-\alpha X) \tag{6}$$

where K – proportionality coefficient; X is the distance between the projection of the blade on the surface of the liquid and the point of incidence of the laser on this surface; A - amplitude.

The point of incidence of the beam on the surface of the liquid can be brought closer and further away from the blade generating capillary waves by moving the stage by rotating

the microscrew on which the entire optical circuit is attached. Thus, it is possible to change the distance X. If the proportionality coefficient does not depend on X, then the attenuation coefficient of capillary waves α can be calculated from the relation

$$\alpha = -\left(\frac{d\ln(I)}{dX}\right) \tag{7}$$

If an electrical signal from the output of a selective amplifier is applied to the Y input of the oscilloscope, and a sinusoidal signal from the G3-110 generator (figure 32) is applied to the X input of the oscilloscope, then you can observe a Lissajous figure on the screen, which will be an ellipse, since the frequency of the two signals is the same. When moving the optical stage, the laser beam passed through points on the surface of the liquid for which the phase of the signal from the generator and amplifier coincided or differed by a multiple of π. In this case, the ellipse is flattened, and a line can be observed on the screen. Such points on the surface of the liquid are separated from each other by an integer number of wavelengths.

The signal from the input of the selective amplifier is also fed to the MP-370 computer oscilloscope-recorder. It records the dependence of the signal on distance X as a csv file in the computer memory and presents this dependence as a graph on the monitor screen.

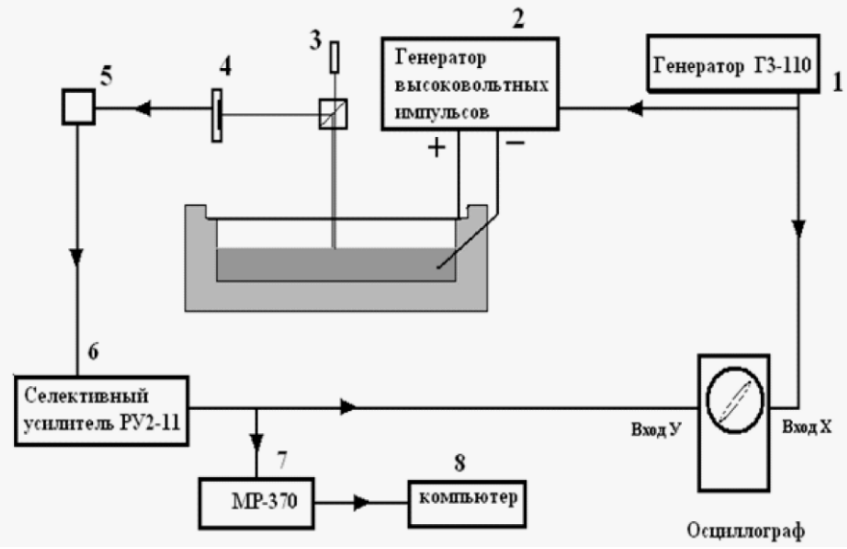

Figure 32. Electrical circuit of the installation for measuring the characteristics of capillary waves. 1 – precision low-frequency signal generator G3-110, 2 – high-voltage pulse generator, 3 – laser, 4 – optical laser beam position sensor, 5 – pre-amplifier, 6 – selective amplifier RU2-11, 7 – two-channel computer oscilloscope – MR recorder –370, 8 – computer.

The attenuation coefficient and capillary wavelength were then calculated using MATLAB. All measurements of dynamic surface properties began after cleaning the surface using a moving barrier and a Pasteur pipette connected to a pump.

2.10 Study of films on water surfaces using microscopy at the Brewster angle

Brewster angle microscopy is a type of optical microscopy that uses linearly polarized light incident on a reflective surface at a Brewster angle to form an image. The installation diagram is shown in the diagram (figure 33). The Brewster angle is the angle of incidence at which the reflected beam will be completely polarized in a plane perpendicular to the plane of incidence.

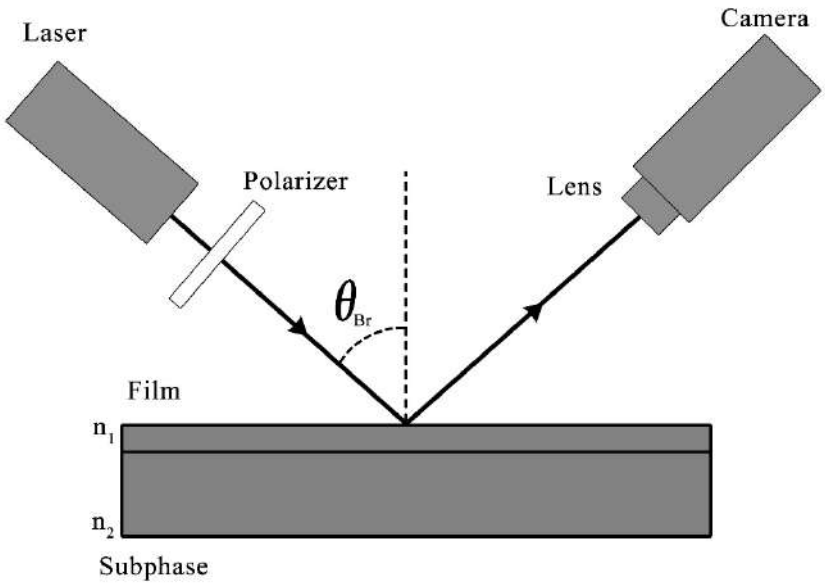

Figure 33. Schematic diagram of Brewster angle microscopy.

In this case, the use of a polarizer makes it possible to prevent the reflected beam from hitting the photodetector. Small changes in the refractive index of an adsorption film or deposited film on a liquid surface result in a change in the Brewster angle, and hence macroscopic discontinuities in the liquid surface become visible. The morphology of the adsorption layers of fullerene derivatives was studied in situ using a Brewster angle microscope, BAM1 (NFT, Göttingen, Germany), equipped with a 10 mV He-Ne laser. The test solution was placed in a

Langmuir bath and equilibrated at room temperature. The measurements were carried out in a Langmuir fluoroplastic bath with a barrier.

2.11 Langmuir-Schaeffer method for transferring surface films to a solid substrate

The Langmuir-Schaeffer method was used to transfer the adsorption or deposited film from an aqueous surface to a solid substrate. Mica plates with a fresh surface were used as a substrate. To obtain a fresh surface, the mica plate was split immediately before use. Using tweezers, the plate was placed parallel to the plane of the cuvette with the test solution and then touched the surface. Next, excess liquid was removed with filter paper, and the sample was placed in a desiccator to dry for several days. The dried samples were examined using atomic force microscopy.

2.12 Application of atomic force microscopy to study the morphology of films obtained by the Langmuir-Schaeffer method

Atomic force microscopy (AFM) is a type of probe microscopy, which is based on the interaction of a sharp probe and the surface under study. At a distance of about one angstrom, repulsive forces arise between the sample atoms and the probe atom attached to the cantilever, and at larger distances ¬ – forces of attraction. The cantilever, moving along the surface under study, records its relief. Needles, the tip of which has a radius of the order of several tens of nm, are used as probes.

To study the surface morphology of the samples in this work, devices operating in the semi-contact mode were used. In this case, forced oscillations of the cantilever are excited near resonance with an amplitude of 10 – 100 nm. When scanning a sample in this mode, changes in the amplitude and phase of cantilever oscillations are recorded.

All samples were examined on an NTEGRA Prima device (NT-MDT, Russia).

2.13 Application of ellipsometry to study films on water surfaces

Elliptically polarized light can be represented as the sum of two linearly polarized components, the electric field strength vectors of which oscillate in two mutually perpendicular

planes P and S. These strength components Ep and Es can be represented as:

$$E_s = |E_s|e^{i\delta_s}, E_p = |E_s|e^{i\delta_p} \quad (8)$$

where: δ_s, δ_p – phase angles for these components of the electric field strength vector.

Reflection of light from a surface lead to a change in the phase and amplitude of two components of light, changes in which depend on the optical properties of the surface under study, and can be characterized by two ellipsometric angles

$$\tan\Psi = \frac{|E_p{}^r|/|E_s{}^r|}{|E_p{}^i|/|E_s{}^i|}, \ \Delta = (\delta_p{}^r - \delta_s{}^r) - (\delta_p{}^i - \delta_s{}^i) \quad (9)$$

where r and i are the indices of the reflected and incident rays, respectively.
The angles Ψ and Δ are related to the complex reflection coefficients of the two components of elliptically polarized light R_p and R_s

$$R_p = \frac{|E_p^r|}{|E_p^i|}e^{i(\delta_p^r - \delta_p^i)}, \ R_s = \frac{|E_s^r|}{|E_s^i|}e^{i(\delta_s^r - \delta_s^i)} \quad (10)$$

Using these quantities, we can write the basic equation of ellipsometry:

$$\tan\psi e^{i\Delta} = \frac{R_p}{R_s} \quad (11)$$

The ratio of reflection coefficients depends on parameters such as: angle of incidence Θ, wavelength λ, refractive indices of the contacting phases and the surface film, and the thickness of this film h. The exact form of the dependence of ellipsometric angles on the given parameters is determined within the framework of the model for the specific system under study. Thus, it is possible to calculate the refractive index n_f and the film thickness h using the measured values of the ellipsometric angles Ψ and Δ.

In the case when there is a thin isotropic layer of an adsorbed substance of constant density on the surface of a one-component solution, the surface concentration Γ can be

calculated using the equation [182]

$$\Gamma = \frac{h*(n_f - n_0)}{dn/dC} \quad (12)$$

where n_0 и n – and n are the refractive indices of the solvent and solution, respectively; C is the concentration of the dissolved component.

In this case, the difference in angles Δ for the solution and the pure solvent ($\Delta_s = \Delta - \Delta_0$) is approximately proportional to the surface concentration [183].

In this work, measurements of the kinetic dependences of ellipsometric angles were carried out using a Multiskop null ellipsometer (Optrel GBR, Germany). The radiation source in this device is a He-Ne laser with a wavelength of 632.8 nm (figure 34).

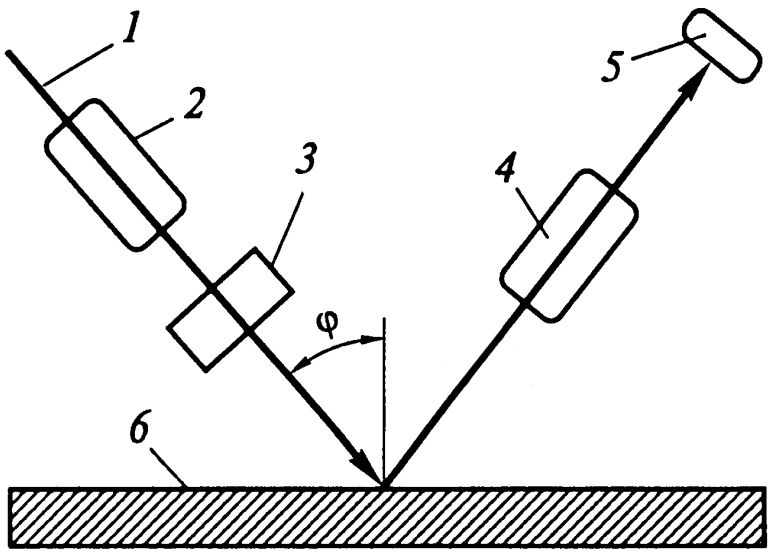

Figure 34. Schematic diagram of a null ellipsometer.

The laser beam (1), passing through the polarizer (2), changes the polarization to linear. Next, the beam passes through the compensator (3), which is a crystal ¼ wavelength thick and has the property of birefringence, changing the polarization to elliptical. Next, the beam is reflected from the surface under study (6) and, passing through the analyzer (4), hits the detector (5). To determine the ellipsometric angles, the positions of the polarizer and analyzer are found that correspond to the minimum light intensity on the detector. In this work, measurements were carried out at an incidence angle of 50°, close to the Brewster angle.

2.14 Determination of film morphology using optical microscopy

Оптический микроскоп использует систему линз для создания увеличенных изображений небольших объектов. Объект помещается на предметный столик и может наблюдаться непосредственно через окуляр микроскопа. Камера используется для захвата изображения микрообъекта (микрофотография). Ряд объективов с разным увеличением обычно устанавливаются на турели, что позволяет поворачивать их на место и обеспечивает возможность увеличения изображения. В данной работе исследование пленок на водной поверхности проводилось посредством их наблюдения в кювете Ленгмюра с подвижными барьерами. Образцы агрегатов фуллерена в форме трубок исследовались посредством наблюдения капли образца, нанесенной между двух предметных стекол. Изучение образцов проводилось на приборе Carl Zeiss Axio Scope A1.

2.15 Study of film morphology using transmission electron microscopy (TEM)

Transmission electron microscopy involves studying thin samples by using a beam of electrons to pass through and interact with them. Electrons passed through the sample are focused onto an imaging device: a fluorescent screen, photographic plate, or CCD (charge-coupled device) camera sensor. In this work, this method was used to study aggregation in the bulk of a solution of fullerenol $C_{60}(OH)_{30}$ and on the surface of a PVP solution on which a film of pure fullerene was deposited. A copper grid coated with a thin nitrocellulose film was used as a substrate. Samples for research were prepared by distributing a drop of the test fullerenol solution over the substrate or using the Langmuir–Schaefer method. The samples were then dried in a desiccator for several days.

2.16 Study of film morphology using scanning electron microscopy (SEM)

A scanning electron microscope is a type of electron microscope that creates images of a sample by scanning a surface with a focused beam of electrons. The electrons interact with atoms in the sample, creating various signals that contain information about the surface

topography and composition of the sample. The electron beam is scanned as a raster image, and the position of the beam is combined with the intensity of the detected signal to create an image. In the most common SEM mode, secondary electrons emitted by atoms excited by the electron beam are detected using a secondary electron detector (Everhart–Thornley detector). The number of secondary electrons that can be detected, and hence the signal intensity, depends, among other things, on the topography of the sample. Some SEMs can achieve resolutions above 1 nanometer. In this work, measurements of samples of C_{60} fullerene aggregates were carried out using a Zeiss SUPRA 40VP scanning electron microscope.

Chapter 3 Surface properties of solutions of fullerene derivatives C_{60}

3.1 Surface properties of fullerenol $C_{60}(OH)_{30}$ solutions

The use of TEM made it possible to detect a noticeable amount of dense compact aggregates in dilute aqueous solutions of $C_{60}(OH)_{30}$ [184]. In the microphotograph of a fullerenol film on the surface of nitrocellulose, formed as a result of drying a drop of a fullerenol solution with a concentration of 0.2 g/l (figure 35 you can see a system of interconnected dark spots of irregular shape. The number of spots increases in the direction from the upper right corner to the lower left corner. This is the direction in which a drop of solution is drawn in during the drying process. Although the upper right corner of the micrograph appears to be brighter and more uniform. Even in this part of the image one can observe several spots darker than the light thin elongated areas between them. The characteristic size of spots in this region is about 20 nm. The morphology of the film in the upper right corner probably corresponds to a C60(OH)30 monolayer with cracks formed during the drying process. The average layer thickness increases towards the lower right corner, where dark spots may correspond to multilayer spots. In some micrographs, relatively dense aggregates with an average size of about 100 nm could be observed. These rare aggregates cannot affect the surface properties of the solutions under study.

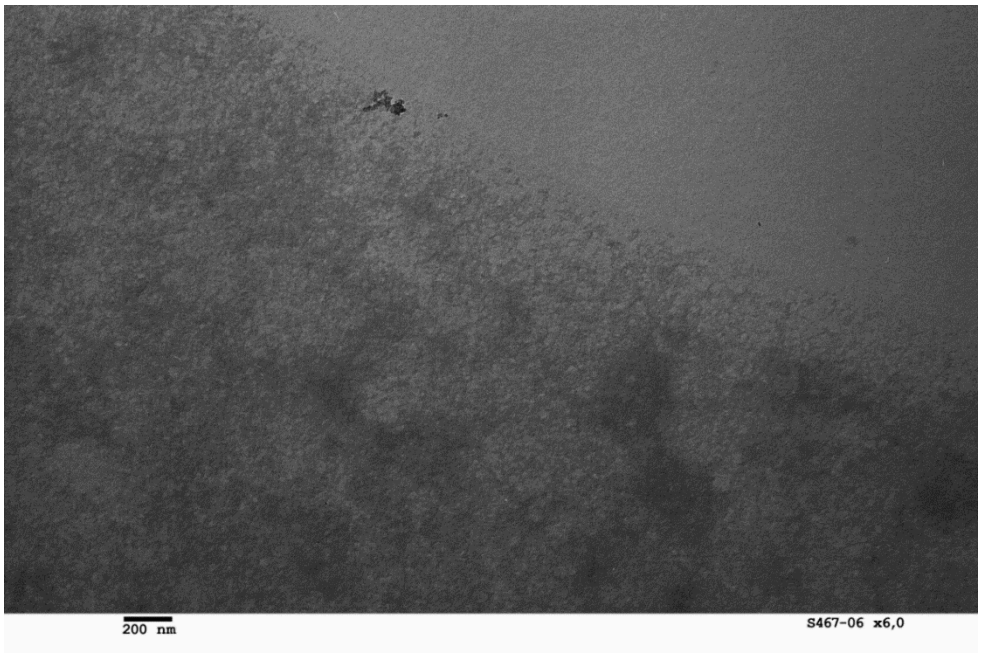

Figure 35. TEM micrograph of a $C_{60}(OH)_{30}$ fullerenol film on the surface of a nitrocellulose layer.

The surface pressure of a fullerenol solution with a concentration of 0.1 g/l equally leads to errors for more than a day after the formation of the surface and begins to noticeably stand out with the age of the surface only at higher concentrations (figure 36), as well as dynamic surface elasticity (figure 37). At a concentration of 0.5 g/l, an induction period is observed when the surface elasticity remains almost unchanged for about two hours and then increases significantly. This effect indirectly indicates the heterogeneity of the adsorption layer at the beginning of adsorption, when adsorbed molecules form small islands of the surface condensed phase, and the surface elasticity begins to increase only with an increase in the size and/or number of islands, and they begin to interact [185]. Surface properties increase slowly over about a day, peak and then decrease (figure 36, figure 37). If the surface pressure does not exceed 9 mN/m, then the surface elasticity at an vibration amplitude of 7.5% and a frequency of 0.1 Hz can reach high values of approximately 140 mN/m at concentrations above 0.2 g/l. Nonmonotonic changes in surface properties appear to be caused by a break in surface area fluctuations. The beginning of the decrease in surface properties coincides with the resumption of oscillations after a break. A decrease in surface pressure and dynamic surface elasticity under the influence of fluctuations in surface area is a characteristic feature of adsorbed layers of solid nanoparticles and is not observed during the adsorption of conventional surfactants, amphiphilic macromolecules and soft nanoparticles [186,187].

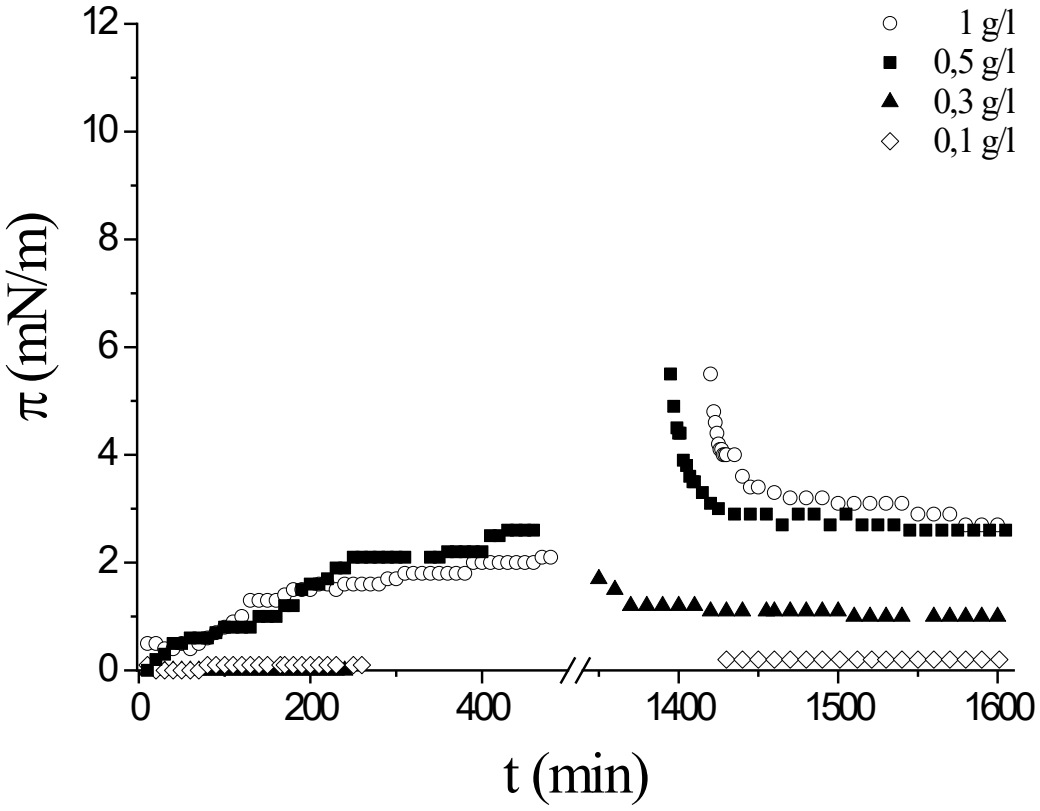

Figure 36. Kinetic dependences of surface pressure at various concentrations of solutions of fullerenol $C_{60}(OH)_{30}$: 1 (circles), 0.5 (squares), 0.3 (triangles), 0.1 g/l (diamonds).

This effect is due to the partial destruction of the structure of the fragile adsorption layer under the influence of external mechanical influences, leading to the formation of individual sections of multilayers and a decrease in surface elasticity. A concomitant decrease in the number of hydrophobic groups in the near region of the surface layer can lead to an increase in surface tension. A strong drop in surface properties after the maximum was not observed for layers of fullerene derivatives with arginine and lysine, where the fullerene core is surrounded by a thin corona of amino acid residues [156]. The discovered feature of fullerenol films indicates a greater sensitivity of the adsorption layer to mechanical disturbances. This effect was weaker for complexes of silica nanoparticles with an oppositely charged surfactant, where greater attraction between particles in the surface layer can be assumed [186].

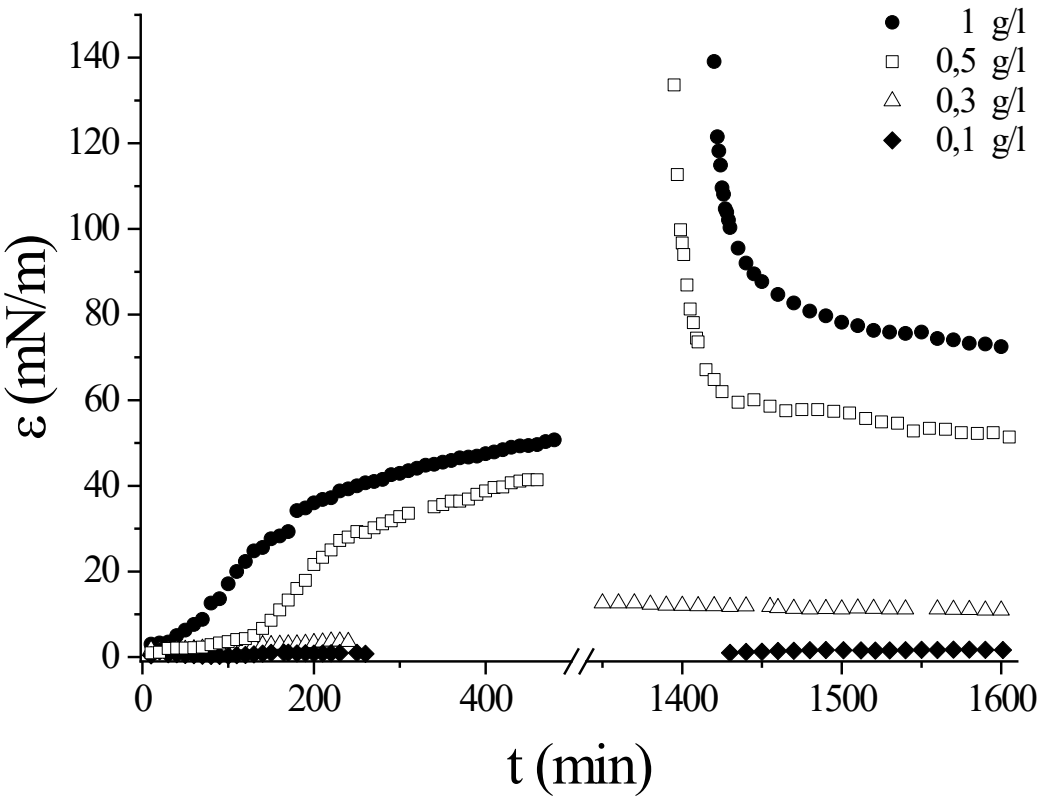

Figure 37. Kinetic dependences of dynamic surface elasticity at various concentrations of solutions of fullerenol $C_{60}(OH)_{30}$: 1 (circles), 0.5 (squares), 0.3 (triangles), 0.1 g/l (diamonds).

Compression of the adsorbed layer in a Langmuir cell leads to a sharp increase in surface pressure and dynamic surface elasticity, followed by relaxation. When approaching equilibrium, the surface properties do not reach their values before compression, which indicates an increase in the stationary surface concentration. The relaxation of surface properties is probably caused not by desorption of adsorbed fullerenols, but by some structural rearrangement leading to denser packing in the surface layer. Replacing the fullerenol solution in the subphase with pure water does not lead to noticeable changes in surface properties, which indicates the irreversibility of adsorption.

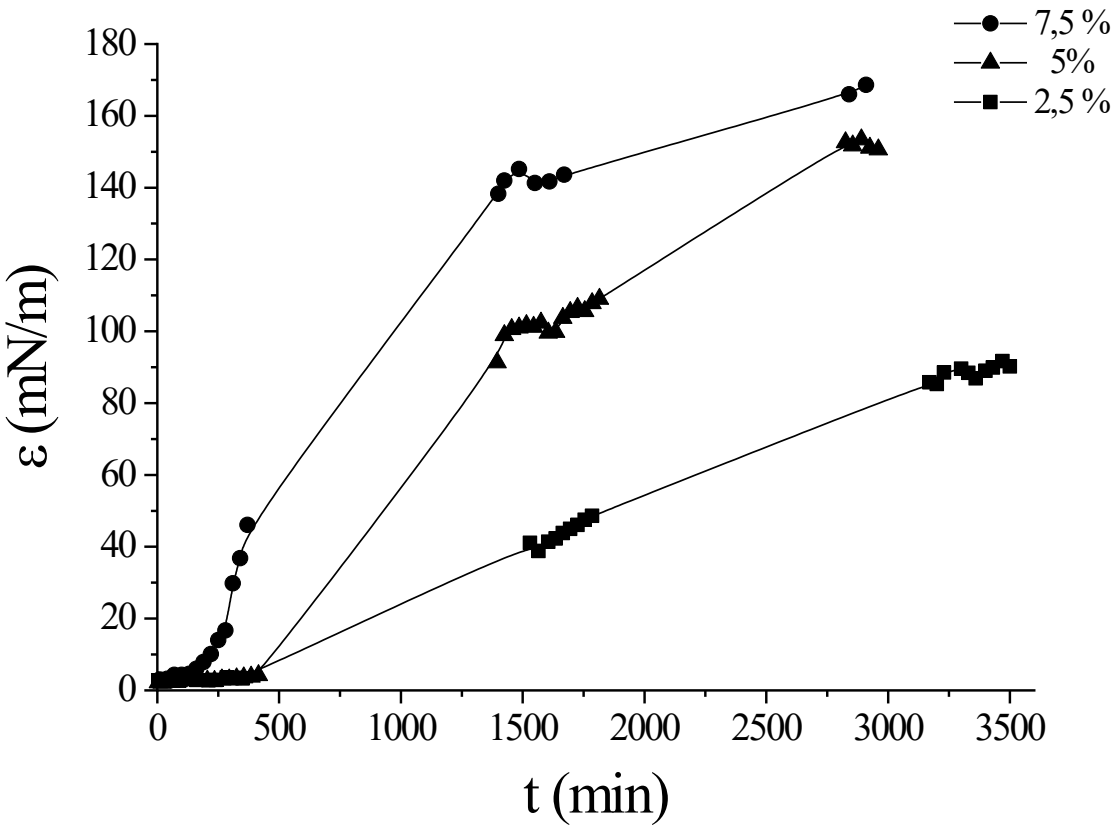

Figure 38. Kinetic dependences of the dynamic surface elasticity of a solution of fullerenol $C_{60}(OH)_{30}$ at a concentration of 0.2 g/l and at various vibration amplitudes: 7.5% (circles), 5% (triangles), 2.5% (squares).

Dynamic surface elasticity decreases greatly as the amplitude of surface area oscillation increases from 2.5 to 7.5%, and the range of oscillation amplitudes corresponding to the linear response of the system to surface tension corresponds to smaller deformations (figure 38). Quite surprisingly, the surface pressure also decreases when the amplitude reaches 7.5%. These results obviously represent a consequence of significant structural rearrangements in the adsorption layer even with minor external disturbances. Oscillations of greater amplitude lead to stronger destruction of the adsorption layer, to a greater number of cracks and multilayer aggregates in it, and thus to lower dynamic elasticity of the surface and lower surface pressure.

The high sensitivity of the adsorption layer to small mechanical disturbances leads to the fact that the total time of oscillation of the surface area affects the kinetic dependences of dynamic surface elasticity. It increases more rapidly within a few hours of surface formation if the area fluctuations are interrupted between measurements, approximately every 30 minutes. The effect of surface area fluctuation time on the kinetic dependences of surface properties can be more complex with longer measurements.

The expected microscopic heterogeneity of $C_{60}(OH)_{30}$ adsorption films does not affect their macroscopic morphology, and Brewster angle microscopy shows only a homogeneous surface of fullerenol solutions even 48 hours after surface formation (figure 39a). Sharp compression of the surface does not lead to visible deformations of the adsorption layer, but lightly touching the surface with a thin stick leads to noticeable changes in the surface morphology immediately after the disturbance (figure 39b). The adsorbed layer regains its homogeneity over the next few minutes, indicating the liquid-like properties of the film.

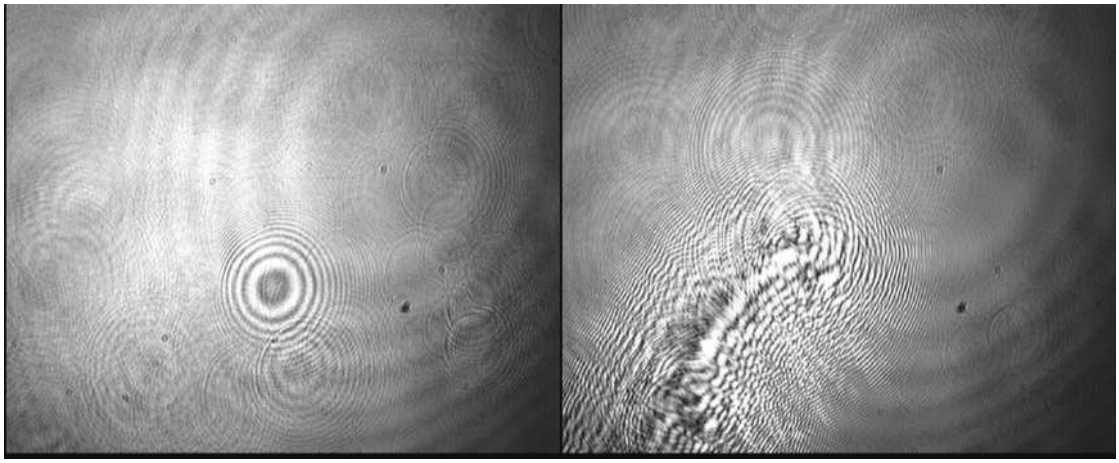

a) b)

Figure 39. Images of the adsorption film of fullerenol $C_{60}(OH)_{30}$, obtained using a microscope at Brewster angle, with a solution concentration of 1 g/l: a) 48 hours after surface formation; b) after disturbing the surface with a thin stick.

The surface concentration of fullerenols after surface formation increases faster than dynamic surface elasticity and surface tension. The ellipsometric angle Δ, approximately proportional to the surface concentration, is equal to the equilibrium value within error approximately 7 hours after surface formation at a concentration of 0.2 g/L (figure 40). This means that small changes in the total surface concentration when approaching equilibrium can lead to significant changes in surface elasticity due to structural rearrangements in the surface layer.

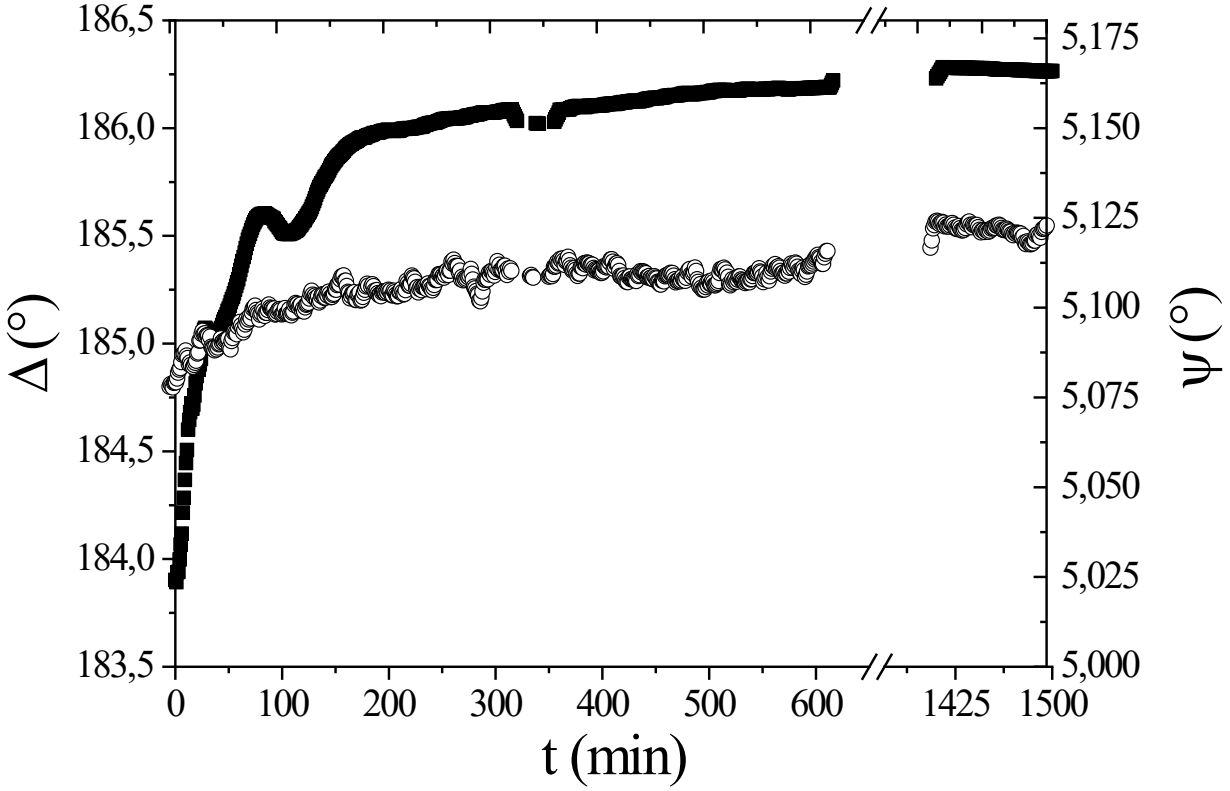

Figure 40. Kinetic dependences of ellipsometric angles Δ (squares) and ψ (circles) for a solution of fullerenol $C_{60}(OH)_{30}$ at a concentration of 0.2 g/l.

The ellipsometric signal fluctuates for more than three hours after surface formation (figure 40). These chaotic changes in the signal can be associated with the macroscopic heterogeneity of the adsorption layer, probably due to the formation of multilayer formations, as well as with the fluidity of the layer at the first stage of adsorption. The movement of macroscopic sections of the adsorption layer of different densities near the spot of the ellipsometer laser beam on the surface of the liquid can lead to these fluctuations, which disappear quite sharply when the surface density reaches a certain critical value, when the adsorption layer becomes stationary.

From the kinetic dependences of the ellipsometric angles (figure 40) it is clear that the characteristic adsorption time is on the order of several hours and significantly exceeds the characteristic time τ of surfactant diffusion from the bulk phase to the surface. The last value can be estimated using the following relation [188]

$$\tau = \frac{\left(\frac{\Gamma}{c}\right)^2}{D} \quad (1)$$

where c is the volume concentration; G is the surface concentration (adsorbed substance); D is the diffusion coefficient.

The diffusion coefficient of fullerenol $C_{60}(OH)_{30}$ can be calculated, knowing the particle radius R, using the Stokes–Einstein equation. The radius for $C_{60}(OH)_{30}$ is 6.5 Å [131], which leads to the value D = 3,29*10^{-10} $м^2с^{-1}$. If we make the assumption that fullerenol molecules form a monolayer with dense packing at the interface, then the following relation can be used for the surface concentration

$$\Gamma = \frac{m}{\lambda \pi R^2} \quad (2)$$

where m = 1230 u - mass of a fullerenol molecule; λ = 1.102 - coefficient corresponding to the densest packing of circles in the plane.

Calculations using relations (1) and (2) give τ = 0.15 s at c = 0.2 g/l. This is only an approximate estimate, based on the assumption of the formation of a compact monolayer of fullerenol at the interface during the adsorption of individual molecules. However, violation of the first assumption cannot lead to a change in τ by more than an order of magnitude. The second assumption also seems reasonable, since the concentration of large aggregates can be neglected. At the same time, the calculated value is several tenth orders of magnitude less than the estimate from the data (figure 39) and, therefore, indicates that the adsorption of fullerenol is not controlled by diffusion. The observed adsorption slowdown may be caused by an electrostatic adsorption barrier due to the negative charge of $C_{60}(OH)_{30}$. The first adsorbed molecules create an electric field, leading to the repulsion of adsorbing molecules, which also carry a negative charge.

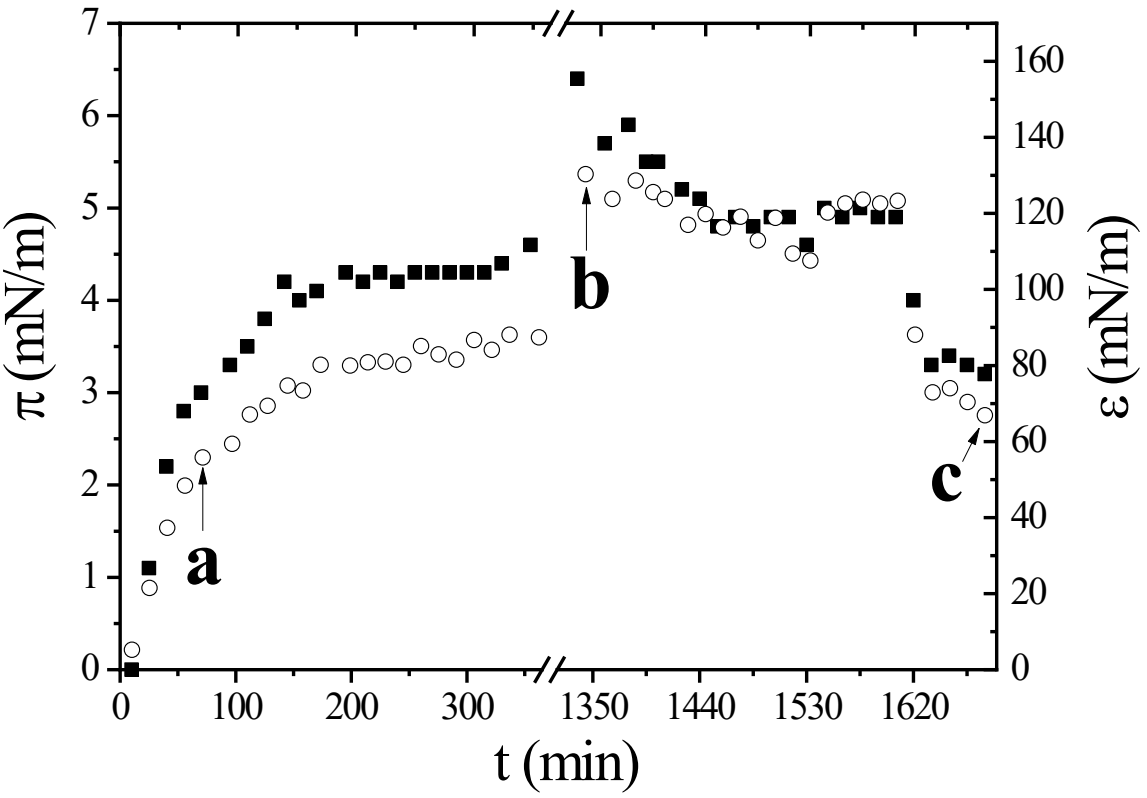

Figure 41. Kinetic dependences of surface pressure (squares) and dynamic surface elasticity (circles) for a solution of fullerenol $C_{60}(OH)_{30}$ at a concentration of 0.5 g/l. Letters and thin arrows indicate the moments of film transfer to the mica surface by the Langmuir-Schaeffer method.

To study the structure of adsorption films of fullerenol, they were transferred from the liquid surface to a freshly cleaved mica surface using the Langmuir–Schaefer method and examined by AFM. The arrows on the kinetic dependence (figure 41) show the values of surface properties at the moment the layer is transferred from the surface of a solution with a concentration of 0.5 g/l. For the obtained samples, the corresponding AFM images are presented (figure 42). Approximately an hour after the surface is formed, the film consists of interconnected aggregates 2–3 nm thick and individual empty areas on the mica surface (figure 42a). AFM does not reliably estimate the width of the aggregates, but it is greater than the thickness, and therefore the surface aggregates represent separate sections of bi- and triloes. Direct comparison of AFM images with TEM micrographs (figure 35) is difficult due to the different physical principles of the two methods. On the other hand, the thickness of the surface aggregates in the AFM image (figure 42a), is likely greater than the thickness of the gray spots in the TEM micrograph (figure 35), indicating a difference in the objects in these

figures. Therefore, it can be assumed that aggregates in the adsorption layer at the liquid-gas interface are not adsorbed from the bulk phase, but are formed in the surface layer as a result of rearrangements of adsorbed molecules.

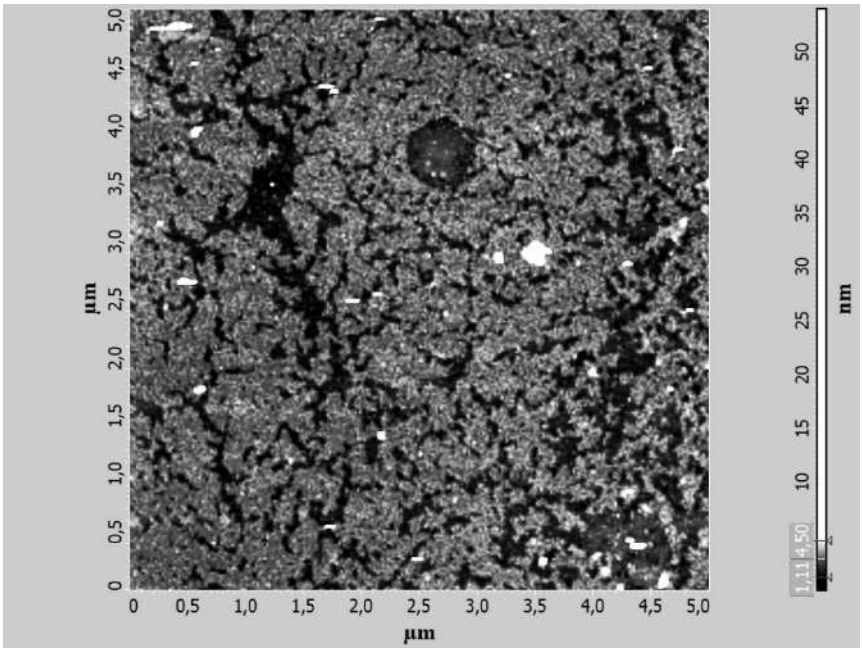

a)

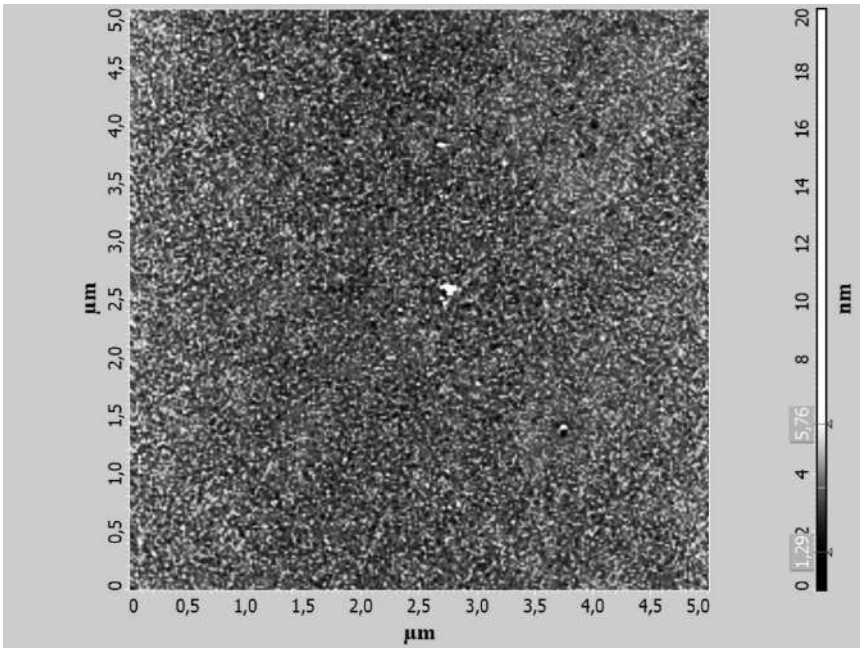

b)

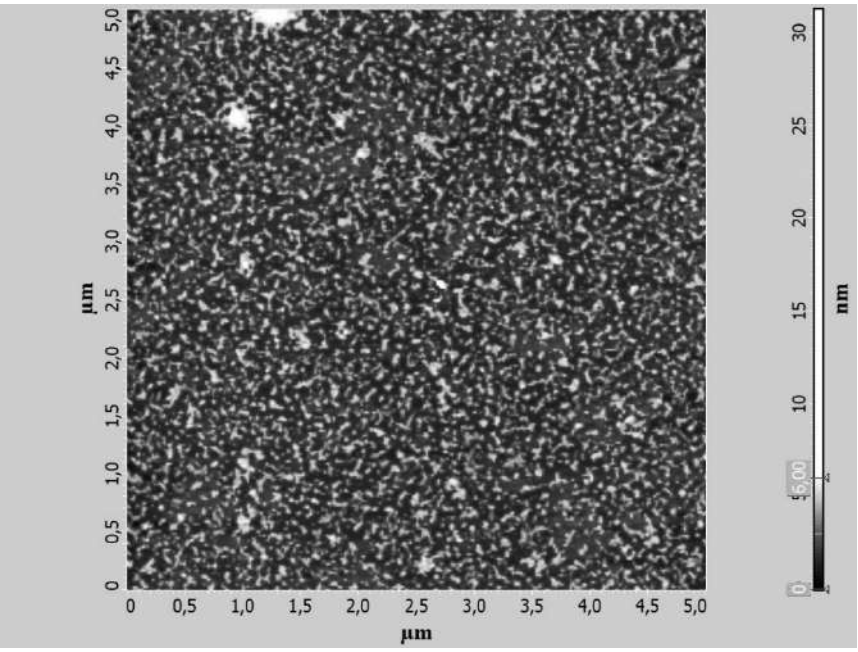

c)

Figure 42. AFM images of various samples of $C_{60}(OH)_{30}$ fullerenol film: a) 70 min after surface formation; b) 16 hours after the formation of the surface without vibrations; c) after continuous vibrations for 75 minutes.

About a day after the formation of the surface, the adsorption layer becomes denser (figure 42b), but retains the main features of the structure. The film consists of a large number of small aggregates with some voids between them. In this case, the dynamic surface elasticity is approximately two times higher than the value corresponding to the AFM image (figure 42a). If the adsorption layer is subjected to continuous fluctuations in surface area for more than an hour, the continuous structure of the layer breaks down into pieces and cracks of different widths and dense areas between them are observed in the layer (figure 42c), in accordance with the conclusions from measurements of dynamic surface elasticity. In this case, the surface elasticity drops from approximately 125 to 65 mN/m, and the surface pressure also decreases (figure 41).

Although the surface activity of fullerenol $C_{60}(OH)_30$ is low and it does not significantly reduce surface tension at low concentrations, its molecules form a macroscopically homogeneous adsorption layer with high dynamic surface elasticity at the solution-air interface. values up to 170 mN/m. Despite the relatively low molecular weight of fullerenol, the surface properties of its solutions are more reminiscent of the properties of dispersions of solid nanoparticles than of surfactant solutions, and are very sensitive to small mechanical disturbances of the surface. As a result, the adsorption layer is characterized by a nonlinear

response to even minor fluctuations in surface area. These vibrations can lead to destruction of the continuous structure of the surface and the formation of cracks between dense areas of the layer. AFM shows that the adsorption layer at the microlevel is heterogeneous and consists of interconnected surface microaggregates consisting of two to three layers of fullerenol molecules. The bonds between different aggregates are relatively weak and can be broken even by minor mechanical stress, although high surface elasticity means that the overall structure is characterized by a significant response to deformation. Surface aggregates are not adsorbed from the bulk phase, but are formed in the surface layer as a result of structural rearrangements of adsorbed molecules. Slow adsorption of fullerenols is controlled by an electrostatic barrier.

3.2 Surface properties of fullerenol $C_{60}(OH)_{20}$ solutions

The range of studied concentrations of fullerenol $C_{60}(OH)_{20}$ coincides with the corresponding range for solutions of fullerenol with 30 hydroxyl groups [189]. Kinetic dependences of surface tension and dynamic surface elasticity of $C_{60}(OH)_{20}$ solutions at a concentration of 0.5 g/l, an oscillation frequency of 0.1 Hz and an oscillation amplitude of 2.5% (figure 43) show that the surface tension changes slowly and reaches approximately 70 mN/m 6 hours after surface formation.

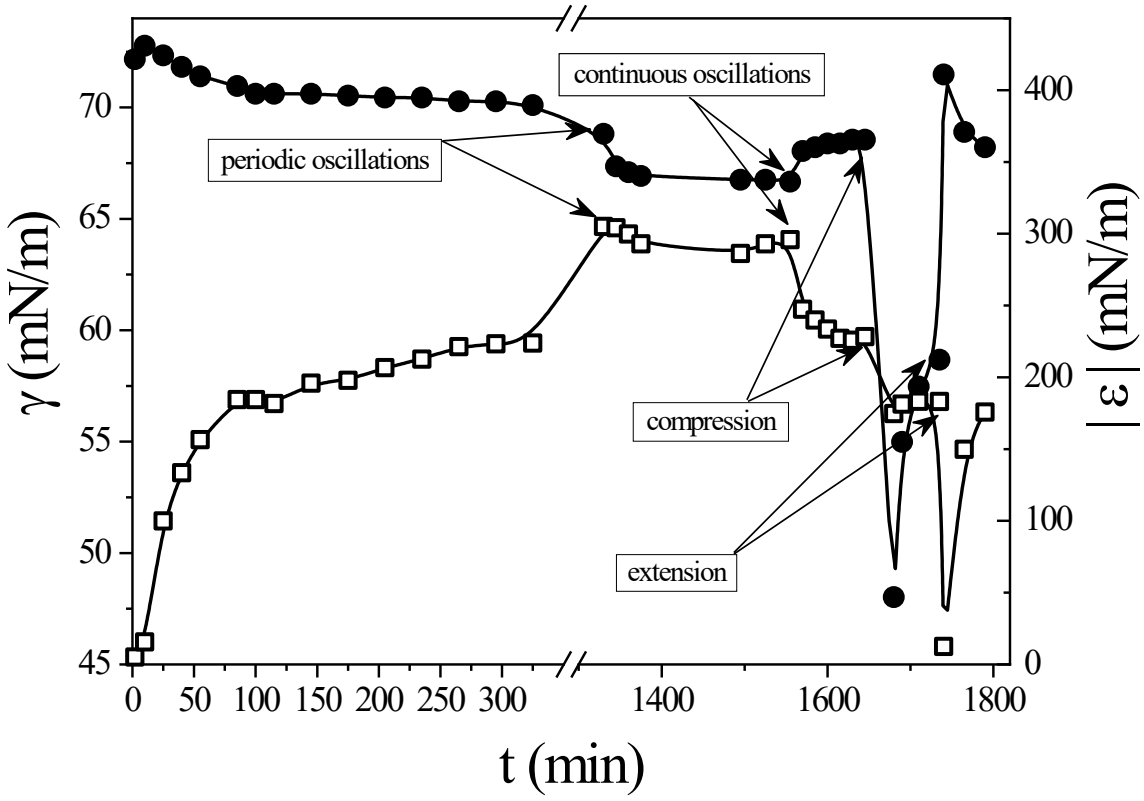

Figure 43. Kinetic dependences of surface tension (circles) and dynamic surface elasticity (squares) of $C_{60}(OH)_{20}$ solutions with a concentration of 0.5 g/l, an oscillation frequency of 0.1 Hz and an oscillation amplitude of 2.5%. Thin arrows mark the moments when periodic oscillations of the surface area are turned on after a break, when continuous oscillations of the surface area are turned on, and sharp compression and stretching of the surface, respectively.

Similar slow changes in surface tension were recently observed for solutions of fullerenols with fewer and more hydroxyl groups, as well as for solutions of fullerene derivatives with amino acidsи [156,157]. The induction period at the beginning of adsorption in this case indicates the heterogeneity of the adsorption layer [185]. In this case, the adsorbed molecules stick together, forming small, non-interacting islands at the interface, and the surface tension does not change noticeably. As the number and size of islands increase, they begin to interact, and the surface pressure and dynamic surface elasticity begin to increase. In the case of solutions of $C_{60}(OH)_{20}$ with a concentration of 0.5 g/l, in contrast to solutions of the more hydrophilic $C_{60}(OH)_{30}$, surface elasticity is close to zero only in the first minutes after the formation of the surface. After this, it begins to increase, reaching about 180 mN/m after an hour and about 300 mN/m after 22 hours (figure 43). These values significantly exceed the

dynamic surface elasticity of $C_{60}(OH)_{30}$ solutions due to the higher hydrophobicity of fullerenol $C_{60}(OH)_{20}$.

Six hours after the formation of the surface, when the surface elasticity reached about 220 mN/m, the adsorption film of $C_{60}(OH)_{20}$ was transferred from the surface of the solution to the surface of the mica using the Langmuir–Schaeffer method and examined by AFM (figure 44). t can be seen that the fullerenol film consists of more than one molecular layer (figure 44a). Each layer is composed of densely packed molecules and individual disk-shaped aggregates ranging in diameter from a few nanometers to about fifty nanometers. The thickness of the layers ranges from 0.5 to 1 nm and is thus close to the size of fullerenol molecules. The thickness of surface aggregates is higher and reaches 3 nm. The resulting high dynamic surface elasticity is characteristic of surface films of close-packed solid nanoparticles on the aqueous subphase and is probably a consequence of the formation of rigid multilayers [186,190].

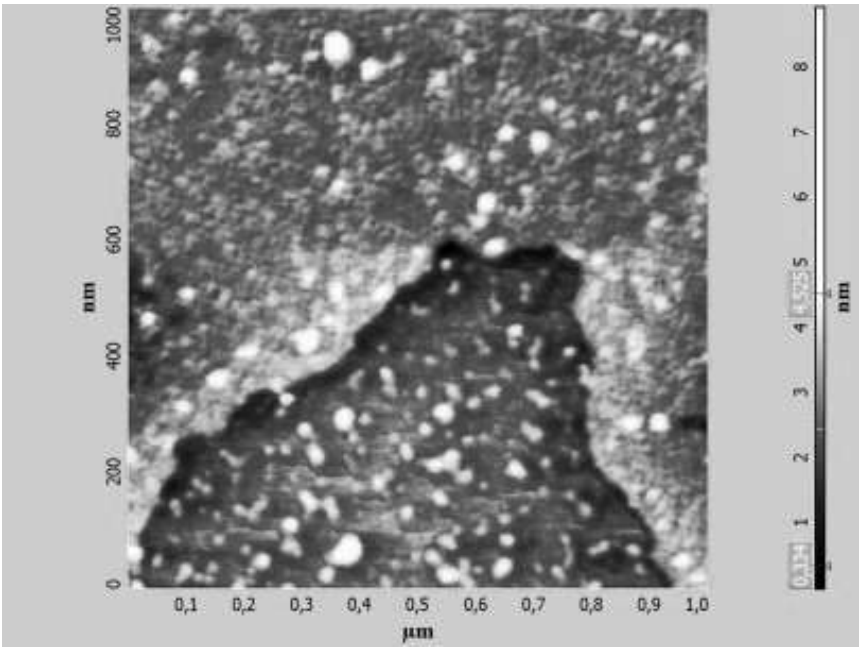

a)

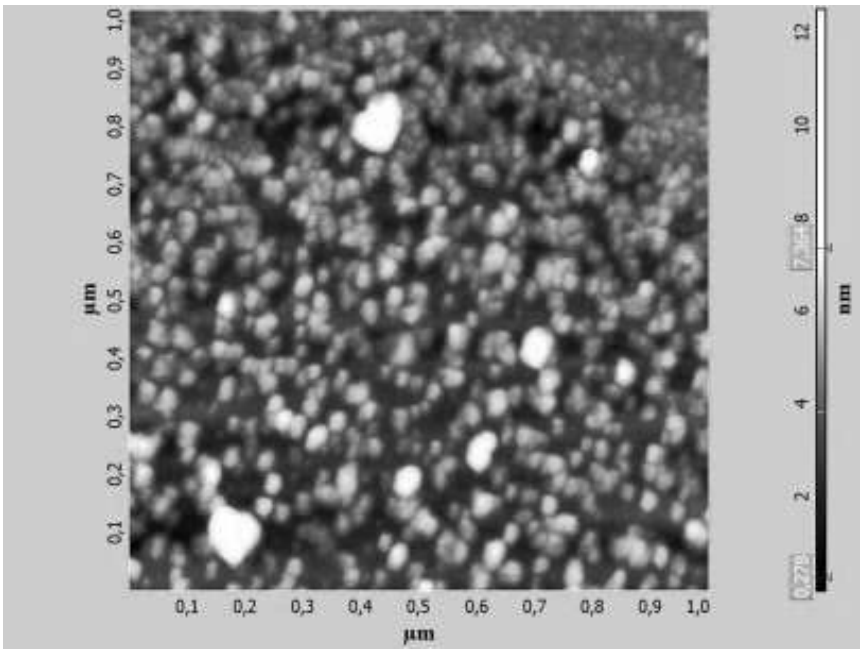
µm
0,1 0,2 0,3 0,4 0,5 0,6 0,7 0,8 0,9 1,0
µm
nm
0 2 4 6 8 10 12

b)

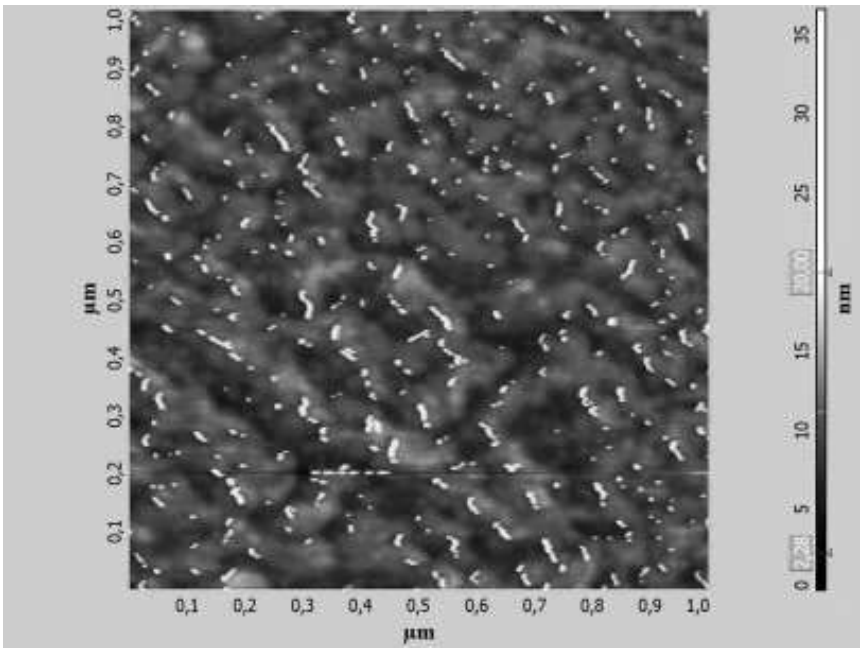
µm
0,1 0,2 0,3 0,4 0,5 0,6 0,7 0,8 0,9 1,0
µm
nm
0 5 10 15 20 25 30 35

c)

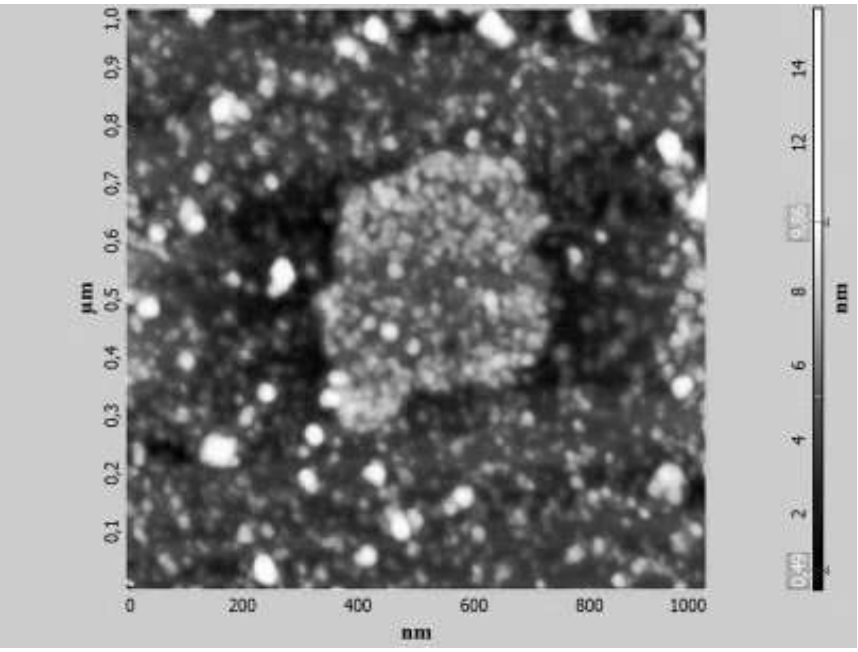

d)

Figure 44. AFM images of $C_{60}(OH)_{20}$ film samples transferred to a mica surface: a) 6 hours after surface formation; b) an hour after switching on continuous oscillations; c) one hour after compression of the surface d) one hour after expansion of the surface to the original surface.

After turning off continuous oscillations, surface elasticity continued to increase over the next sixteen hours without external mechanical influences (figure 43). Large changes in surface elasticity over the twenty-two hours of measurement were accompanied by only a slight decrease in surface tension of approximately 3 mN/m. The adsorption film was then transferred to the mica surface before further measurements. In this case, the AFM images of the layer are close to those presented (figure 44a) and indicate only a slight decrease in the concentration of aggregates. Subsequent inclusion of periodic oscillations of the surface area (five periods of oscillation every 15 minutes) did not lead to noticeable changes in surface elasticity. After this, continuous fluctuations in the surface area were initiated, and the dynamic surface elasticity began to decrease and reached about 220 mN/m. Continuous fluctuations in surface area also caused an increase in surface tension of approximately 1 mN/m. Such a response of the adsorption layer to fluctuations in surface area has not previously been observed for solutions of standard surfactants, amphiphilic polymers, and aqueous dispersions of soft nanoparticles, but is characteristic of aqueous dispersions of solid nanoparticles [183,186,191–193]. The observed changes in surface properties may be associated with partial destruction of the brittle fullerenol layer by mechanical disturbances of the liquid surface. A

similar behavior was previously observed for solutions of $C_{60}(OH)_{30}$, but was not observed for solutions of fullerene derivatives with arginine and lysine [156], which indicates the high sensitivity of the morphology of films of hydroxylated fullerene derivatives to surface vibrations. AFM data confirm this assumption. The AFM image of a layer transferred to the mica surface after turning off continuous vibrations shows a large number of individual aggregates and unfilled areas between them, presumably formed under the influence of these vibrations (figure 44b). The surface layer becomes looser, and the dynamic surface elasticity decreases by approximately 25% compared to the values before the inclusion of continuous oscillations.

Compression of the fullerenol film by 50% led to a sharp drop in surface tension to 47 mN/m and dynamic surface elasticity to 175 mN/m (figure 43). Subsequent relaxation for an hour resulted in only a slight increase in surface elasticity to 183 mN/m, but a more significant increase in surface tension to 60 mN/m. This behavior differs from the corresponding results for $C_{60}(OH)_{30}$ solutions, where surface stretching led to an increase in dynamic surface elasticity. This effect for $C_{60}(OH)_{30}$ solutions is associated with structural rearrangements leading to denser packing in the surface layer. In the case of the $C_{60}(OH)_{20}$ adsorption film, AFM images indicate the formation of elongated aggregates after compression (figure 44c). Their characteristic length is approximately 100 nm, and their thickness exceeds 10 nm. These sizes are approximately one decimal order higher than those of surface aggregates before compression. The simultaneous formation of some regions of reduced density between elongated aggregates may explain the decrease in the dynamic elasticity of the surface after compression, despite the increase in the total surface concentration. It can be assumed that the observed aggregates are formed during local destruction of the adsorption layer under compression, which leads to the formation of individual sections of multilayers. A similar morphology of the adsorption film was previously observed in mixed solutions of sodium polystyrene sulfonate and dodecyltrimethylammonium bromide when the surfactant concentration increased above a certain critical value [194].

Subsequent stretching of the surface in the Langmuir bath to the original area leads to a sharp increase in surface tension to the value for pure water and a simultaneous drop in dynamic surface elasticity to almost zero (figure 43). After this, the surface elasticity returns to pre-expansion values in less than an hour, and the surface tension approaches the value for an

undisturbed surface. Presumably, the adsorption layer, after stretching, breaks up into separate islands (surface aggregates), which do not interact with each other and thus have virtually no effect on the surface properties. Gradually, these large aggregates begin to disperse over the surface, and this process can be accompanied by further adsorption of fullerene, which leads to a decrease in surface tension and an increase in dynamic surface elasticity. AFM makes it possible to observe a large number of aggregates in the surface layer an hour after the surface is stretched (figure 44d), reminiscent of surface aggregates that fell an hour after the continuous oscillations were turned on (figure 44b).

A decrease in the concentration of fullerenol leads to a slowdown in changes in surface properties. A decrease in surface tension by no more than 1 mN/m occurs within 30 hours after surface formation at a $C_{60}(OH)_{20}$ concentration of less than 0.5 g/l.

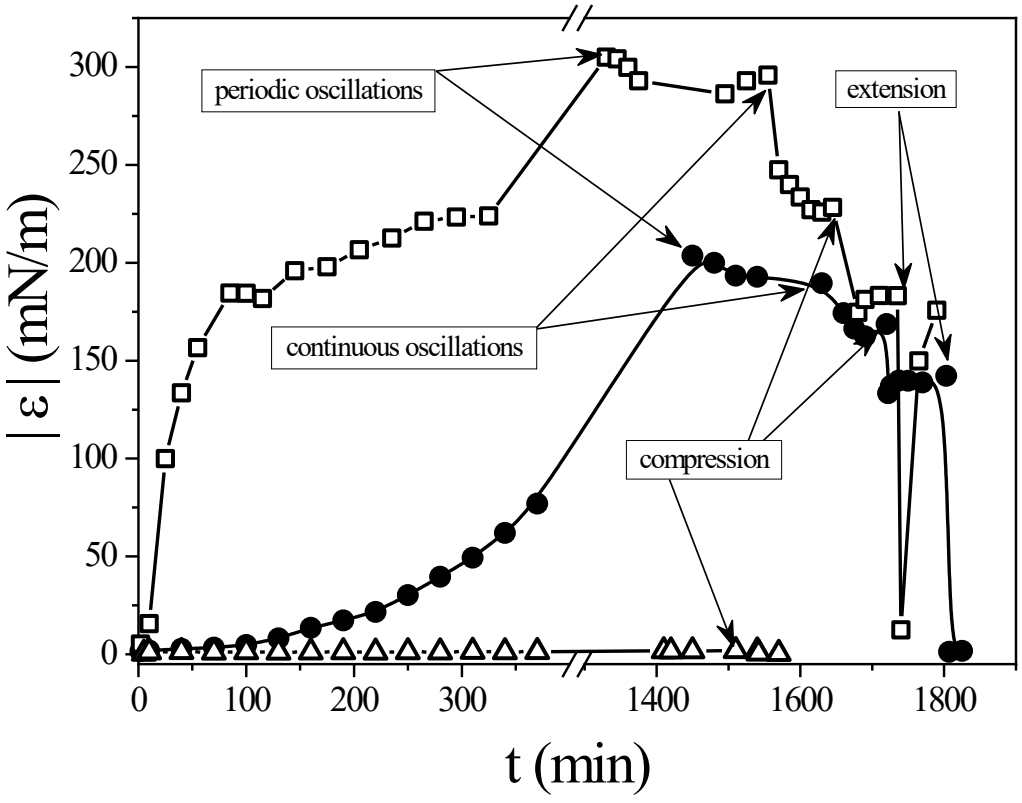

Figure 45. Kinetic dependences of the dynamic surface elasticity of $C_{60}(OH)_{20}$ solutions at a frequency of 0.1 Hz, vibration amplitude of 2.5% and concentrations: 0.5 (squares), 0.1 (circles), 0.03 g/l (triangles). Thin arrows indicate the inclusion of periodic oscillations in surface area, continuous oscillations in surface area, and sudden compression and extension of the surface, respectively.

The dynamic surface elasticity of a solution with a concentration of 0.03 g/l is zero within the error (figure 45). At a concentration of 0.1 g/L, a relatively long induction period was observed. The dynamic surface elasticity was close to zero for two hours and then increased slowly, reaching approximately 75 mN/m after 7 hours and 200 mN/m in the subsequent 17 hours, without fluctuations in surface area. Turning on the oscillations resulted in a small decrease, about 10 mN/m, in less than an hour. The transition to continuous oscillations resulted in a decrease of 20%, as in the case of subsequent surface compression. At a concentration of 0.5 g/L approaches 305 mN/m 22 hours after surface formation.

The dynamic surface elasticity of the studied $C_{60}(OH)_{20}$ solutions reaches stationary values approximately 24 hours after the formation of the surface, in contrast to the $C_{60}(OH)_{30}$ solutions, when the surface properties changed within several days after the formation of a new surface. The surface properties of $C_{60}(OH)_{20}$ solutions change for more than a day only as a result of external mechanical effects on the adsorption layer.

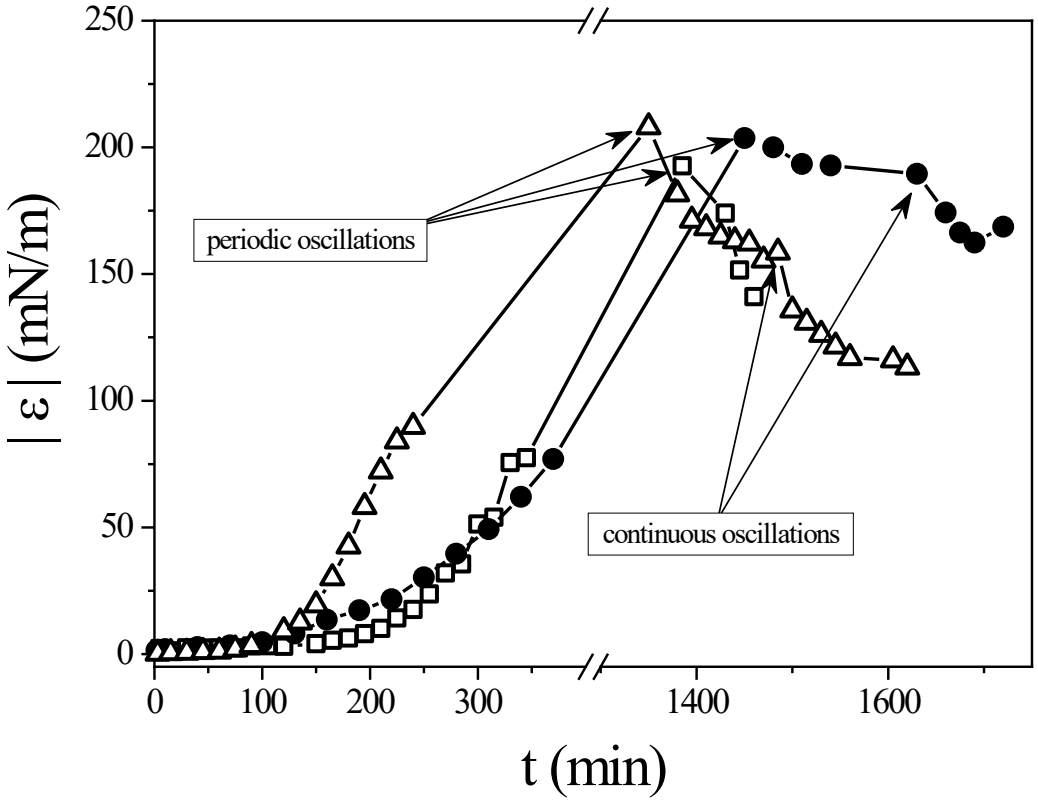

Figure 46. Kinetic dependences of the dynamic surface elasticity of $C_{60}(OH)_{20}$ solutions at a concentration of 0.1 g/l, a frequency of 0.1 Hz and relative amplitudes of surface area

fluctuations: 2.5% (circles), 5% (squares) and 7. 5% (triangles). Thin arrows indicate the inclusion of periodic and continuous fluctuations in surface area.

The induction period decreases and the dynamic surface elasticity changes faster as the vibration amplitude increases from 2.5. up to 7.5% (figure 46). The observed differences are presumably due to increased convection in the solution under the influence of surface vibrations with a larger amplitude. The inclusion of oscillations after a period of rest leads to a faster and stronger drop in surface elasticity at higher oscillation amplitudes due to stronger destruction of the fragile adsorption layer.

The ellipsometric angle Δ, approximately proportional to the surface concentration, approaches stationary values faster than surface tension and dynamic surface elasticity for both $C_{60}(OH)_{20}$ and $C_{60}(OH)_{30}$ solutions (figure 47). The main changes in the ellipsometric angle occur within about an hour after the formation of the surface and all changes after this are close to the error limits at a concentration of 0.5 g/l. The time to approach equilibrium increases with decreasing concentration.

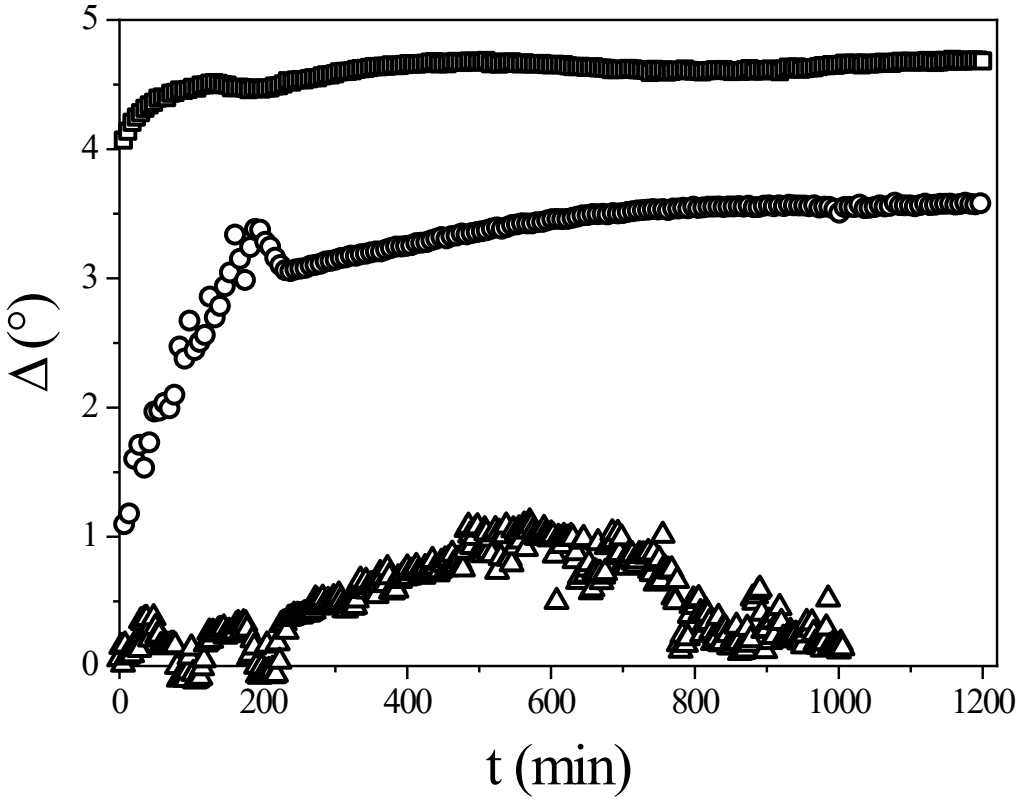

Figure 47. Kinetic dependences of the ellipsometric angle Δ at different concentrations of $C_{60}(OH)_{20}$ solution: 0.5 (red circles), 0.1 (black squares) and 0.03 g/l (green triangles).

The observed differences between the rates of relative changes in the ellipsometric angle and dynamic surface elasticity mean that minor changes in surface concentration when approaching equilibrium can lead to significant structural changes in the adsorption layer and thereby to noticeable changes in the rheological surface properties. The Δ values on the kinetic dependence (figure 47) are higher than the corresponding results for solutions of $C_{60}(OH)_{30}$, which indicates a higher surface concentration of the more hydrophobic fullerenol. At a concentration of 0.03 g/l Δ is close to zero and only some fluctuations in this angle are observed.

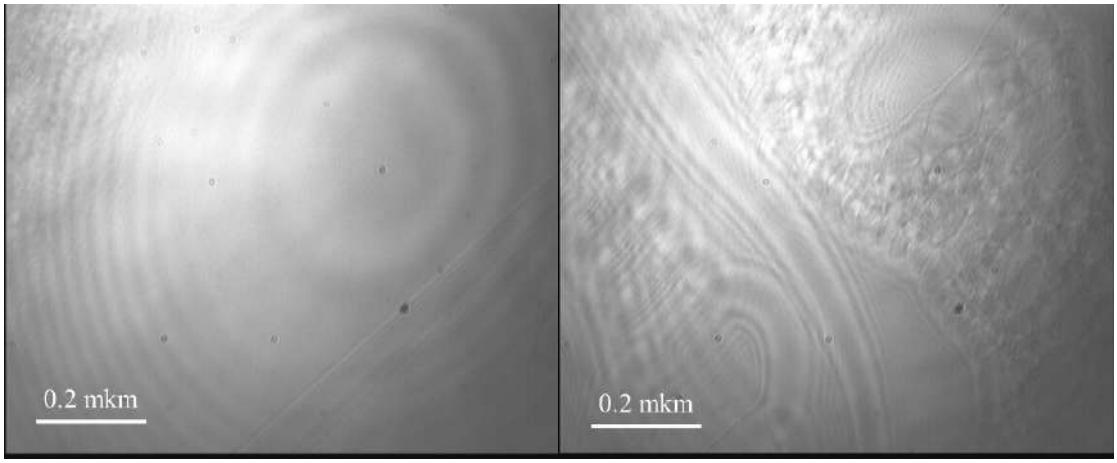

a) b)

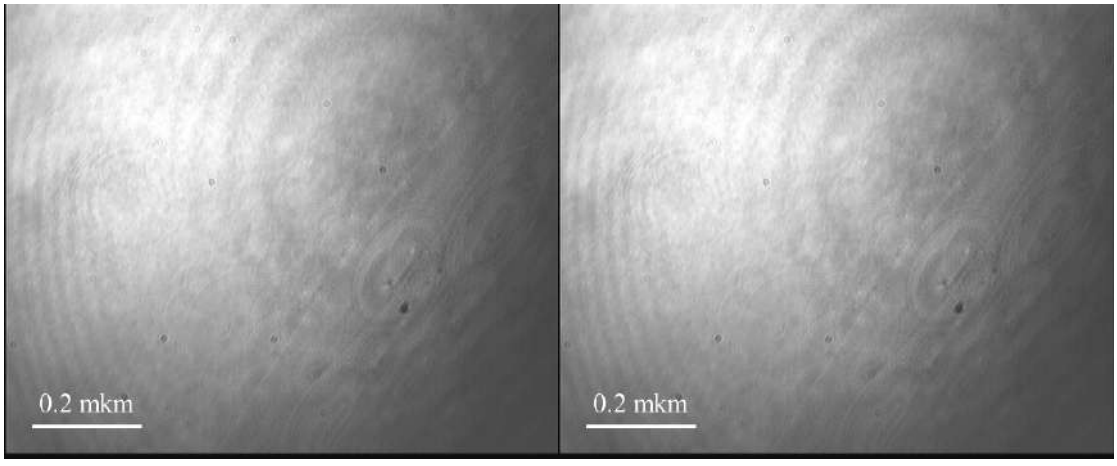

c) d)

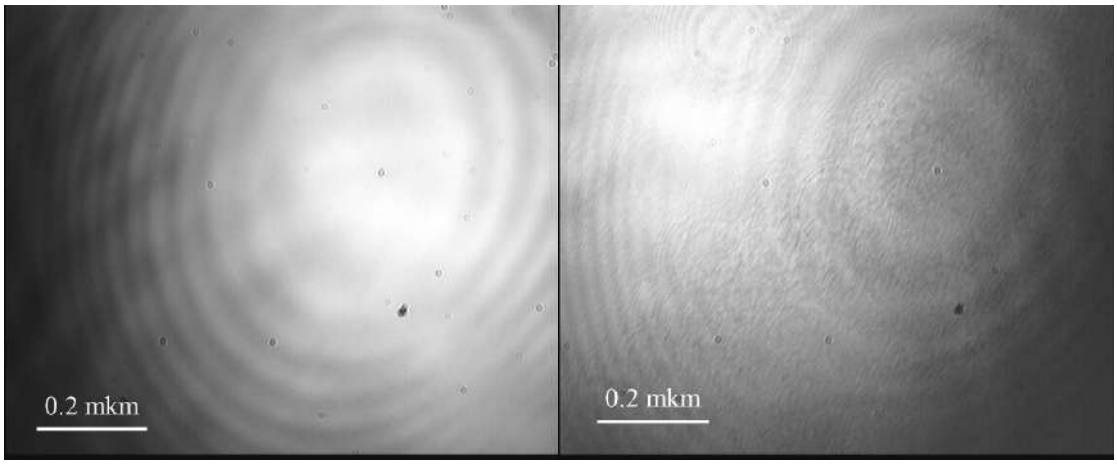

e) f)

Figure 48. Images obtained using a microscope at Brewster angle for the $C_{60}(OH)_{20}$ adsorption film after: a) 1 min; b) 15 min; c) 2.5 hours and d) 10 hours after surface formation. Image e) was obtained when the surface was compressed by 50% and f) when the surface was subsequently expanded to the original area. Solution concentration 0.03 g/l.

However, time averaging leads to nonzero values, indicating the formation of an adsorption layer. The observed fluctuations may be associated with the macroscopic heterogeneity of the adsorption layer and its mobility at low surface concentrations.

The heterogeneity of the adsorption layer of $C_{60}(OH)_{20}$ at a concentration of 0.03 g/l was also observed using Brewster angle microscopy, while at higher concentrations a macroscopically homogeneous adsorption layer was formed a few minutes after the formation of the surface, and its morphology did not change (figure 48). The formation of surface aggregates can be observed within a minute after the formation of the surface (right corner of the image (figure 48a)). In 15 minutes, almost the entire field is covered with units in constant motion (figure 48b). In this case, the surface pressure and surface elasticity are close to zero (figure 43, figure 45), but the ellipsometric angle Δ differs from the value for water (figure 47). Areas of the surface free from surface aggregates gradually decrease and practically disappear two and a half hours after the formation of the surface (figure 48c), but the adsorption layer retains its mobility. After ten hours the surface becomes macroscopically homogeneous (figure 48d). This adsorption stage corresponds to constant surface elasticity values, but small changes in the ellipsometric angle (figure 47). The morphology of the layer remains virtually unchanged when the surface is compressed by 50% (figure 48e). In this case, the surface mobility decreases, but the surface properties do not change. Immediately after stretching the

surface to the initial area, both areas covered with a fullerenol layer (lower right corner (figure 48f)), and areas free from the adsorption layer (upper left corner (figure 48f)), are visible, but after 10-15 minutes the layer becomes more homogeneous.

Fullerenol $C_{60}(OH)_{20}$ forms a macroscopically homogeneous layer at the solution-air interface, similar to the more hydrophilic fullerenol $C_{60}(OH)_{30}$. In both cases, small changes in surface tension (about 5 mN/m) are accompanied by a strong increase in the dynamic elasticity of the surface. At the same time, the surface elasticity is significantly higher for $C_{60}(OH)_{20}$ solutions and is about 300 mN/m versus 135 mN/m for $C_{60}(OH)_{30}$ solutions at a concentration of 0.5 g/l. A rigid adsorption layer is easily transferred to a solid surface using the Langmuir-Blodgett and Langmuir-Schaeffer methods. Adsorption kinetics are faster for $C_{60}(OH)_{20}$ solutions, probably due to the lower molecular charge and therefore lower adsorption barrier. The surface properties of fullerenol solutions are very sensitive to small mechanical disturbances at the interface. The $C_{60}(OH)_20$ adsorption layer is more fragile than the $C_{60}(OH)_{30}$ layer, and surface compression causes the dynamic surface elasticity to drop by about 25% in the first case, while in the second case the surface elasticity increases after compression. Continuous fluctuations in surface area also led to a decrease in surface elasticity as a result of partial destruction of the adsorption layer. Atomic force microscopy makes it possible to trace the destruction of the adsorption layer under mechanical influences and shows that this layer is not a monolayer of fullerenol molecules. It is also heterogeneous on a microscopic scale and contains small surface aggregates. Brewster angle microscopy shows that at low concentrations of $C_{60}(OH)_{20}$ the adsorption layer contains individual macroscopic surface aggregates at the beginning of adsorption, but becomes more homogeneous several hours after surface formation.

3.3 Surface properties of carboxyfullerene $C_{60}(C(COOH)_2)_3$ solutions

The surface activity of carboxyfullerene is significantly higher than that of fullerenols [195]. While the surface pressure of aqueous solutions of fullerenols does not exceed 7 mN/m and weakly depends on the number of hydroxyl groups in the molecule, for solutions of carboxyfullerenes in the same concentration range this value reaches approximately 30 mN/m.

(figure 49). Unlike fullerenol, carboxyfullerene behaves like a regular surfactant with moderate surface activity.

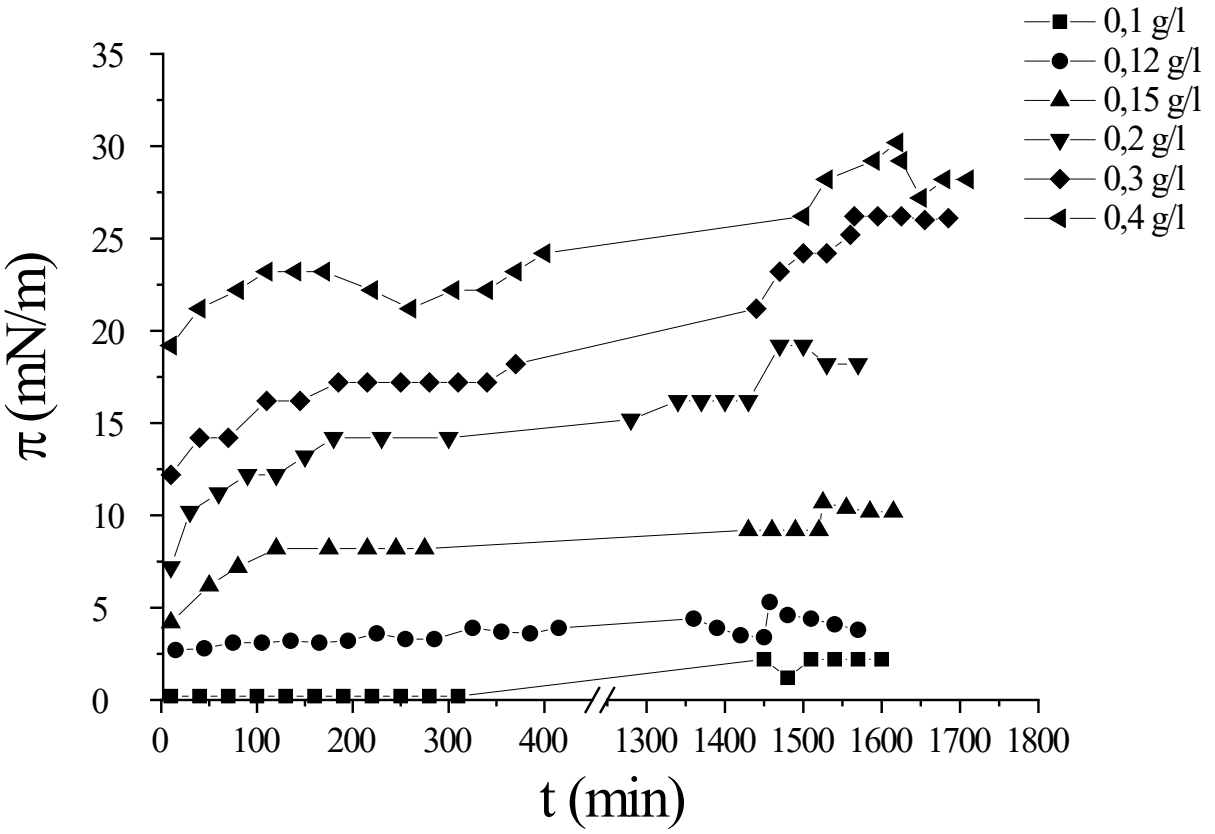

Figure 49. Kinetic dependences of surface pressure at various concentrations of solutions of carboxyfullerene $C_{60}(C(COOH)_2)_3$.

The rate of adsorption of carboxyfullerene is determined by its concentration. A slight increase in surface pressure at a concentration of 0.1 g/l occurs only 24 hours after the formation of the surface, while the main changes in surface pressure at concentrations above approximately 0.3 g/l occur within 1-2 minutes after the formation of a new surface, i.e. e. occur at surface lifetimes that are inaccessible to the method used (figure 49). After this time, only slow and weak changes in surface pressure can be observed. The increase in surface pressure of fullerenol solutions occurs more slowly at the beginning of adsorption due to the electrostatic adsorption barrier and faster over a longer period of time. The results obtained may indicate that the kinetics of carboxyfullerene adsorption is controlled by diffusion, at least at the first stage of adsorption. An induction period has never been observed for solutions of carboxyfullerenes.

In contrast to surface pressure, surface elasticity increases significantly longer even at the highest concentration tested (figure 50).

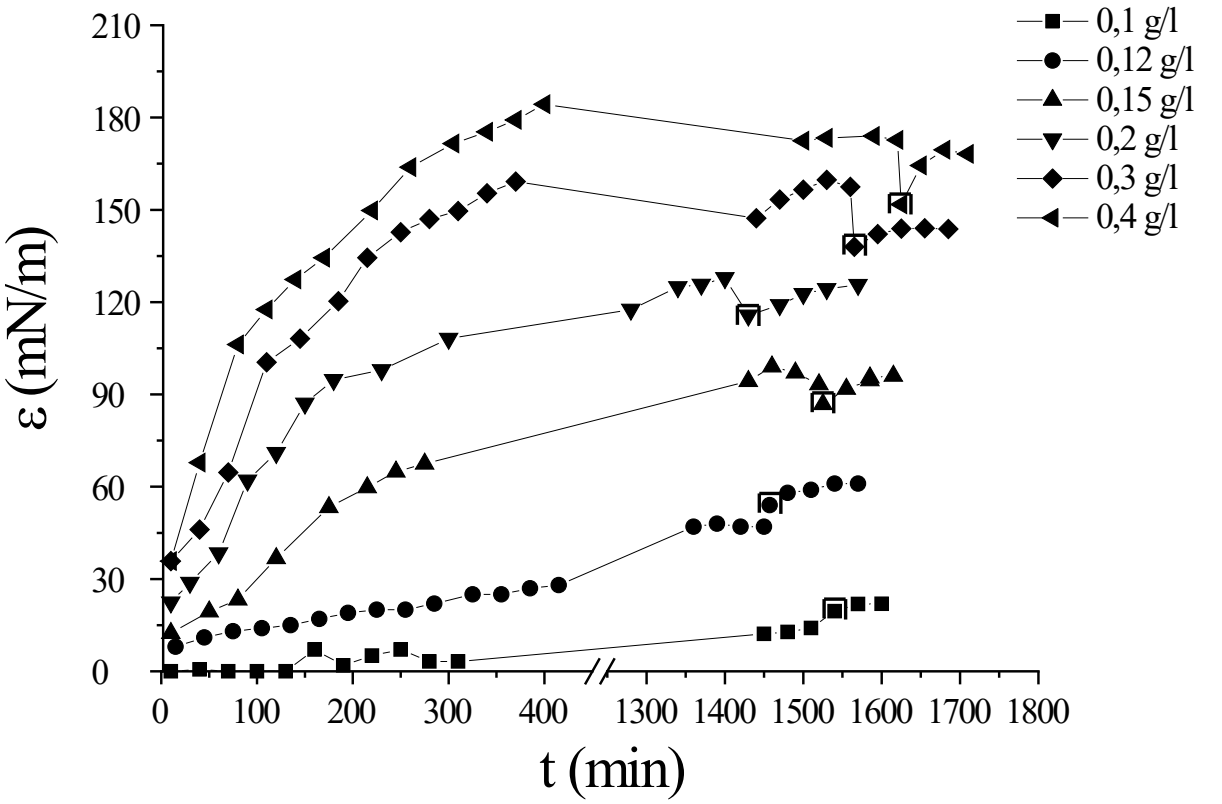

Figure 50. Kinetic dependences of dynamic surface elasticity at different concentrations of solutions of carboxyfullerene $C_{60}(C(COOH)_2)_3$. The marked points with surface lifetimes of more than 1400 minutes correspond to a sharp compression of the surface by 25%.

The surface elasticity reaches approximately 18 mN/m even at a concentration of 0.1 g/L and increases to approximately 180 mN/m at higher concentrations. The latter value exceeds the results for solutions of fullerenol with 30 hydroxyl groups, but is significantly lower than for solutions of fullerenol with 20 hydroxyl groups. These differences may be due mainly to variations in the surface density of fullerene derivatives. The packing of carboxyfullerene molecules in the surface layer is presumably intermediate between the packing of the two studied fullerenols with different numbers of hydrophilic groups. The surface elasticity (180 mN/m) is higher than typical values for adsorption layers of soft nanoparticles, but less than for layers of hard silica nanoparticles, where this value can reach 300 mN/m. The lower values for the adsorption layers of carboxyfullerene can presumably be

associated not with the lower rigidity of individual particles, but with the peculiarities of the packing of nanoparticles in surface aggregates. The rapid increase in surface pressure at the beginning of adsorption is accompanied by only moderate changes in surface elasticity, and this value changes more strongly as the surface concentration approaches its equilibrium value. This is possible if the approach to equilibrium is accompanied by significant changes in the layer structure with minor changes in the adsorption value.

The response of adsorption films of carboxyfullerene to mechanical stress also differs from the reaction of fullerenol films. In contrast to the latter case and layers of some hard nanoparticles, small-amplitude vibrations did not have a noticeable effect on the measured surface properties. Even sharp compression of the surface of carboxyfullerene solutions led to only small changes in the dynamic elasticity of the surface at relatively high concentrations (≥ 0.2 g/L, Figure 50). he corresponding changes at lower concentrations and changes in surface pressure did not significantly exceed the error limits, in contrast to the response to the tensile properties of adsorption films of fullerenols, which were destroyed by external mechanical influences. However, the surface elasticity of carboxyfullerene solutions decreased slightly upon compression of the surface at concentrations above 0.2 g/l, which indicates partial destruction of the layer structure, presumably due to the formation of cracks in the layer, as in the case of adsorption films of fullerenols.

Ellipsometric data support the assumption that changes in dynamic surface elasticity are mainly the result of structural changes in the adsorption layer, rather than a significant increase in the amount of adsorbed substance. The ellipsometric angle Δ, directly related to the surface concentration, remains almost unchanged already about an hour after the formation of the surface at a concentration of 0.3 g/L, when noticeable changes in the dynamic surface elasticity can be observed (figure 51).

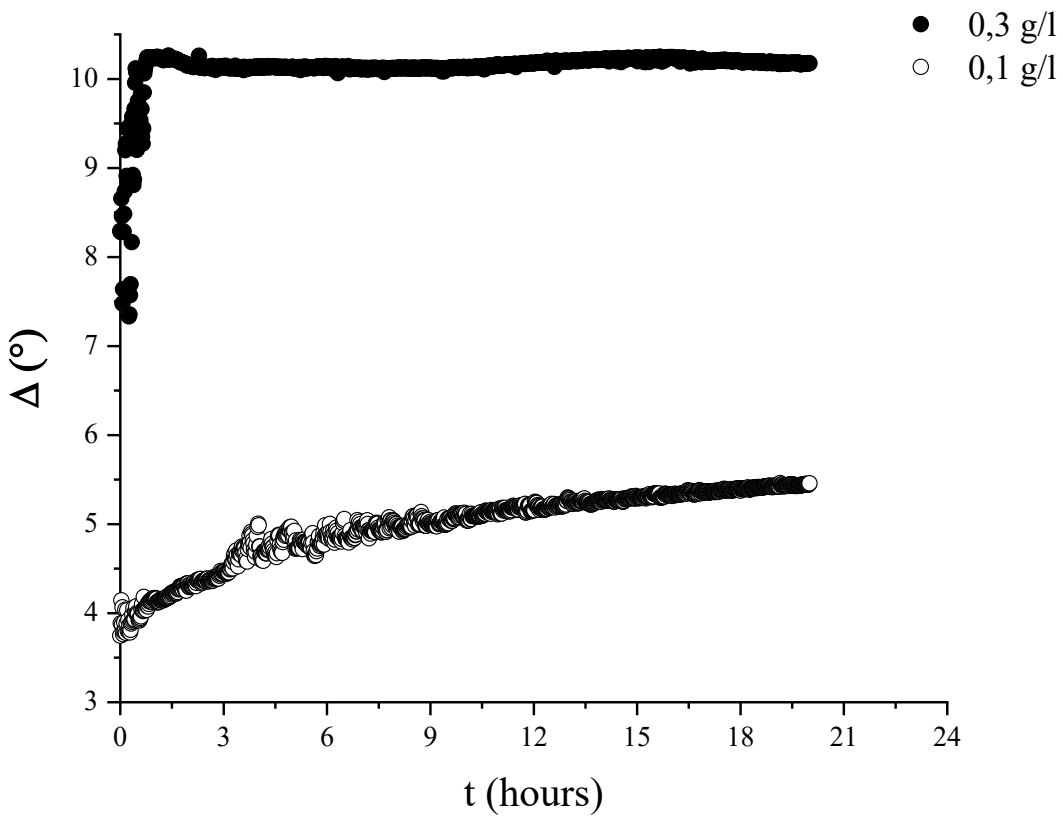

Figure 51. Kinetic dependence of the ellipsometric angle Δ for a solution of carboxyfullerene $C_{60}(C(COOH)_2)_3$ at concentrations of 0.3 g/l and 0.1. g/l.

This means that minor changes in surface concentration after initial growth can be accompanied by a noticeable increase in dynamic surface elasticity as a result of restructuring of the surface layer structure. At a concentration of 0.1 g/l there is a noticeable increase in the ellipsometric angle, and the surface pressure and dynamic surface elasticity are close to zero within the error (figure 49, figure 50). In this case, the adsorption layer is presumably heterogeneous and contains islands of a relatively dense surface phase of carboxyfullerene. The adsorption process leads to an increase in surface concentration, but the surface pressure begins to deviate from zero only when an increase in the size and/or number of islands leads to interaction between them. Fluctuations of the ellipsometric signal at the first stage of adsorption confirm the assumption of the formation of a non-uniform surface (figure 51). he chaotic movement of sections of the adsorption layer of different surface densities in the spot of the laser beam on the surface of the liquid due to the fluidity of the layer can lead to chaotic changes in the signal, which disappear quite abruptly when the adsorption layer becomes stationary.

Although the sensitivity of microscopy at the Brewster angle may be insufficient and does not allow observing the heterogeneity of the adsorption layer, it confirms the liquid-like nature of the carboxyfullerene film. The layer is macroscopically homogeneous for more than a day after surface formation (figure 52). Unlike fullerenol films, a slight mechanical disturbance of a carboxyfullerene film with a thin needle does not lead to a noticeable change in the surface morphology due to the rapid restoration of the original macroscopic structure.

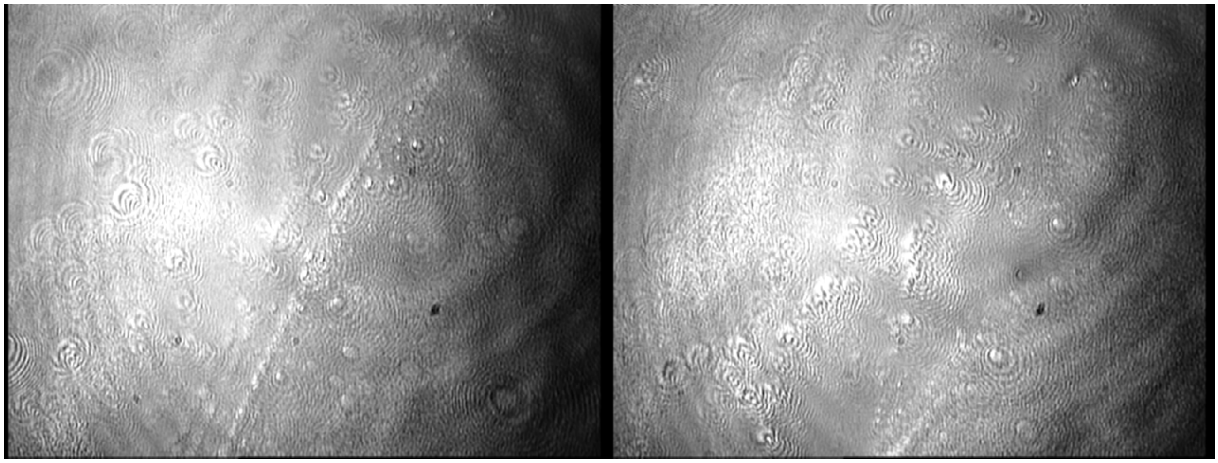

а) б)

Figure 52. Images obtained using a microscope at Brewster angle of a film of carboxyfullerene $C_{60}(C(COOH)_2)_3$ with a solution concentration of 0.3 g/l: a – 5 minutes after surface formation; b) after disturbing the surface with a thin rod.

The microscopic morphology of adsorption films of carboxyfullerene can be assessed by atomic force microscopy after transferring the layer to the surface of a freshly cleaved mica plate. If, approximately 10 minutes after the formation of the surface, the film is transferred at a solution concentration of 0.4 g/l, then an almost continuous film with individual aggregates embedded in it can be observed on the mica surface (figure 53a). The diameter of the aggregates is 20–30 nm, and their height is 2–3 nm, indicating that they are not monolayers, but bi- and trilayers (the diameter of a single carboxyfullerene molecule is approximately 1.3 nm [155]. This morphology of surface aggregates is presumably the result of the transformation of primary micelles formed in the bulk of the liquid. Such micelles (aggregates 40-80 nm in size) were observed in aqueous solutions of water-soluble derivatives of malonic acid C_{60} [196].

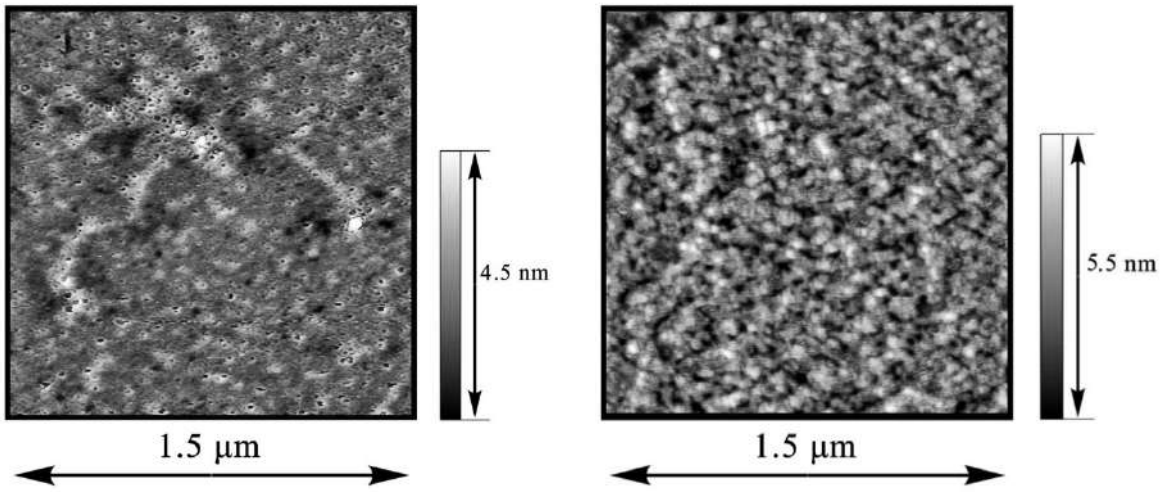

а) б)

Figure 53. AFM images of various samples of the $C_{60}(C(COOH)_2)_3$ carboxyfullerene film: (a) 10 and (b) 470 min after surface formation.

The morphology of the layer changes significantly when it is transferred to the mica surface 470 min after surface formation. In this case, larger aggregates with a diameter of up to 50 nm and a height of up to 4 nm appear. Thus, these objects become closer to the micellar aggregates observed in water. The surface concentration of the aggregates increases and they come into contact at longer adsorption times. These changes in surface morphology are accompanied by a marked increase in dynamic surface elasticity with small increases in surface pressure and total surface concentration and are presumably associated with the growth of surface aggregates during adsorption.

Compression of the adsorption film of carboxyfullerene does not lead to its complete dissolution. The compression isotherm after adsorption from a solution with a concentration of 0.3 g/l for 17 hours consists of two sections with different slopes (figure 54). The second and third compressions after corresponding stretching of the film lead to different isotherms, which are characterized by a large slope and small hysteresis.

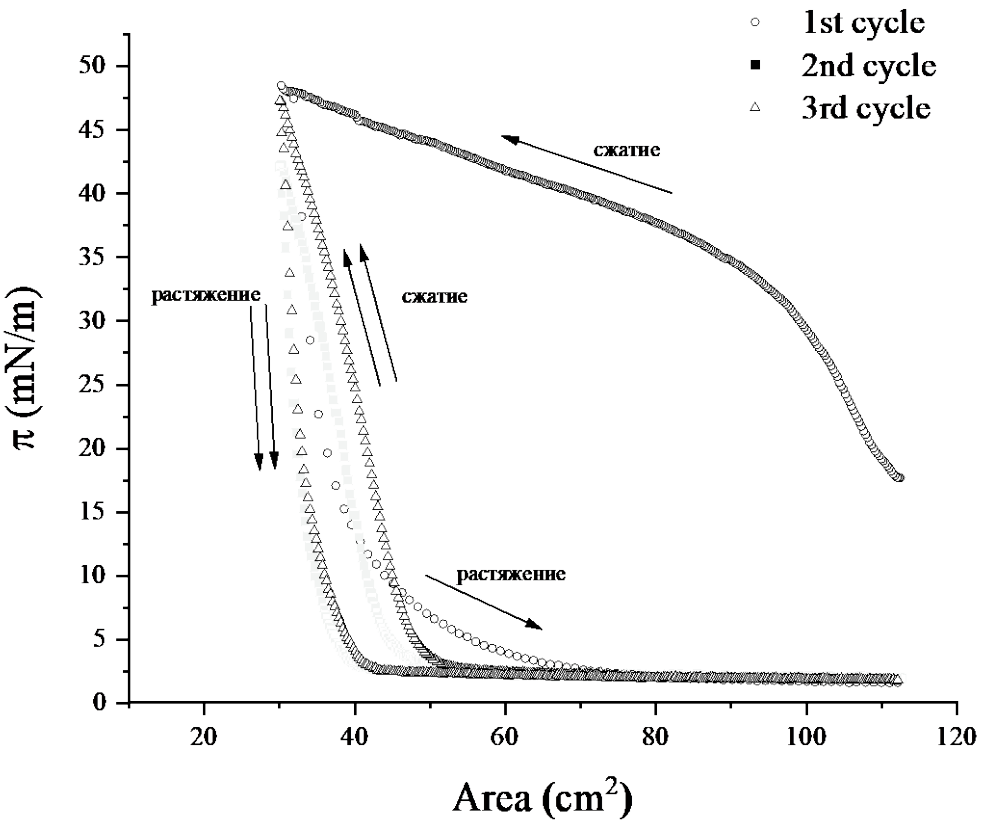

Figure 54. Surface pressure isotherms of adsorption films of carboxyfullerene $C_{60}(C(COOH)_2)_3$.

The slope of the first part of the first compression isotherm is close to the slopes of the second and third compression isotherms, and this part of the isotherm corresponds presumably to compression of the film without its noticeable dissolution. The second part of the first isotherm with a slight slope can be associated with the partial dissolution of the carboxyfullerene film. The coincidence of the second and third compression isotherms indicates that dissolution has stopped, and in the surface layer there are presumably only stable aggregates that do not dissolve further after the first compression.

Carboxyfullerene can also be applied to the aqueous subphase from a concentrated solution in water or from a solution in ethanol. In this case, the dissolution of carboxyfullerene in the bulk phase is apparently limited by a significant desorption barrier. The formation of stable surface aggregates of carboxyfullerene can lead to an increase in the barrier.

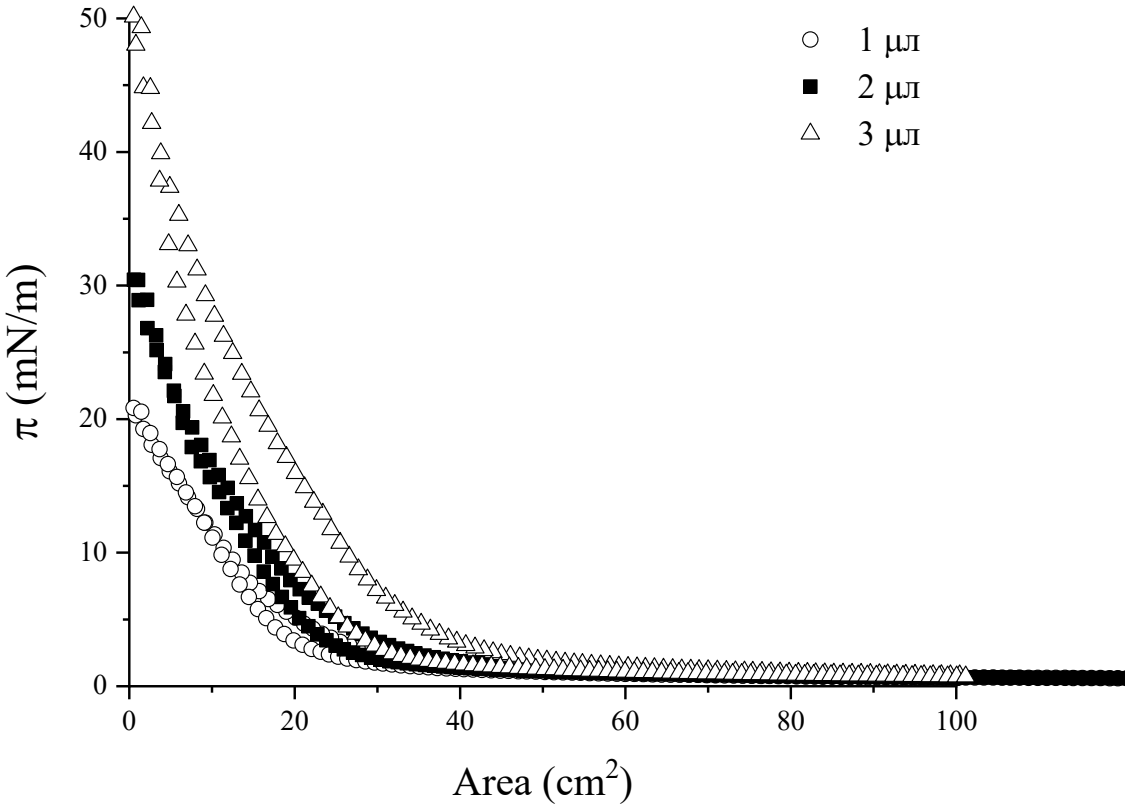

Figure 55. Surface pressure isotherms of deposited films of carboxyfullerene $C_{60}(C(COOH)_2)_3$ at different volumes of solution application with a solution concentration of 2 g/l.

The initial increase in surface pressure upon compression of the surface corresponds to calculated surface concentrations of 300 – 400 molecules per nm2, depending on the volume of application. Such high concentrations mean that film application is accompanied by the dissolution of carboxyfullerene in the subphase and only part of it remains on the surface. The corresponding compression isotherms with a large slope are similar to the isotherms of the second and third compression of the adsorption film, which in this case presumably contains only stable surface aggregates (figure 55).

A concentrated solution that is applied to an aqueous surface appears to contain aggregates, and these are more likely to remain at the interface than individual molecules, but the formation of aggregates directly in the surface layer is also possible. The main difference between the compression isotherms for deposited and adsorbed films is the different initial surface pressures (figure 54, figure 55). If for the deposited film this value is close to zero, then the increase in surface pressure for the adsorbed film begins from approximately 2 mN/m for

the second and third compression/extension cycles. As a result, there are small differences in isotherm slopes at higher surface pressures.

The use of AFM shows that compression of the deposited film is accompanied by the growth of surface aggregates and an increase in their surface concentration (figure 56).

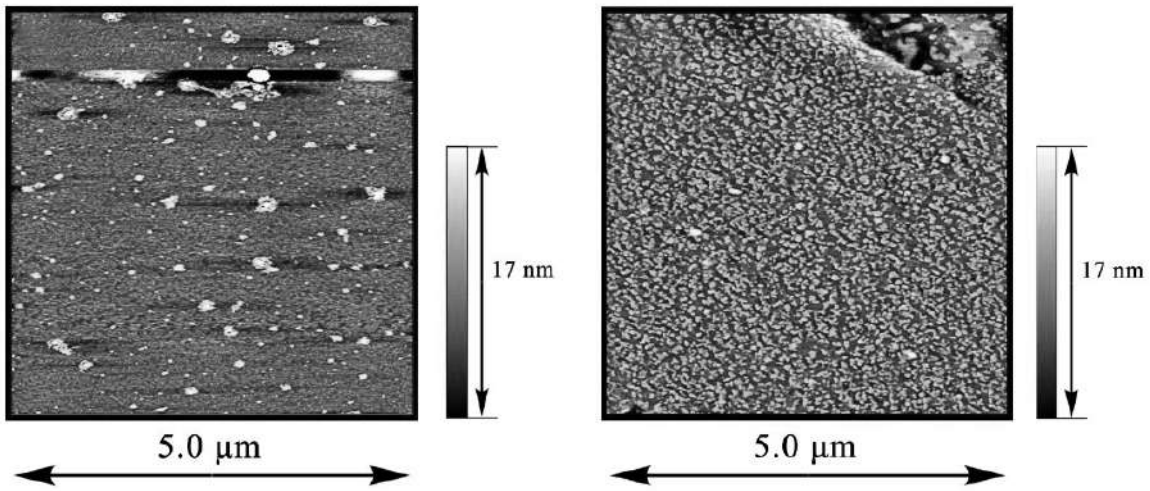

а) б)

Figure 56. AFM images of a film of carboxyfullerene $C_{60}(C(COOH)_2)_3$ deposited from a solution in ethyl alcohol with a concentration of 0.06 g/l. Application volume - 3 ml, surface pressure 15 mN/m (a) and 27 mN/m (b).

The size and morphology of surface aggregates of carboxyfullerene in the deposited and adsorbed film are similar (figure 53b, figure 56b). At the same time, these aggregates are significantly smaller than in deposited C_{60} fullerene films, reaching up to 100 nm in the Z-direction. This difference appears to be caused by the very high hydrophobicity of C_{60}, which results in its extremely low solubility in watere.

The surface activity of carboxyfullerene $C_{60}(C(COOH)_2)_3$ is close to conventional surfactants and significantly exceeds the surface activity of fullerenols. Adsorption of carboxyfullerene occurs much faster than fullerenols, and the kinetic dependences of surface properties in the first case do not have an induction period. The dynamic surface elasticity of carboxyfullerene solutions changes significantly over several hours, when the surface tension, after an initial rapid decrease, changes only slowly. This stage of adsorption layer formation is presumably associated with structural changes in the surface layer with minor changes in the adsorbed amount due to the formation of surface aggregates. The adsorption layer of

carboxyfullerene is less fragile than the adsorption layers of fullerenol, and its properties change under external mechanical influences to a lesser extent than those of fullerenol layers. Brewster angle microscopy images of carboxyfullerene adsorption layers indicate their liquid-like nature. When a layer is deformed with a thin needle, the restoration of its morphology occurs very quickly and cannot be traced by the methods used. The AFM images show that the adsorption layer contains numerous surface aggregates, the size and number of which increase during the adsorption process. The first compression of the adsorbed layer leads to its partial dissolution. Compression isotherms are almost the same for the second and third cycles of compression/extension of the layer due to the high stability of the remaining surface aggregates in the adsorption layer.

Chapter 4 Properties of a C_{60} fullerene mixture films with amphiphilic polymers and of C_{60} microaggregates films on a water surface

4.1 Properties of mixed films of fullerene C_{60} with poly-n-isopropylacrylamide (PNIPAM) and polyvinylpyrrolidone (PVP)

For C_{60} films deposited on the surface of water from various volumes of toluene solution with a concentration of 0.5 mg/ml, the dependence of surface pressure on the area per fullerene A molecule is typical for systems without surface phase transitions (figure 57) [197].

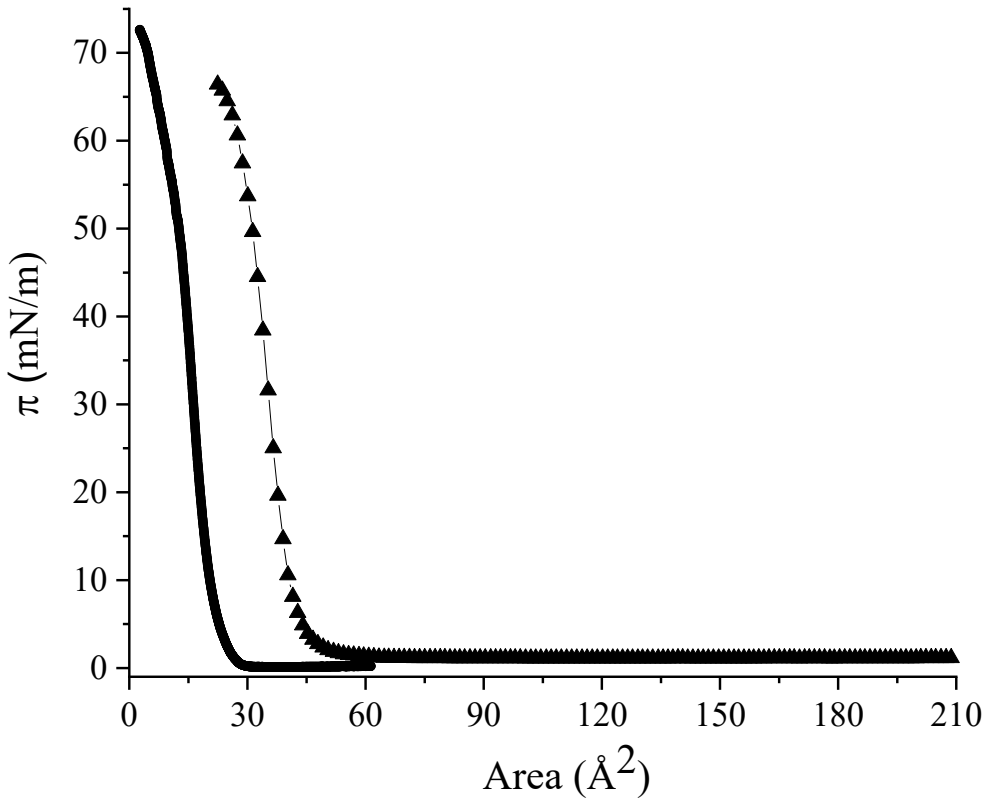

Figure 57. Surface pressure isotherms of a film of pure fullerene deposited from a solution in toluene with a concentration of 0.5 mg/ml with a deposition volume of 100 (squares) and 200 μl (triangles).

Surface pressure increases monotonically during compression without any features. The relationships are linear over limited surface pressure ranges, but the slope of the isotherms

gradually decreases as surface pressure increases. For a C_{60} film with a deposition volume of 100 μL, the linear region corresponds to a surface pressure of approximately 10 to 45 mN/m, and its extrapolation to zero surface pressure gives an area per molecule of 0.22 nm^2. This value is much smaller than 0.87 nm^2 for a densely packed C_{60} monolayer [198], ті.е. fullerene does not form a monolayer on the surface. Compressed fullerene multilayers are characterized by high cohesion and do not stretch after a sharp increase in the area between the barriers in a Langmuir cell, which leads to strong hysteresis of compression-tension isotherms.

The modulus of dynamic surface elasticity is also a smooth function of area per molecule or surface pressure, but with a maximum at surface pressures close to 25 mN/m (figure 58).

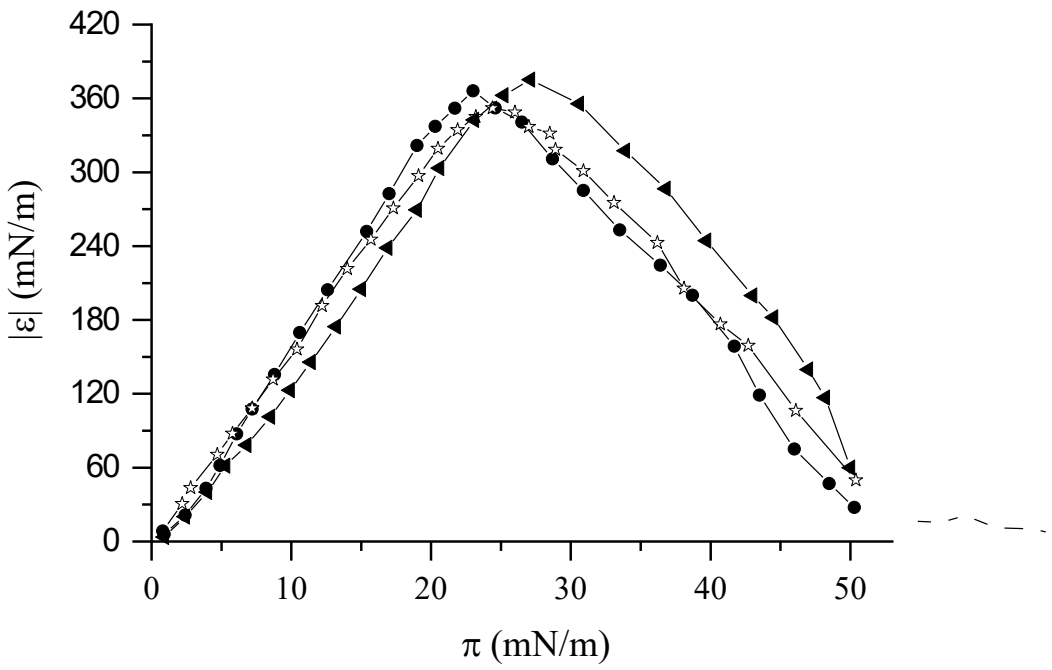

Figure 58. Dependence of the modulus of dynamic surface elasticity on surface pressure for deposited C_{60} films. Circles, triangles and stars correspond to different experiments.

The maximum surface elasticity (~370 mN/m) is significantly higher than typical values for deposited and adsorbed polymer films, but is close to the results for monolayers of solid nanoparticles [156,199]. It should be noted that the reproducibility of the surface elasticity isotherms of C_{60} films is somewhat worse than for other systems, which is apparently due to the insufficient reproducibility of the size and shape of fullerene aggregates in the surface layer. The nonmonotonic dependence of dynamic surface elasticity on surface pressure

is a typical feature of systems with structural restructuring in the surface layer [183,192,199,200]. For example, the maximum elasticity of monolayers of solid nanoparticles arises as a result of monolayer collapse [199,201,202] C_{60} film is not a monolayer; therefore, the mechanism of its restructuring with increasing surface pressure may differ from the corresponding mechanism for monolayers of both insoluble surfactants and solid nanoparticles. A sharp decrease in dynamic surface elasticity at high surface pressures indicates that the film structure becomes less resistant to mechanical disturbances in this region (figure 58).

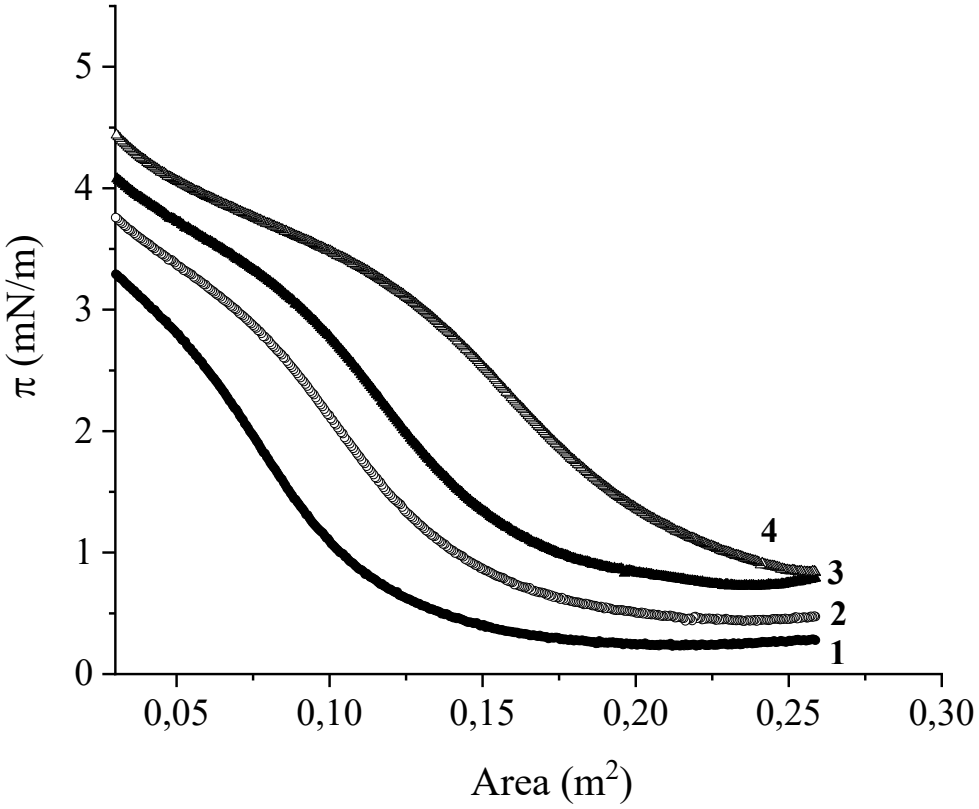

Figure 59. Surface pressure isotherms of PVP film with application volumes of 50 (1), 100 (2), 200 (3) and 300 (4) μl from a solution in ethanol with a concentration of 0.5 mg/ml.

The properties of PVP films deposited on the water surface are completely different. Compression of the film leads to a small but sharp increase in surface pressure to approximately 3 mN/m and a slightly weaker increase with further compression (figure 59). The corresponding nonmonotonic dependence of dynamic surface elasticity on surface pressure is characteristic of solutions of linear flexible polymers. The surface elastic modulus

reaches a local maximum of about 4.5 mN/m and approaches low values (~ 1 mN/m) at higher surface pressures (figure 60).

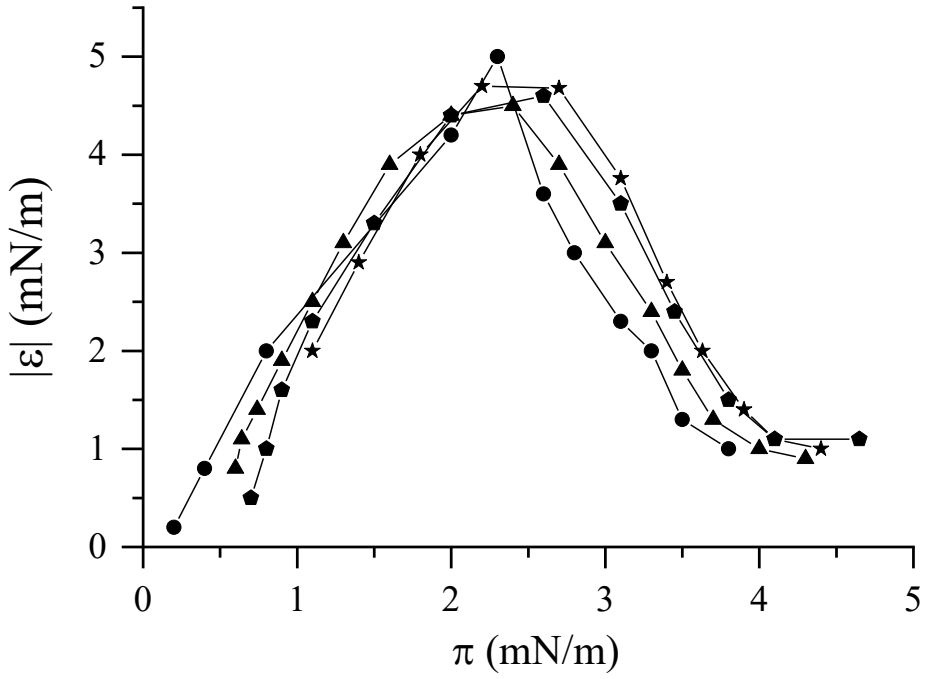

Figure 60. Dependence of the modulus of dynamic surface elasticity on surface pressure for deposited PVP films. Circles, triangles, pentagons and stars correspond to different experiments.

The maximum dynamic surface elasticity of polymer films arises as a result of the formation of loops and tails of macromolecules that form the far region of the surface layer [183,192,203–205]. At low surface pressures, the adsorbed macromolecules have a nearly planar conformation in the surface layer, and the surface elasticity increases with increasing surface concentration and surface pressure. Loops and tails gradually appear, surface stresses relax due to the exchange of segments between the far and near regions of the surface layer, and surface elasticity begins to decrease. Subsequent repeated compression of the film does not lead to noticeable changes in surface elasticity as a result of the sequential displacement of polymer segments from the near region of the surface layer. If PVP is adsorbed at the solution-air interface from solution, the dynamic surface elasticity as a function of surface age or surface pressure peaks at about 4.5 mN/m and drops to about 1 mN/m as equilibrium is approached. [204].

Qualitatively the same dependence of surface pressure on the area per molecule is observed for deposited PNIPAM films on the water surface (figure 61).

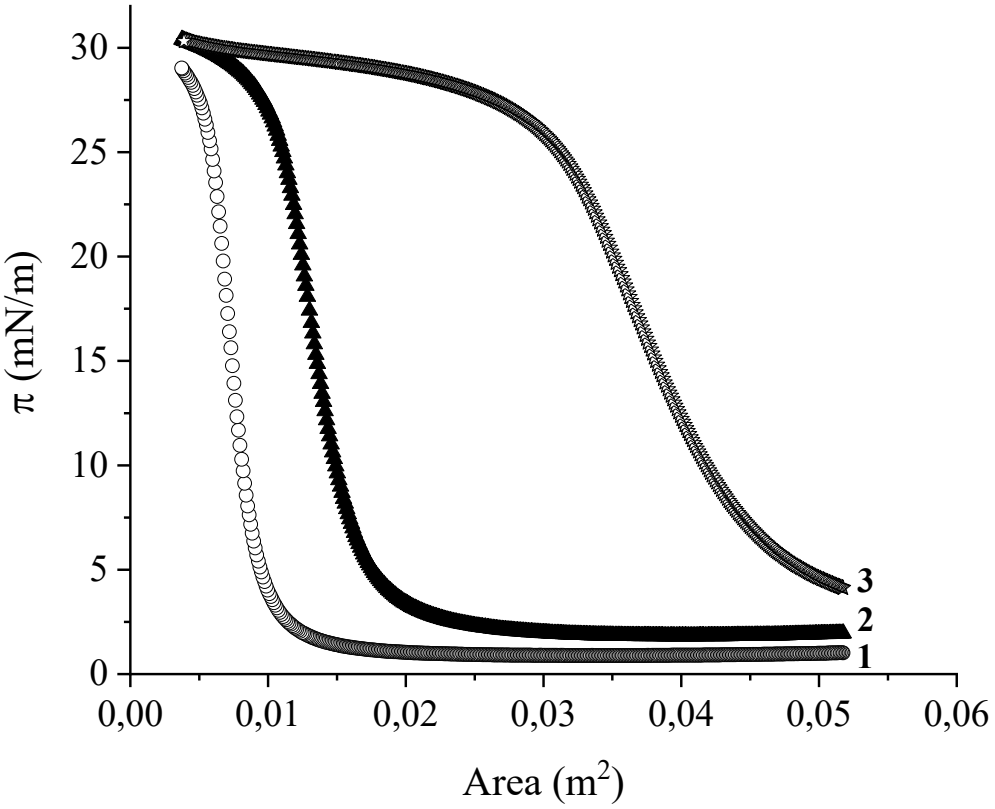

Figure 61. Surface pressure isotherms of deposited PNIPAM films with a deposition volume of 50 (1), 100 (2), 300 (3) μL of a solution in ethanol with a concentration of 0.5 mg/ml.

In this case, the surface pressure increases to significantly higher values, approximately 28 mN/m, and changes little with further compression. The dependence of the dynamic surface elasticity of PNIPAM films on surface pressure has a significantly higher peak (~ 55 mN/m) than that of PVP (figure 62). Dynamic surface elasticity at high surface pressures (> 30 mN/m) is in the range of 1 – 3 mN/m. A maximum (~ 55 mN/m) also appears in the kinetic dependences of the dynamic surface elasticity of PNIPAM solutions, after which this value approaches 2 – 3 mN/m at long surface lifetimes [192].

Note that the maximum value of the dynamic surface elasticity of films of amphiphilic polymers depends on the number of hydrophobic groups per polymer segment, which affects the segment-water and segment-segment interactions in the film.

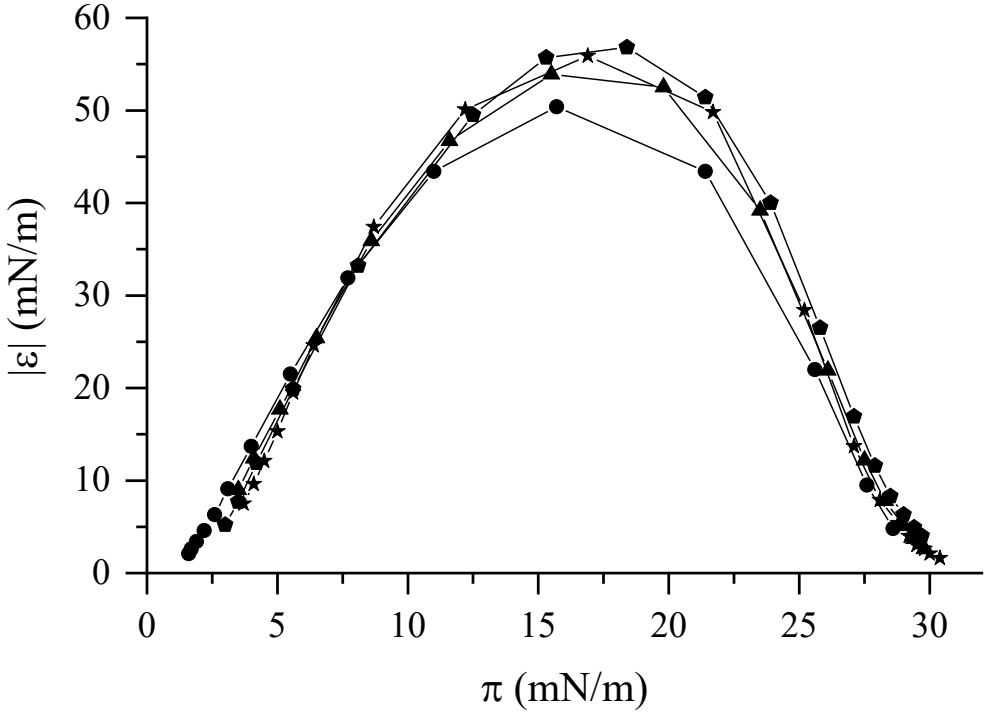

Figure 62. Dependence of the modulus of dynamic surface elasticity on surface pressure for deposited PNIPAM films. Circles, triangles, pentagons and stars correspond to different experiments.

Surface pressure isotherms of deposited mixed films of PVP and C_{60} fullerene have some features that are absent in the corresponding results for individual substances (figure 63). For mixed deposited PVP/C_{60} films, the surface pressure increases from zero to a characteristic value of 3 mN/m, after which it remains virtually unchanged, and then sharply increases to approximately 70 mN/m, as for layers of pure fullerene (figure 57). The extent of the surface pressure plateau region depends on the molar ratio of fullerene and polymer in the layer. The corresponding dependence of dilatational dynamic surface elasticity on surface pressure is close to the dependence for deposited fullerene films and has a local maximum of about 270 mN/m (Figure 64).

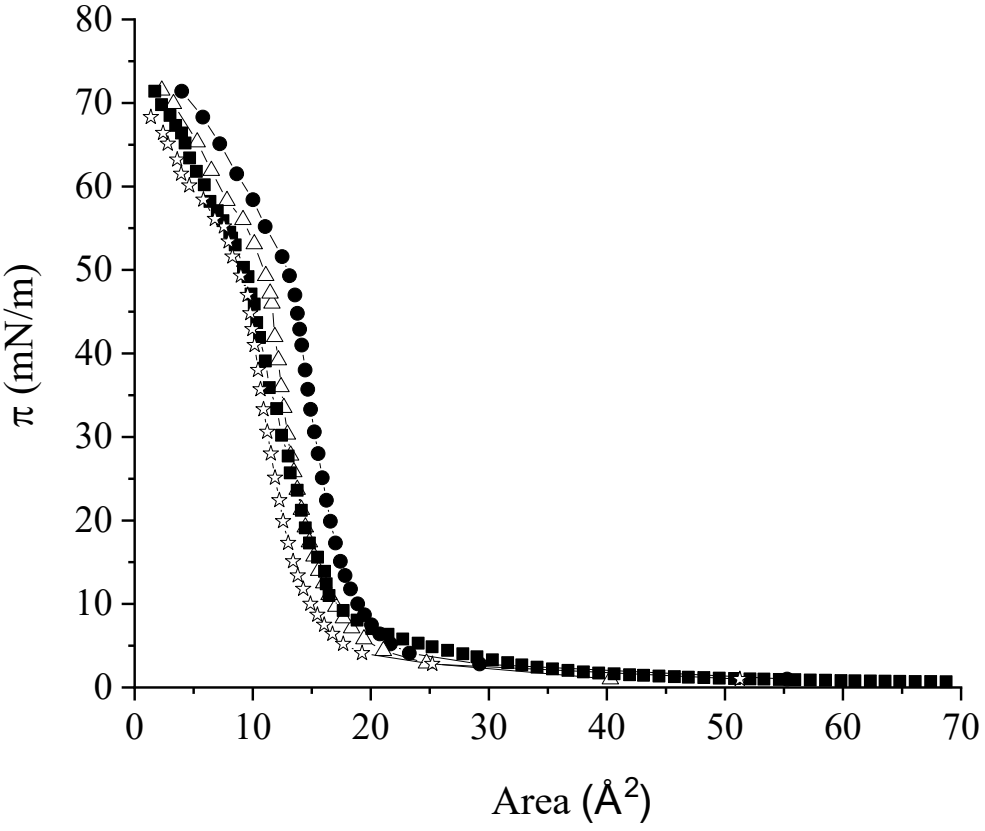

Figure 63. Dependences of surface pressure on the area per fullerene molecule for mixed deposited PVP/C60 films at polymer:fullerene molar ratios of 3.2 (circles), 2.4 (triangles), 1.6 (pentagons), 0. 8 (stars).

At the same time, there is a second small local maximum (less than 10 mN/m) at low surface pressures (< 3 mN/m). Therefore, the entire dependence consists of two parts, corresponding to two maxima of surface elasticity. The first part at surface pressures less than 4 mN/m is close to the corresponding dependence for deposited PVP films with a small local maximum (figure 62). The second part, beyond the local minimum at surface pressures of about 4 mN/m, practically coincides with the surface elasticity isotherm for C_{60} fullerene films (figure 58). Thus, the dependence in Figure 64 does not indicate the interaction of the two components in the deposited film, and the two parts of this dependence can be associated with the properties of PVP and C_{60} separately. The surface pressure isotherms (figure 63) can also be divided into two parts corresponding to PVP and C_{60}: the first increase in surface pressure followed by the pseudoplateau region (first part) and the strong increase after the pseudoplateau region (second part).

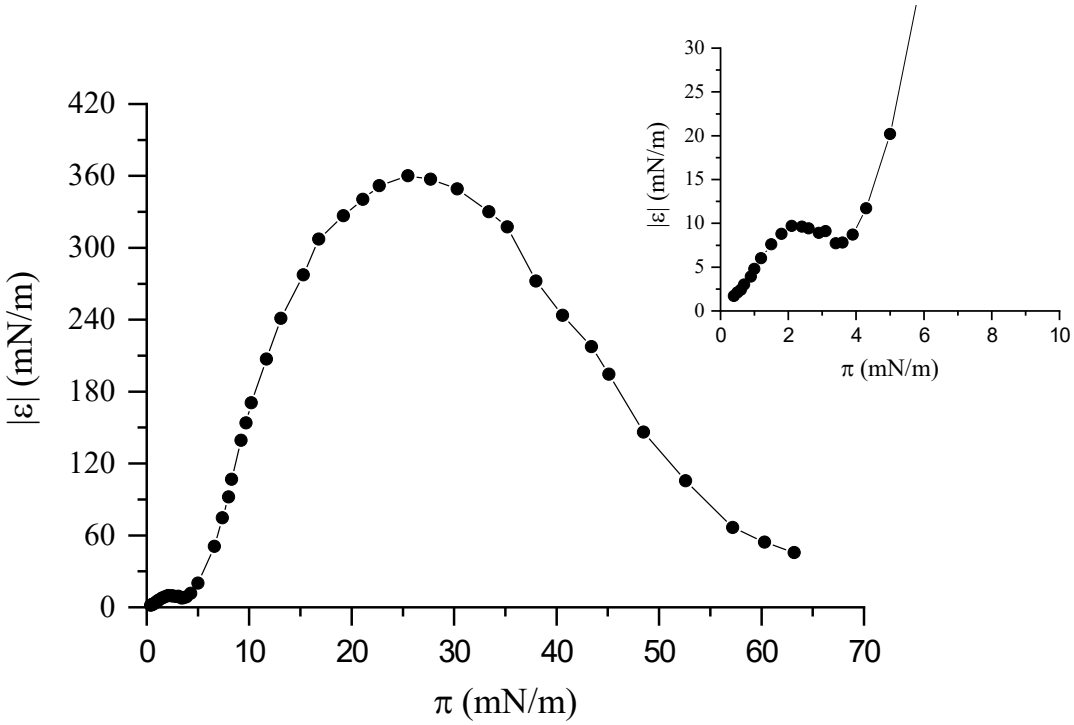

Figure 64. Dependence of surface elastic modulus on surface pressure for mixed layers of PVP/C_{60}. 100 ml of a solution of fullerene in toluene and 50 ml of a solution of PVP in ethanol with concentrations of 0.5 and 0.25 mg/l, respectively, were applied successively to the water surface.

The results for the mixed deposited PNIPAM/C_{60} films are close to those for the PVP/C_{60} films, but the higher surface pressure and elasticity of the PNIPAM films allow for a more detailed study. The surface pressure isotherm and the dependence of dynamic elasticity on surface pressure for PNIPAM/C_{60} films can also be divided into two parts. The initial increase in surface pressure, together with the subsequent pseudoplateau, constitutes the first part of the isotherm, and the sharp increase to high values constitutes its second part (figure 65). The main difference from the results for PVP/C_{60} films is the high pseudoplateau surface pressure (~ 28 mN/m), which coincides with the corresponding results for pure PNIPAM layers (figure 62).

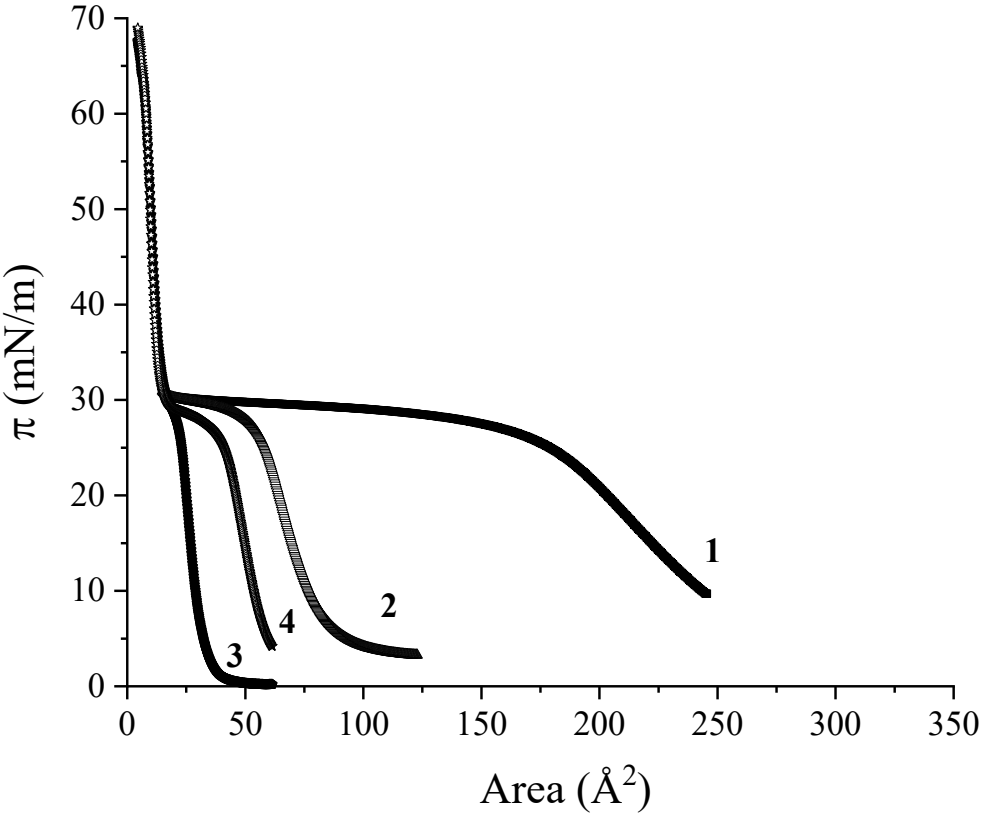

Figure 65. Dependences of surface pressure on the area per fullerene molecule for mixed deposited PNIPAM/C_{60} films with a polymer:fullerene molar ratio 12,8 (1), 6,4 (2), 1,6 (4), 0,8 (3).

The dependence of dynamic elasticity on surface pressure of deposited PNIPAM/C_{60} films consists of the same two regions corresponding to the first and second peaks, which are separated by a local minimum (figure 66). The first maximum value is less than the second, but unlike the PVP/C_{60} layers the difference is small. If the ratio of the molar concentrations of fullerene and PNIPAM is higher than approximately 3, then the first part of the isotherm practically coincides with the corresponding results for films of pure PNIPAM. The maximum value is approximately 55 mN/m, and the subsequent local minimum value is approximately 3 mN/m. After the minimum, dynamic elasticity increases sharply to a second maximum.

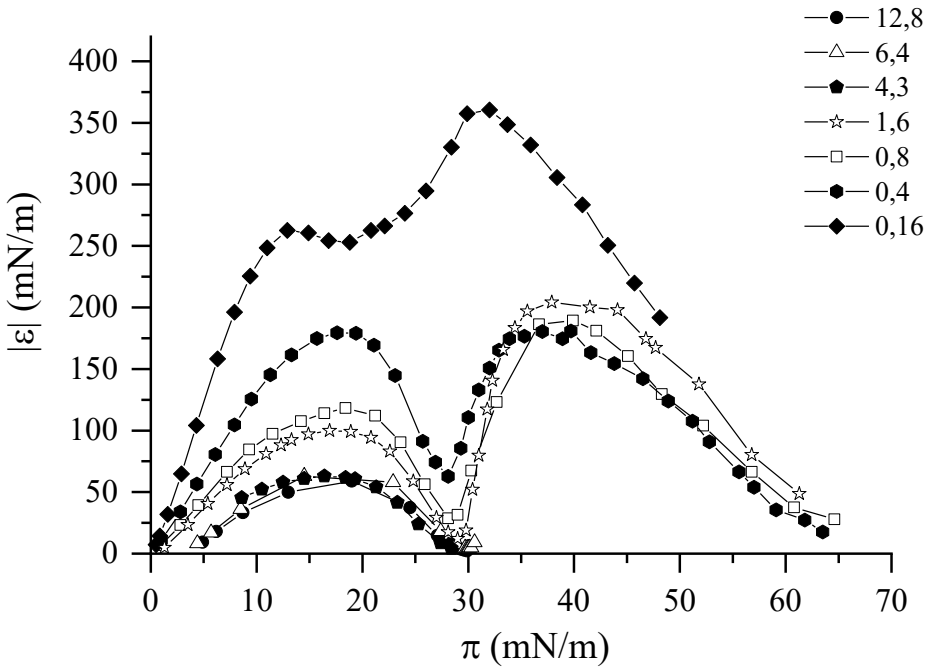

Figure 66. Dependence of the surface elastic modulus on surface pressure for mixed deposited PNIPAM/C_{60} films at polymer:fullerene molar ratios of 12.8 (circles), 6.4 (triangles), 4.3 (pentagons), 1.6 (lstars), 0.8 (squares), 0.4 (pentagons), 0.16 (diamonds).

This maximum value is less than for films of pure C_{60} (figure 58), and corresponds to a higher surface pressure than the elastic maximum for C_{60}. The results obtained show that fullerene has little effect on the first part of the dependence, which is determined mainly by the polymer. As the elasticity approaches the minimum, the entire film is strongly compressed, and the polymer is apparently squeezed out of the surface layer. In this case, the surface pressure is higher than the value corresponding to the maximum elasticity of the pure fullerene film, and a sharp transition is observed from the first branch of the curve to the second branch, corresponding to a highly compressed fullerene film beyond the maximum elasticity of the pure C_{60} film. After this transition, the dynamic surface elasticity begins to decrease and does not reach the maximum value for a pure fullerene film. At the same time, PNIPAM still appears to affect the film properties in this region, and the surface elasticity decreases more smoothly than for a pure C_{60} film (Figure 66).

An increase in the C_{60}/PNIPAM molar ratio leads to a gradual increase in the dynamic surface elasticity of the first maximum and minimum. If this ratio exceeds approximately 10,

then it is impossible to distinguish between the two parts of the dependence, and the found dependences turn out to be close to the results for films of pure C_{60}.

The transition from the first to the second part of the dependence of surface elasticity on surface pressure is accompanied by an increase in the contribution of higher harmonics to surface tension fluctuations. For the first branch this contribution does not exceed approximately 5%.

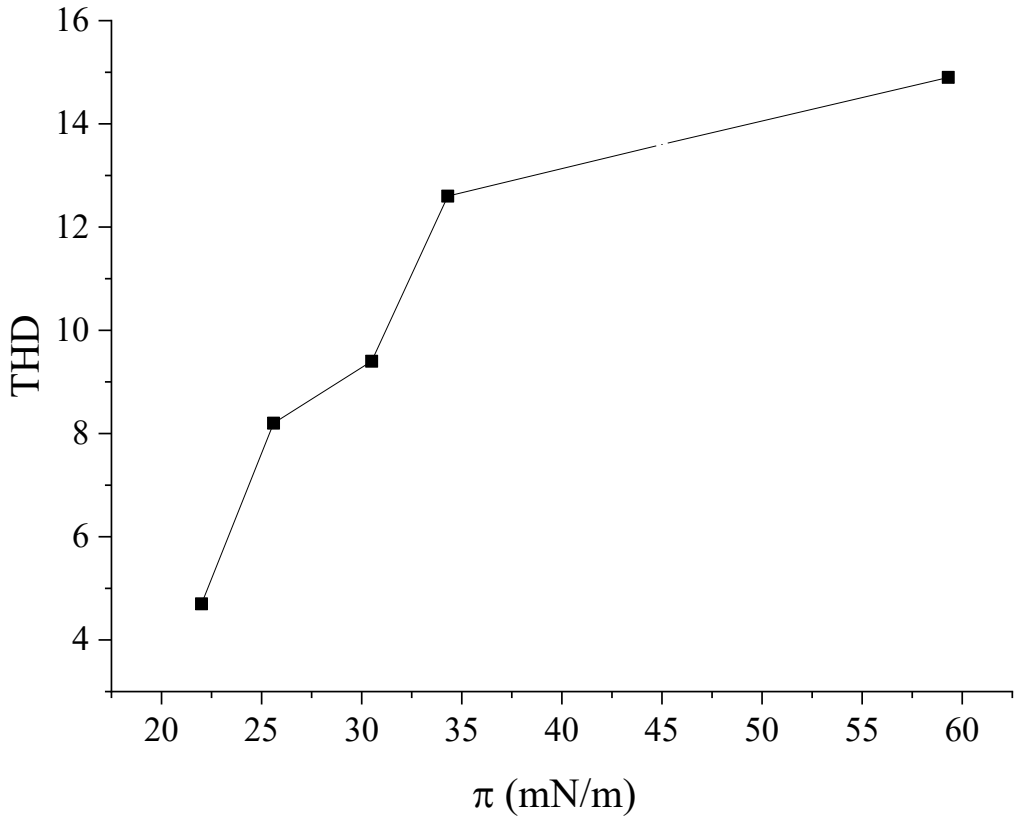

Figure 67. Dependence of the total contribution of higher harmonics to surface tension fluctuations for mixed deposited PNIPAM/C_{60} films at a polymer:fullerene molar ratio of 3.2.

In the transition region between the two parts of the dependence, the contribution of higher harmonics increases significantly (figure 67). In the second part of this dependence, the contribution of higher harmonics reaches approximately 15%, which indicates the inhomogeneity of the deposited film and exchange processes between local elements of the surface structure with characteristic times comparable to the oscillation period [200].

Ellipsometric results indicate macroscopic heterogeneity of the deposited fullerene films even at low surface pressures. Both ellipsometric angles Δ and Ψ change randomly over time. This can occur if the characteristic size of macroscopic surface aggregates (fullerene islands) is comparable to the cross section of the laser beam in an ellipsometer (~ 1 mm) and the aggregates move chaotically along the interface.

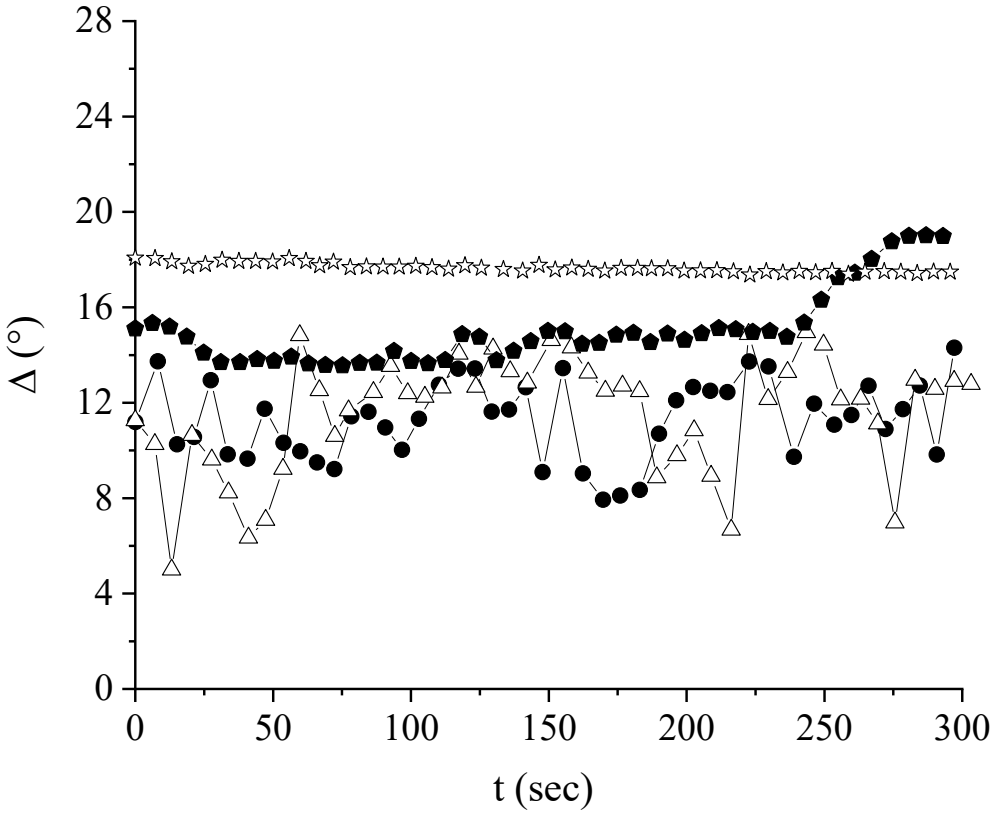

Figure 68. Dependence of the ellipsometric angle Δ on the surface age t for deposited C_{60} fullerene films at various surface pressures: circles – 0.5 mN/m, triangles – 1 mN/m, pentagons – 6.6 mN/m, stars – 63 .1 mN/m.

The dependence of the ellipsometric angle Δ (figure 68) shows that the amplitude of oscillations of the angle Δ increases at the beginning of compression. If the surface pressure exceeds approximately 3 mN/m, the fluctuations become smoother and the time-average value Δ increases. This indicates a slowdown in the movement of surface aggregates and an increase in the average thickness of the deposited film during compression. Fluctuations stop at surface pressures above 50 mN/m, indicating that the layer becomes stationary. The similar behavior of mixed deposited films of C_{60} fullerene and amphiphilic polymers indicates that the polymers

do not have a noticeable effect on the size and mobility of microscopic surface aggregates (figure 69).

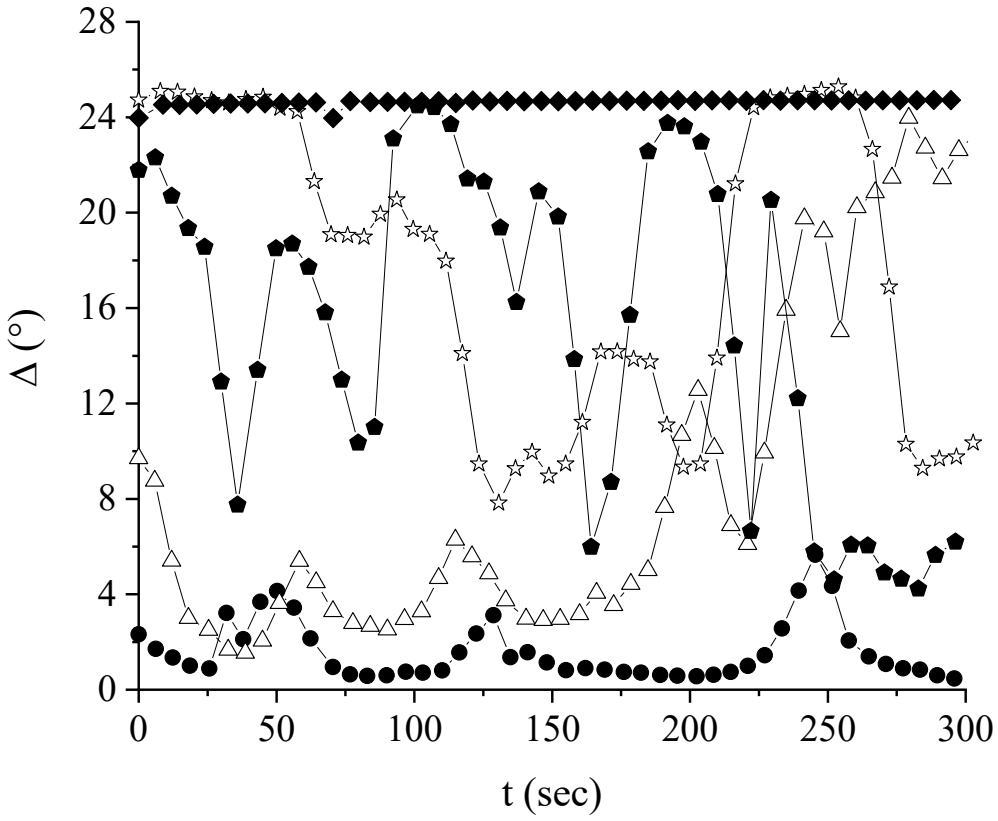

Figure 69. Dependence of the ellipsometric angle Δ on the age of the surface for mixed deposited PVP/C_{60} films at different areas per fullerene molecule: red circles – 1.1 mN/m, triangles – 2.5 mN/m, pentagons – 4.9 mN/m, stars – 52.8 mN/m, diamonds – 65.5 mN/m.

It should be noted that ellipsometric angles are mainly determined by the surface concentration of fullerene, and the contribution of polymers to the angles is much smaller than that of fullerene due to the significant difference in their refractive indices [206]. The constancy of ellipsometric angles over time does not mean that the layer becomes homogeneous. Measurements of ellipsometric angles in different parts of the deposited film in a Langmuir cell can lead to different values and even different kinetic dependences of Δ (figure 70).

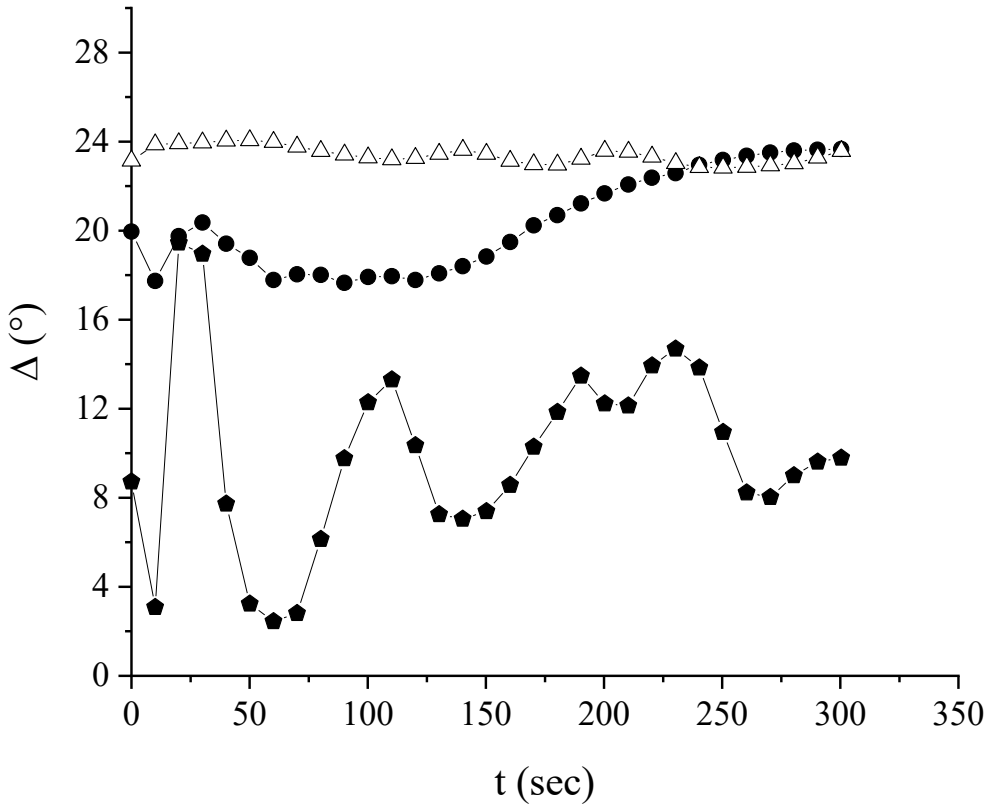

Figure 70. Dependence of the ellipsometric angle Δ on the surface age for mixed deposited PNIPAM/C_{60} films in a Langmuir bath at a surface pressure of 0.6 mN/m and a PNIPAM:C_{60} molar ratio of 0.16.

Brewster angle microscopy allows one to see macroscopic surface aggregates of C_{60} fullerene at relatively low surface concentrations (figure 71), which continuously move along the interface. The brightness of the aggregates changes along their surface, which indicates a change in the thickness of the deposited film. An increase in the surface concentration of fullerene during compression leads to a decrease in the unfilled surface between them, and with a surface area of approximately 0.3 nm^2 per molecule, only small holes are visible in an almost continuous layere (figure 71).

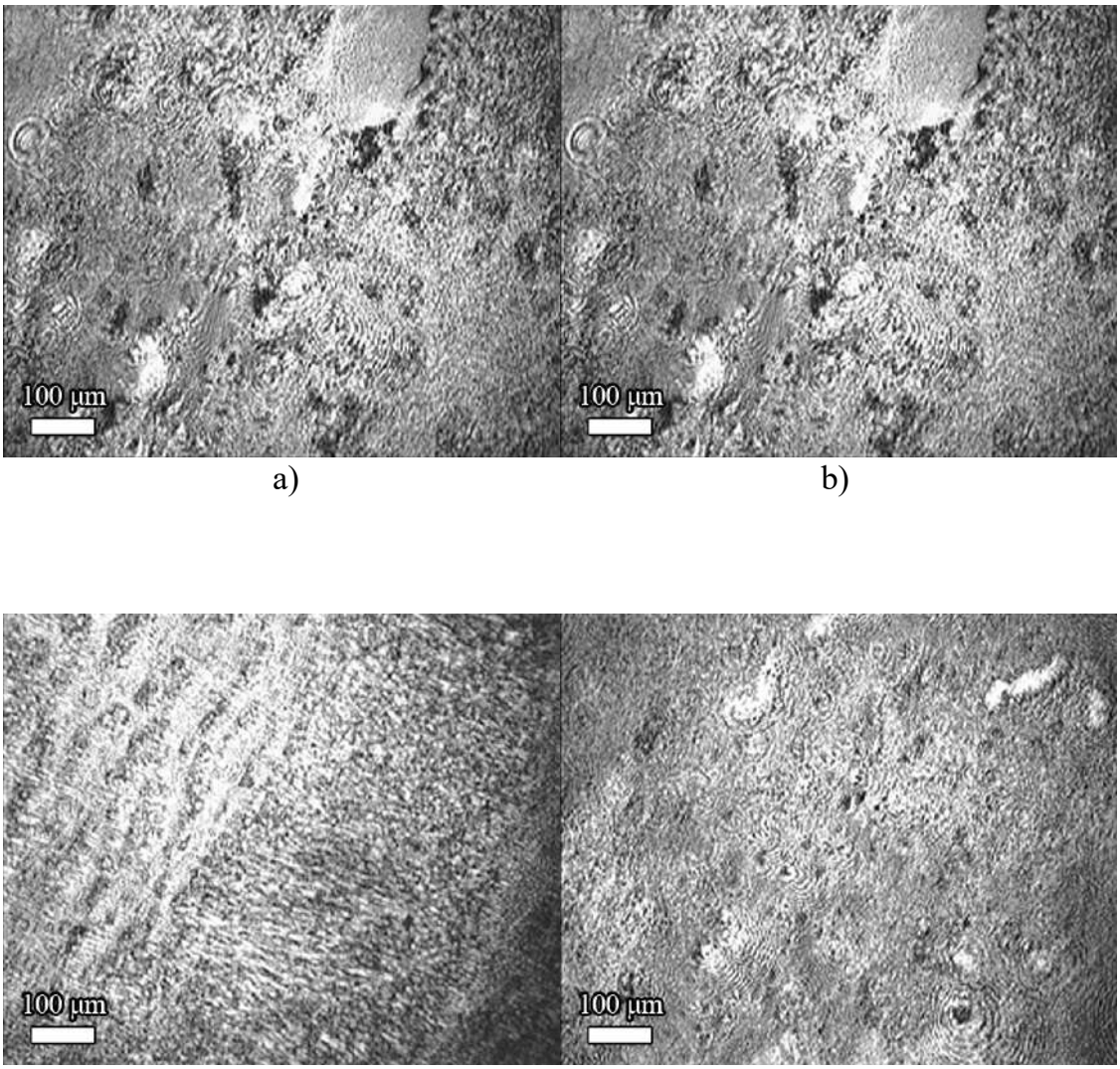

Figure 71. Brewster angle microscope images of a deposited C_{60} fullerene film with areas per fullerene molecule of 0.68 (A), 0.3 (B), 0.19 (C), and 0.12 nm^2 (D).

The movement of the aggregates stops at an area per molecule of approximately 0.3 nm2, but this does not cause noticeable changes in the images obtained by microscopy at the Brewster angle (figure 71), and the surface remains highly heterogeneous. When the area per molecule is less than about 0.15 nm2, stripe patterns can be seen in the layer, which are presumably caused by layer collapse. Similar behavior is observed for mixed deposited C60 films with amphiphilic polymers (figure 72). The only noticeable difference in this case is that the cessation of the movement of aggregates along the surface occurs at large areas per fullerene molecule due to the contribution of the polymer to the surface pressure.

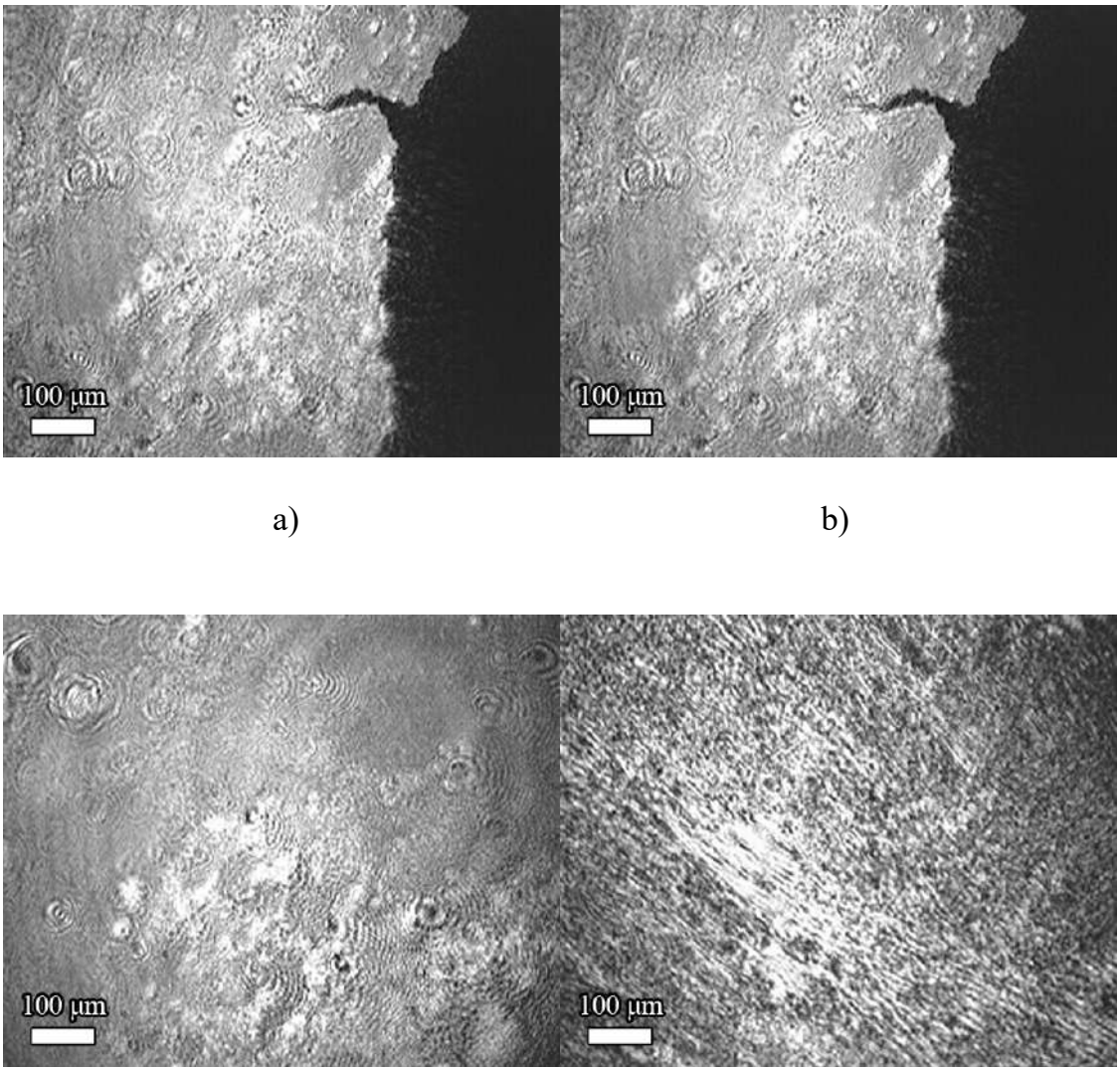

Figure 72. Brewster angle microscope images of a mixed deposited PNIPAM/C_{60} film with area per fullerene molecule values of (a) 0.91, (b) 0.61, (c) 0.19, and (c) 0.15 (d) nm^2 and at a molar ratio of PNIPAM:C60 equal to 3.2.

The heterogeneity of macroscopic surface aggregates can also be seen at low magnification using standard optical microscopy (figure 72, figure 73). The brightness of the islands' surfaces varies depending on their thickness. The edges of the islands are not smooth, indicating that they are formed by a solid-like surface phase. Compression of the surface leads to a decrease in the area not covered by the fullerene layer, and the empty surface practically disappears with an area of approximately 0.3 nm^2 per fullerene molecule.

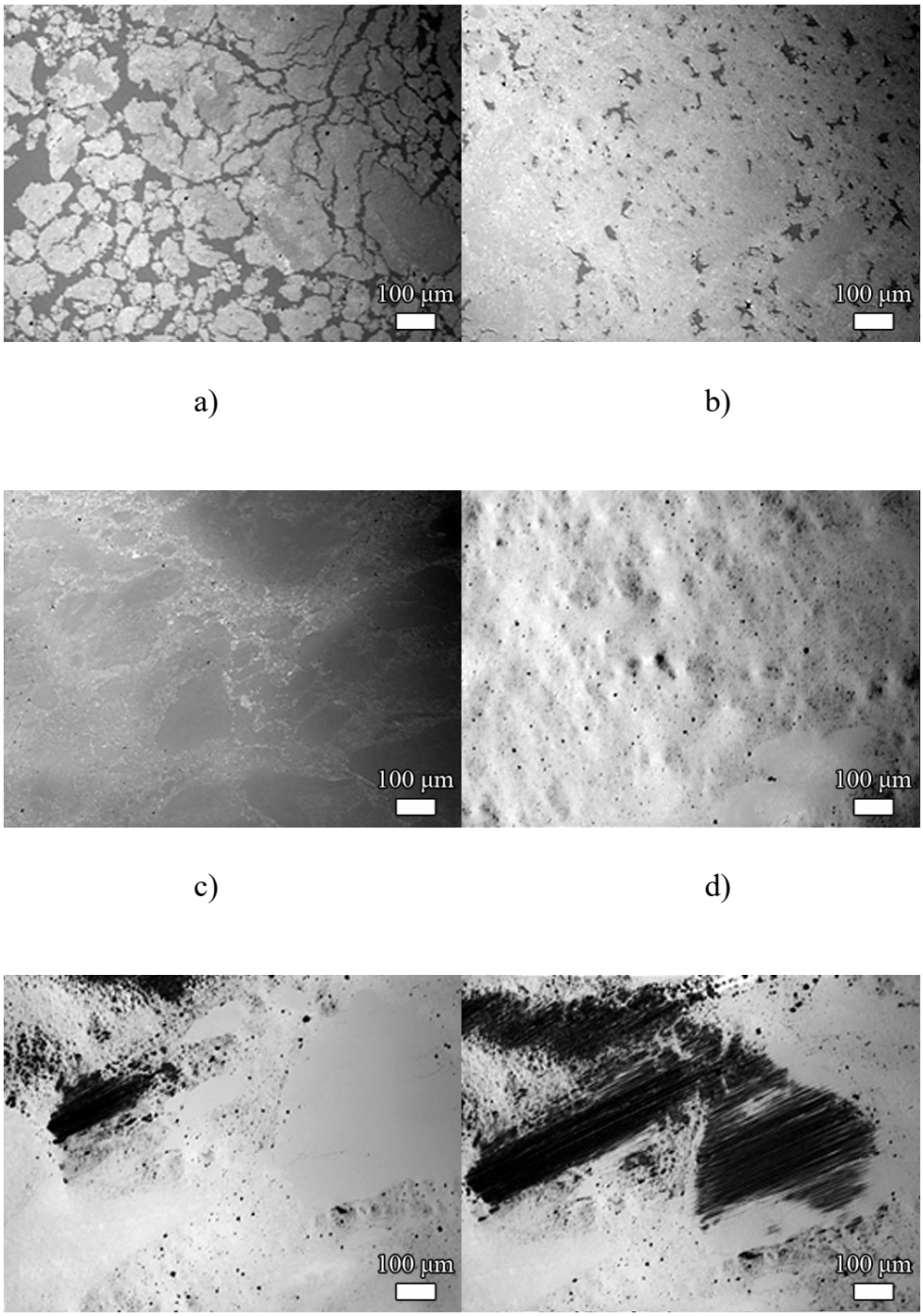

Figure 73. Microphotographs of a deposited C60 fullerene film with area values per fullerene molecule of 0.68 (a), 0.46 (b), 0.3 (c), 0.19 (d), 0.16 (e) and 0.12 nm^2 (f).

With stronger compression, relatively light areas alternate with darker ones, indicating the beginning of layer collapse (figure 73d). If the area per molecule is less than about 0.2 nm^2,

almost black spots can be seen in the micrographs (figure 73e, figure 73f). higher magnification, it is clear that these spots consist of almost parallel dark lines (figure 74). The lines represent folds in the fullerene film.

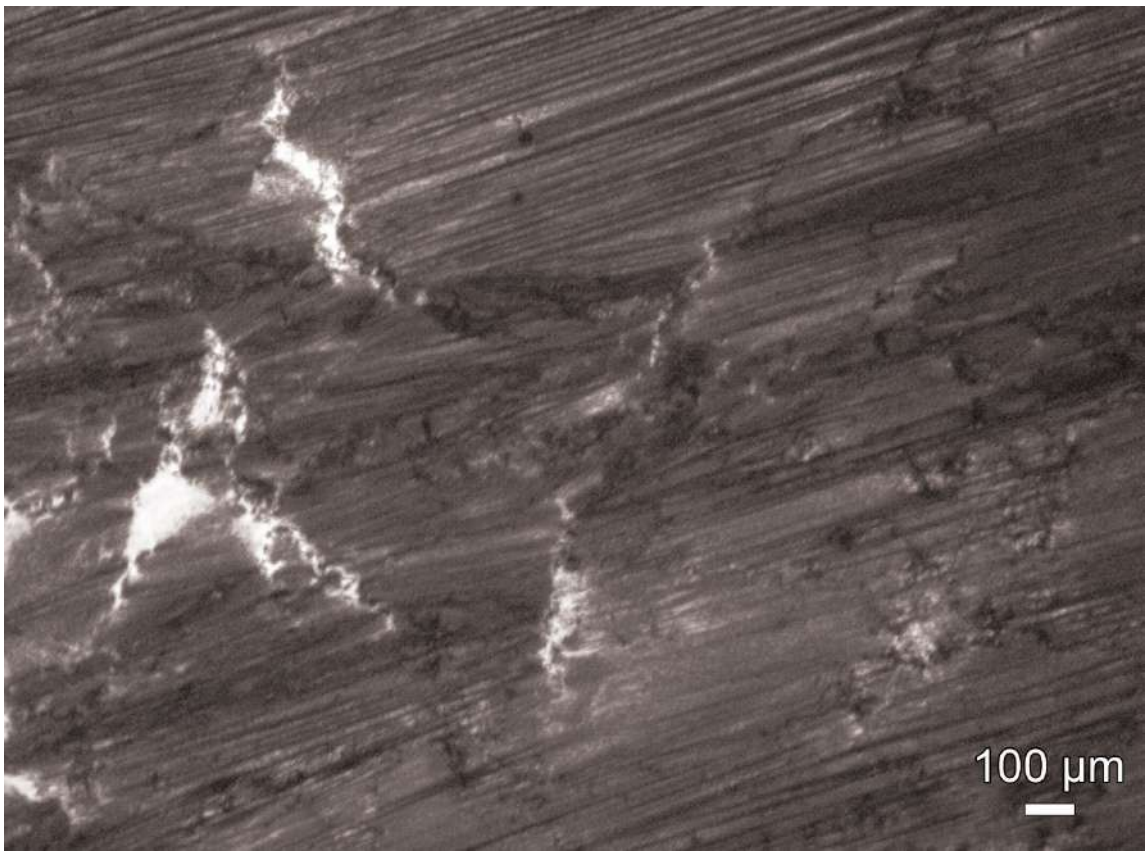

Figure 74. Micrograph of a C_{60} fullerene layer with a surface area per fullerene molecule of 0.15 nm^2.

The distance between the lines (wavelength) varies from 2 to 20 µm and depends on the position of the black spot in the layer. The spots are distributed non-uniformly in the layer at the beginning of its destruction and correspond to local areas of relatively high surface stresses. They initially appear next to moving barriers and appear in other parts of the layer only after its destruction. Their area decreases if compression stops due to the gradual relaxation of local surface stresses (figure 75). Increasing the surface pressure to 70 mN/m increases the number and area of black spots, and they become visible to the naked eye. Therefore, the collapse of the C_{60} film, in contrast to the collapse of the layer of insoluble surfactants, occurs in a wide range of surface pressures from approximately 30 to 70 mN/m.

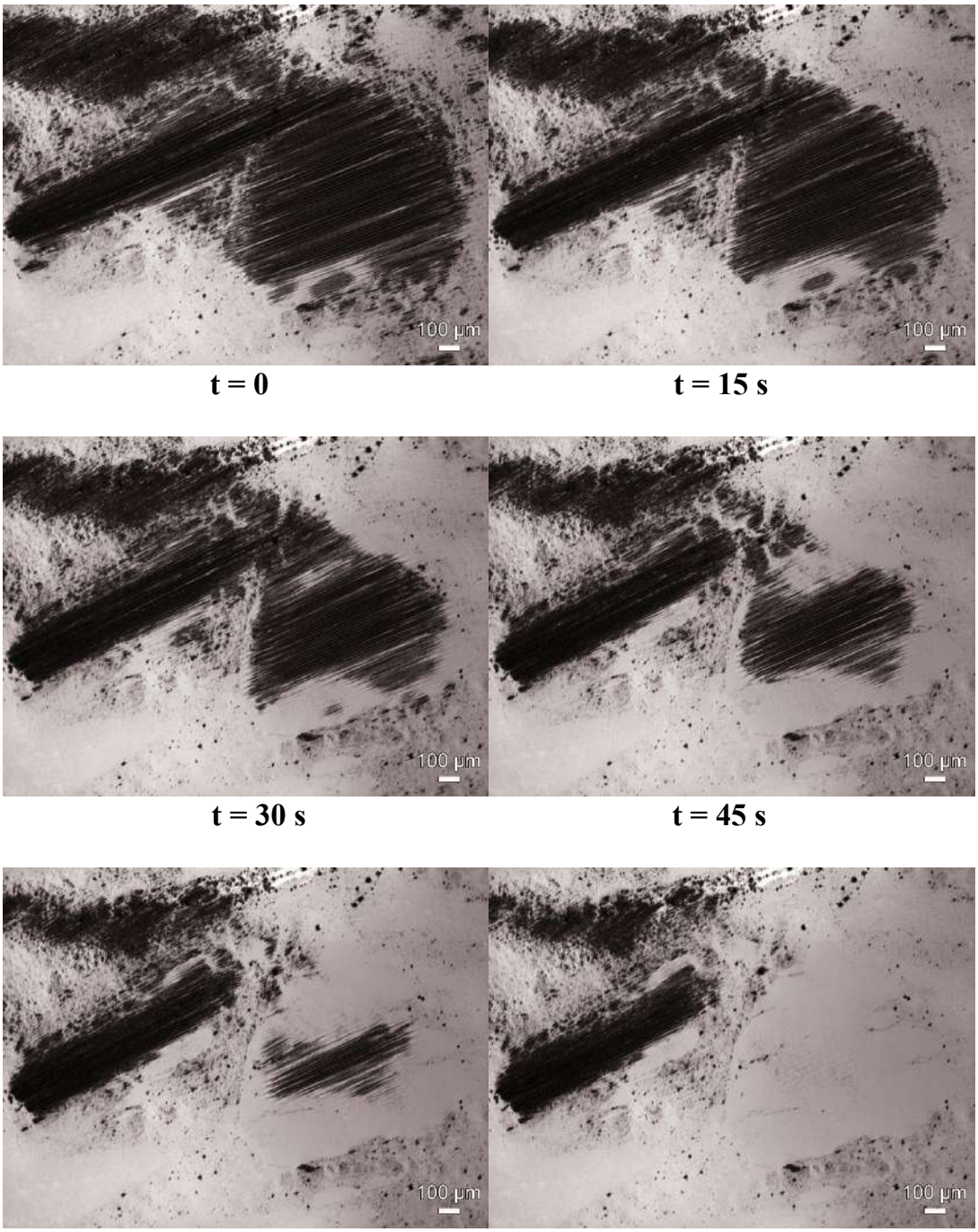

Figure 75. Change in time of the black spot in the deposited fullerene film with a surface area per fullerene molecule of 0.19 nm^2, after the termination of surface compression.

Further sharp stretching of the fullerene film leads to the formation of numerous cracks in the layer, followed by segmentation (figure 76). The main features of the collapse of mixed films of C60 fullerene and amphiphilic polymers do not differ noticeably from those for C_{60} films (figure 77).

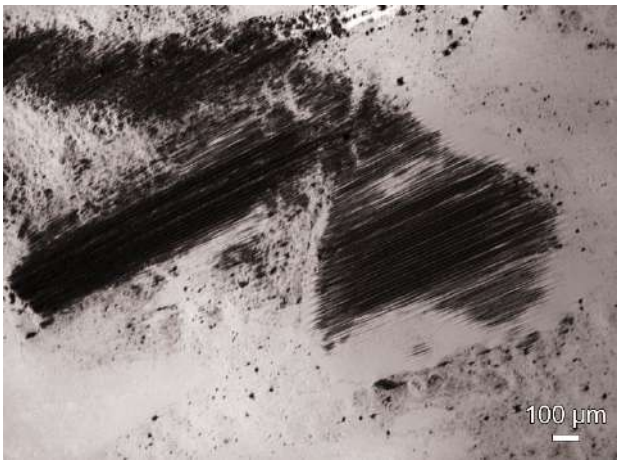

A

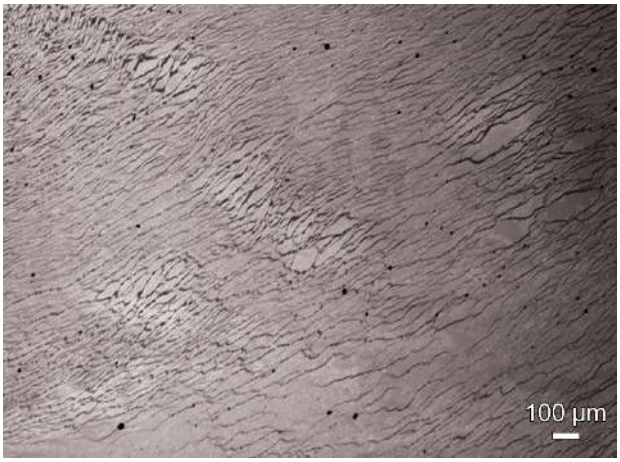

B

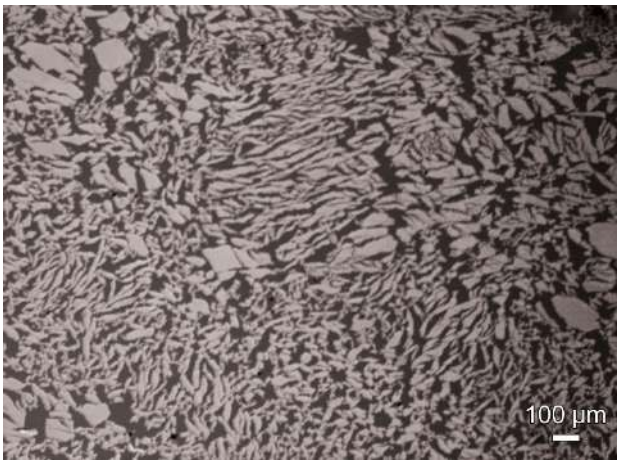

C

Figure 76. Microphotographs of a deposited C60 fullerene film during stretching with an area per molecule of 0.15 (A), 0.19 (B) and 0.3 nm^2 (C).

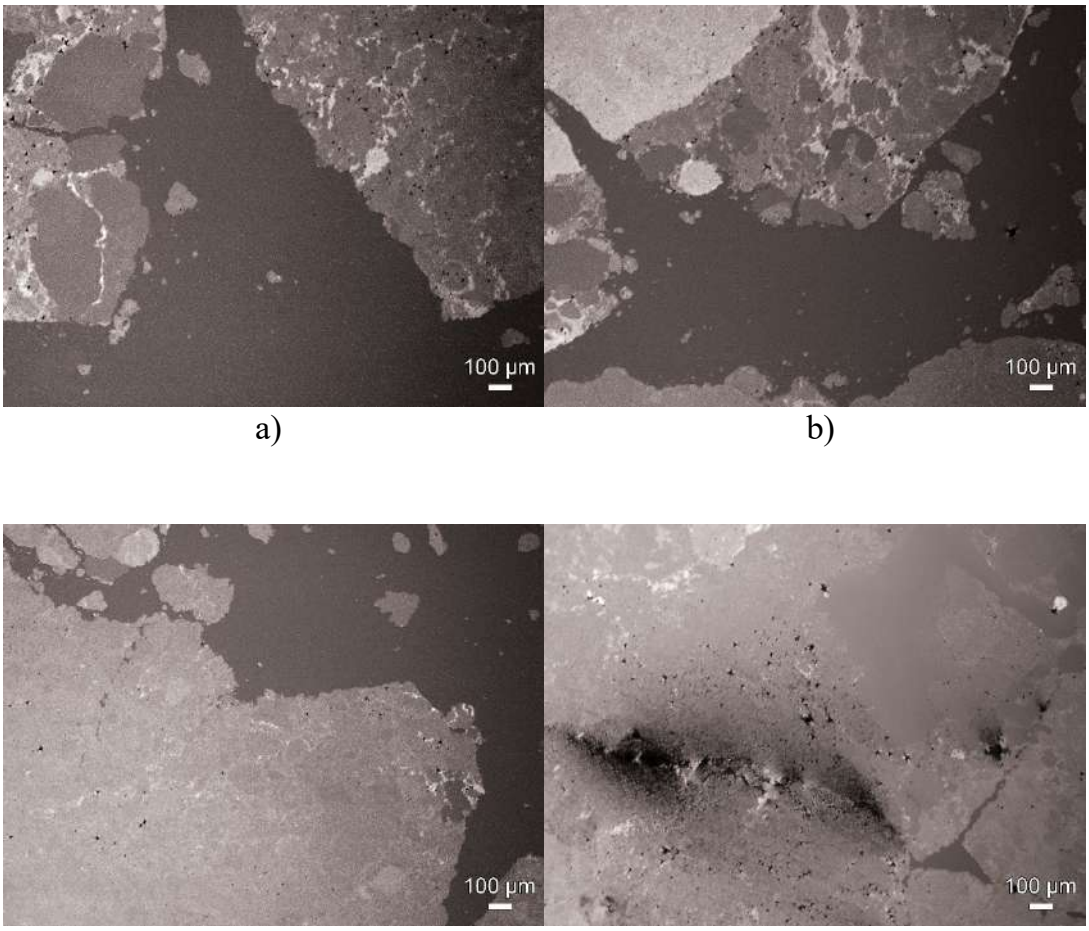

Figure 77. Microphotographs of mixed deposited PNIPAM/C_{60} films with area values per fullerene molecule of 0.91 (a), 0.61 (b), 0.27 (c) and 0.15 (d) nm^2 and at a molar ratio of PNIPAM: C_{60}, equal to 3.2.

The use of AFM on deposited C_{60} films transferred from a water surface to a mica plate shows that they are highly heterogeneous at the microscale. At low surface concentrations they are mainly a mixture of mono-, bi- and tri-layers (figure 78). As surface pressure increases, in addition to these relatively thin films, regions of larger surface aggregates can also be seen. In this case, most of the area is occupied by aggregates with dimensions of approximately 40-60 nm in diameter and approximately 20-40 nm in the Z direction. Larger aggregates with dimensions of 100–200 nm in diameter and 50–120 nm in Z direction occupy only a small part of the AFM image. It should be noted that such large aggregates have not been observed for films of pure polymer, but are typical for layers of films with fullerene [35] An increase in surface concentration during compression leads to an increase in the area occupied by large

aggregates in AFM images, and at surface pressures above about 50 mN /m large aggregates presumably occupy the entire area in the Langmuir cuvette between the barriers. In this case, the unfilled surface between the aggregates decreases, and the overall density of the layer increases (figure 78).

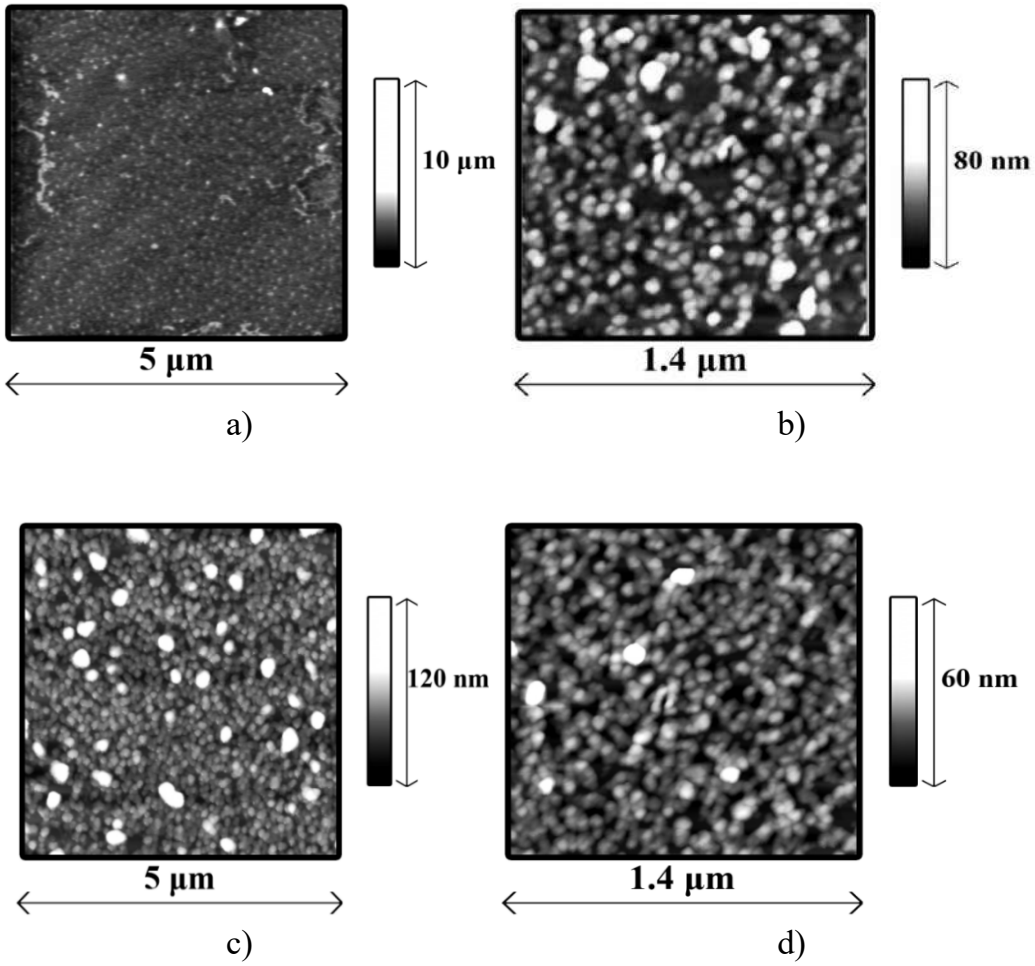

Figure 78. AFM images of a deposited C_{60} fullerene film at surface pressures of 5 (A), 30 (B), 45 (C) and 60 (D) mN/m.

The addition of amphiphilic polymers to the film does not lead to a significant change in its micromorphology, and AFM images of mixed films are close to those for pure C_{60} film with an increase in the number of large surface aggregates at high surface concentrations (figure 79). C_{60}/polymer blend films are slightly smoother and there is on average slightly less free surface area between microaggregates. It can be assumed that polymers contribute to the formation of the shell of surface microaggregates.

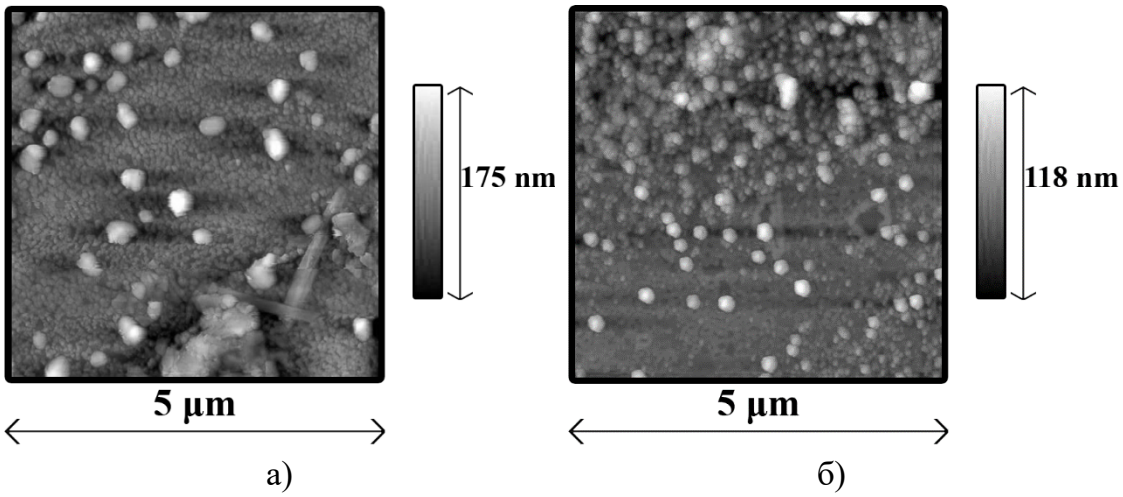

Figure 79. AFM images of deposited C_{60}/PNIPAM (A) and C_{60}/PVP (B) films at a surface pressure of 60 mN/m.

The results obtained confirm the high resistance to mechanical deformation of C_{60} fullerene films in the aqueous subphase. These films can withstand surface pressures of up to 70 mN/m, and their tensile elasticity can reach very high values, up to approximately 370 mN/m. Although the surface elasticity decreases with strong surface compression, the morphology of the fullerene film does not change noticeably with time after the end of compression, even at surface pressures up to 70 mN/m. This behavior is due to the strong adhesion of the surface film of fullerene to water.

The properties of mixed films of C_{60} and amphiphilic polymers provide further evidence of such strong adhesion. Dependences of the dynamic elastic modulus on surface pressure with two local maxima for mixed deposited films show that they consist of two separate surface phases (figure 63, figure 65). In the surface pressure ranges from zero to about 4 mN/m for PVP/C_{60} films and from zero to 29 mN/m for PNIPAM/C60 films, the surface properties are typical of amphiphilic polymer films. For example, if the PNIPAM/C_{60} molar ratio is higher than 3, the dependences of the surface elastic modulus on surface pressure for mixed films coincide with the dependences for deposited films of pure polymer. If this ratio decreases, the area covered by fullerene increases at the same surface pressure and the surface elasticity increases, resulting in a higher peak. This effect is a consequence of the significant difference in elasticity of the two coexisting surface phases. In this case, compression and stretching of the film leads to a slight deformation of the more elastic fullerene phase and a significantly

greater relative deformation of the polymer phase for the same total surface deformation, which is consistent with the Lucassen relation [207]

$$\frac{1}{|\epsilon|} = \frac{F_1}{|\epsilon_1|} + \frac{F_2}{|\varepsilon_2|} \quad (1)$$

where F_1 и F_2 — area fractions of two surface phases with elastic moduli ε_1 and ε_2, respectively.

If the surface pressure exceeds approximately 29 mN/m, the surface properties are determined by the fullerene, and the dependence of the dynamic elastic modulus on surface pressure for mixed films is close to those for films of pure C_{60} (figure 57, figure 65). PNIPAM can only slightly influence this relationship at surface pressures above approximately 50 mN/m (figure 66). These results show that although PNIPAM is an amphiphilic polymer with high surface activity, it is displaced by fullerene from the proximal region of the surface layer upon surface compression. This process can result in an increase in the length and number of loops and tails penetrating into the bulk phase while C_{60} is still forming a film on the surface of the water. Polymer displacement can be seen using standard optical microscopy and Brewster angle microscopy (figure 72, figure 75). The gaps between solid-like macroscopic aggregates, i.e., the area covered by the polymer, gradually decrease, and eventually only a continuous dense layer is visible. Figure 78 shows that the continuous phase consists mainly of fullerene aggregates at the micro level.

The appearance of stripes in micrographs (figure 71 - figure 74) nder strong compression resembles similar changes for monolayers of solid micro- and nanoparticles at high surface pressures and indicates destruction of the layer structure[208–211]. The collapse of a monolayer of insoluble surfactants at the liquid-gas interface occurs spontaneously if the surface pressure exceeds a certain value, known as the collapse pressure [212–214]. This value is usually higher than the surface pressure corresponding to the equilibrium between the monolayer and three-dimensional aggregates at the interface. Therefore, collapse can be described as a transition from a stable metastable state of the layer to an unstable one, accompanied by the formation of three-dimensional aggregatesв [213]. Collapsed structures vary between systems and may consist of bilayer platelets or thick and tall ridges at the interface [212]. In the case of multicomponent monolayers, such as pulmonary surfactant monolayers, this process becomes more complicated and can lead to the transition of part of

the layer into a subphase [214]. The collapse of monolayers of low molecular weight surfactants usually results in a kink or plateau in the surface pressure isotherm at a certain collapse pressure. When comparing the microphotographs, it is clear that this is not the case for the C_{60} and polymer/C_{60} films. The results obtained are closer to the surface pressure isotherms for monolayers of solid micro- and nanoparticles, when determining a specific collapse pressure is difficult due to smoother compression isotherms [208–211,215–218].

Although detection of kinks in compression isotherms of layers of solid particles is not always possible, optical micrographs (for example, (figure 71) (figure 73)), can usually reveal the formation of three-dimensional structures in films at the liquid-gas interface [208,209,211,217]. The mechanism of destruction of monolayers of solid particles can vary significantly depending on the particle size [211], shape and degree of amphiphilicity [210,217]. Out-of-plane deformations are irreversible for monolayers of weakly amphiphilic microparticles, and an increase in the degree of amphiphilicity leads to the reversible formation of wrinkles and folds when the monolayer is compressed. The destruction of monolayers of polystyrene microparticles usually occurs by bending the monolayer [199,201,202,219]. In the case of silica microparticles, the collapse mechanism may depend on the degree of their hydrophobicity and the ionic strength of the subphase [210]. More hydrophobic particles form wrinkles and folds that disappear when the monolayer is stretched, while monolayers of less hydrophobic particles undergo reversible or irreversible collapse due to the displacement of particles into the bulk phase.

Although the deposited fullerene film is not a monolayer, optical micrographs (figure 71, figure 73) show the formation of dark lines at surface pressures above the values corresponding to the maximum dynamic surface elasticity. These lines are characteristic of destroyed monolayers of various micro- and nanoparticles [208–211] and may indicate similar processes in fullerene films. An increase in surface pressure can lead to a redistribution of fullerene molecules between various surface aggregates and the surrounding layer. At the same time, patterns in the film indicate the formation of meso- or macroscopic folds in the monolayer, which become visible with slight magnification or even with the naked eye. The exchange of molecules between the folds and the surrounding film can contribute to the reduction of dynamic surface elasticity at surface pressures above approximately 25 mN/m (figure 57, figure 63, figure 65). Dark lines in micrographs (figure 71, figure 73) may be shorter than in layers of other micro- and nanoparticles, and do not necessarily be

perpendicular to the direction of compression. Apparently, this is a consequence of the heterogeneity of the layer, in which there are areas of different strength.

Distinct dark lines (figure 71, figure 73) cannot be attributed to the ejection of particles into the subphase, since in this case the images are usually blurred [210]. Such images (figure 71, figure 73), appear for layers of gold nanoparticles when compaction of the layer leads to wrinkling [208] or when cross-linked gold nanoparticles begin to form folds[211]. Distinct folds in fullerene films mean that the amplitude of the folds exceeds variations in the thickness of the unperturbed layer and can exceed 50 nm. Under strong compression, the layer mainly consists of fullerene nanoaggregates with a diameter in the range of 40 – 60 nm. Therefore, the folds are presumably formed by these aggregates and not by smaller fullerene molecules (figure 80). Addition of amphiphilic polymers to the layer does not lead to visible changes in the nature of folds.

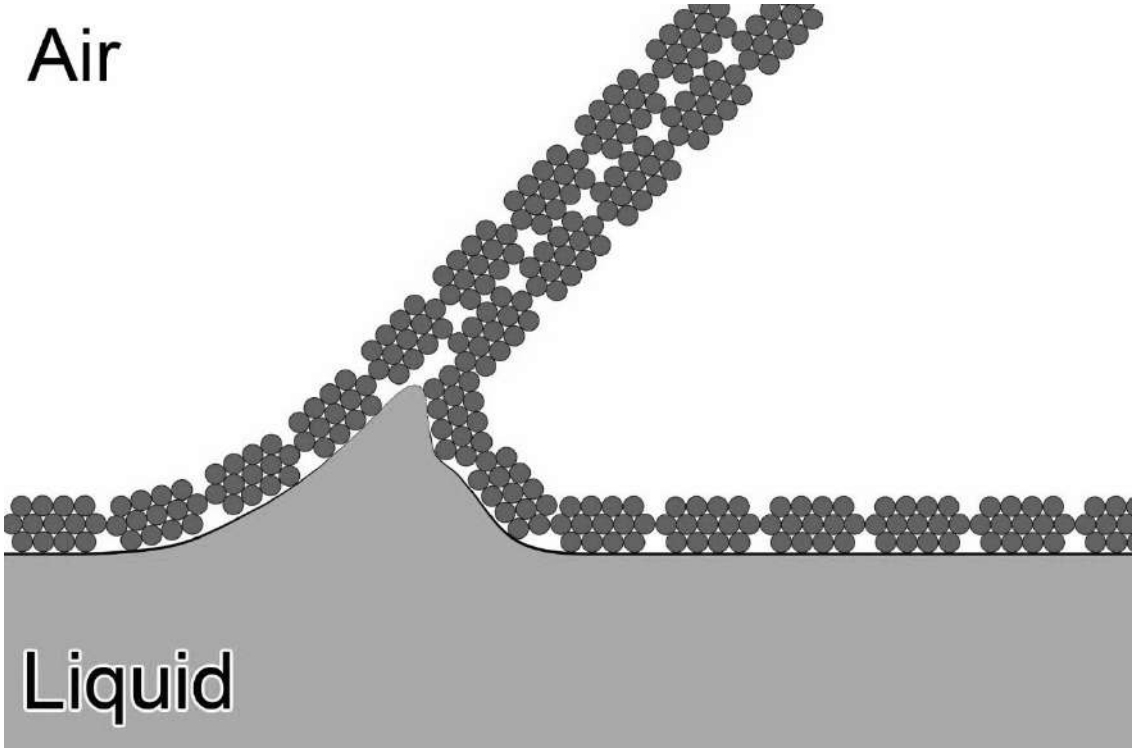

Figure 80. Scheme of destruction of a film of fullerene aggregates during bending and formation of folds.

The collapse of the deposited fullerene film begins as local wrinkling at relatively low surface pressures (≥ 30 mN/m) and develops at significantly higher surface pressures up to 70 mN/m. Even in a highly compressed state, the film consists of large folds and individual sections of the unbroken layer. The formation of such a complex structure can be explained by

the heterogeneity of the film and strong adhesion to water. The attraction of fullerene molecules to water apparently weakens at the boundaries of relatively homogeneous areas of the layer, where folds begin to appear. Defects in the structure of the deposited film and the non-uniform distribution of surface stresses can explain the apparent contradiction between the onset of destruction of the layer at relatively low surface pressures and the ability of the layer to withstand surface pressures up to 70 mN/m. The behavior of mixed films of C_{60} fullerene and amphiphilic polymers also confirms the strong attraction of fullerene molecules to water. This strong interaction is not consistent with the hydrophobic effect, which usually results in the displacement of hydrophobic particles from water. Spectroscopic data from two groups show that immersion of C_{60} molecules in water leads to hydroxylation of its surface [220,221]. Although the exact mechanism of hydroxylation is not well understood, it explains the stabilization of C_{60} aggregates in water. It can be assumed that in a multilayer at the water-air interface, the fullerene monolayer closest to the water is also hydroxylated, at least partially, which leads to the formation of hydrogen bonds between water and the resulting fullerenol, thereby creating a strong attraction. The heterogeneity of fullerene films can lead to difficulty in the formation of fullerenols in some small areas of the layer, where the formation of folds begins.

The properties of deposited C_{60} fullerene films at the water-air interface indicate strong adhesion of the layers to water. The layers can withstand surface pressures of up to 70 mN/m. The dynamic tensile elasticity of the films reaches approximately 370 mN/m at surface pressures close to 25 mN/m, and then gradually decreases. Ellipsometric measurements and microscopy at the Brewster angle show that the layer has a variable thickness. According to AFM, it is primarily a bilayer or trilayer at low surface pressure, but it can contain large aggregates with a Z-size of up to about 100 nm. The number of these tall aggregates increases as surface pressure increases, but most surface aggregates measure approximately 40–60 nm in the X-Y plane and approximately 20–40 nm in the Z direction. A local maximum in surface elasticity may indicate the onset of layer failure. This conclusion is confirmed by optical micrographs that record the beginning of the formation of meso- and macroscopic folds in the layer at surface pressures above 30 mN/m. This behavior is similar to that of three layers of gold nanoparticles. The macroscopic morphology of some areas of the deposited fullerene film does not change even at surface pressures close to 70 mN/m, and these areas coexist with

numerous folded structures. The dependences of dynamic elasticity on surface pressure of mixed deposited C_{60} films with amphiphilic polymers PVP and PNIPAM have two local maxima and can be divided into two parts, where the surface elasticity is determined by the polymer or fullerene. For example, the dynamic elasticity of mixed PNIPAM/fullerene films almost coincides with the dynamic elasticity of deposited films of pure PNIPAM at surface pressures up to approximately 29 mN/m, if the PNIPAM/fullerene molar ratio is greater than 3. At lower molar ratios, only an indirect effect of fullerene on dynamic elasticity is visible. If the surface pressure exceeds 29 mN/m, then the dynamic elasticity of the surface is determined mainly by fullerene. The polymer has little effect on surface elasticity only at high surface pressures (> 50 mN/m). The properties of deposited C_{60} films and mixed C_{60}/polymer films at high surface pressure are due to the strong adhesion of the layers to water.

4.2 Properties of C_{60} fullerene microaggregates on the water surface

Fullerene aggregates of various shapes (rods and tubes) were obtained using the MOLJ method. Rod-shaped microaggregates are relatively large particles with a diameter of about 2 and a length of 15-20 microns (figure 81 - figure 82). Although they retain their shape when transferred to the liquid phase, when they are applied to an aqueous surface from a solution in toluene, successful transfer was not achieved, which is apparently due to the sedimentation of relatively large MRC_{60} particles, as a result of which the surface properties are determined by the admixture of other smaller fullerene aggregates or fullerene molecules.

Thus, the compression isotherm and the dependence of surface pressure on dynamic surface elasticity are not very different from the results for a film of pure C_{60} (figure 84). The use of the AFM method also did not allow us to detect particles in the form of microrods on the surface (figure 85).

In contrast to MRC_{60}, the diameter of NTC_{60} is significantly smaller, with a comparable length. These particles are better applied to the surface of a liquid and form a film on the water surface, just like pure fullerene and its mixtures with amphiphilic polymers. At the initial moment of time, after 1 ml of NTC_{60} dispersion is applied to the surface of the liquid and the solvent evaporates, there appear to be separately floating nanotubes on the surface that do not interact with each other (figure 86). n this case, the surface pressure is zero.

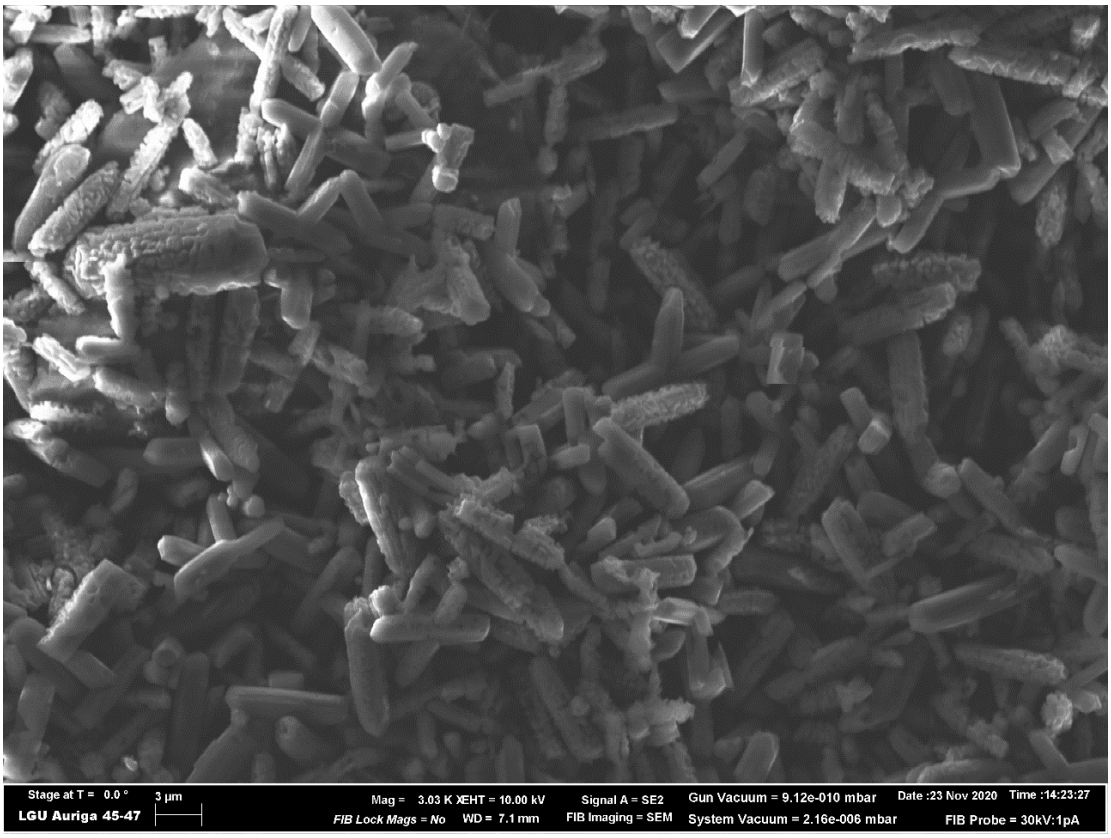

Figure 81. SEM images of MRC60 powder.

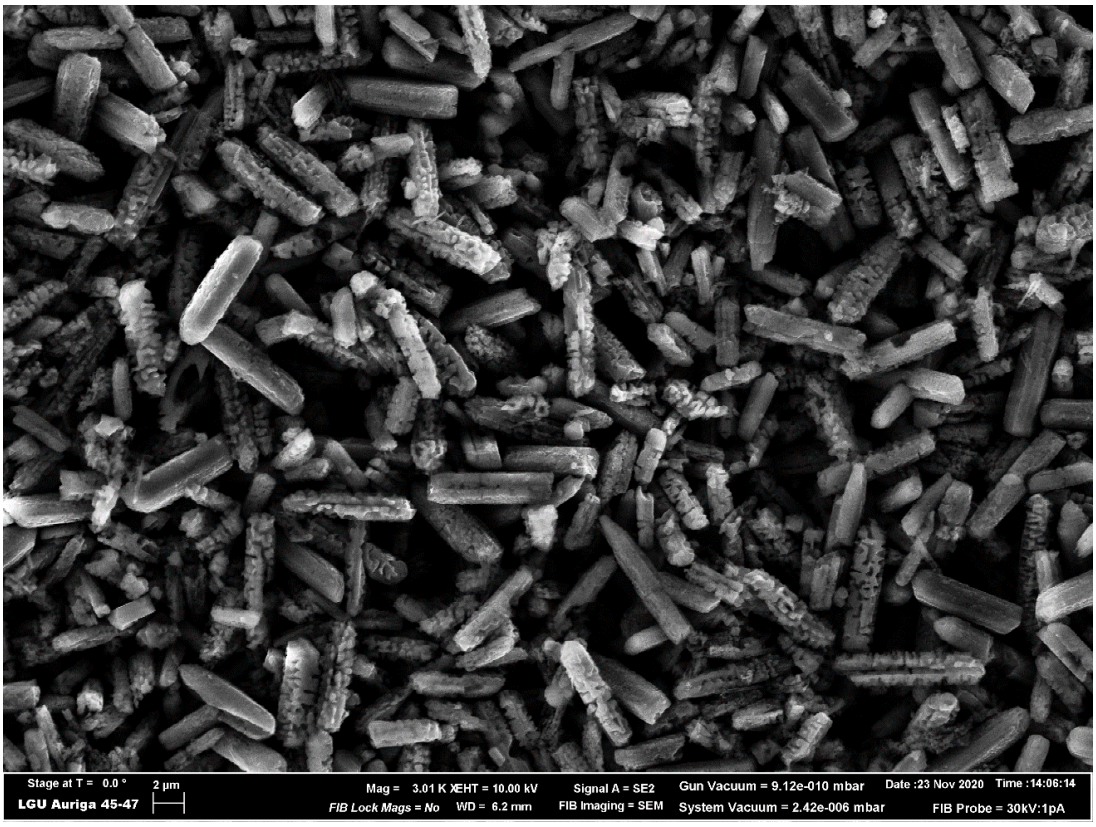

Figure 82. SEM images of MRC_{60} powder toluene solution.

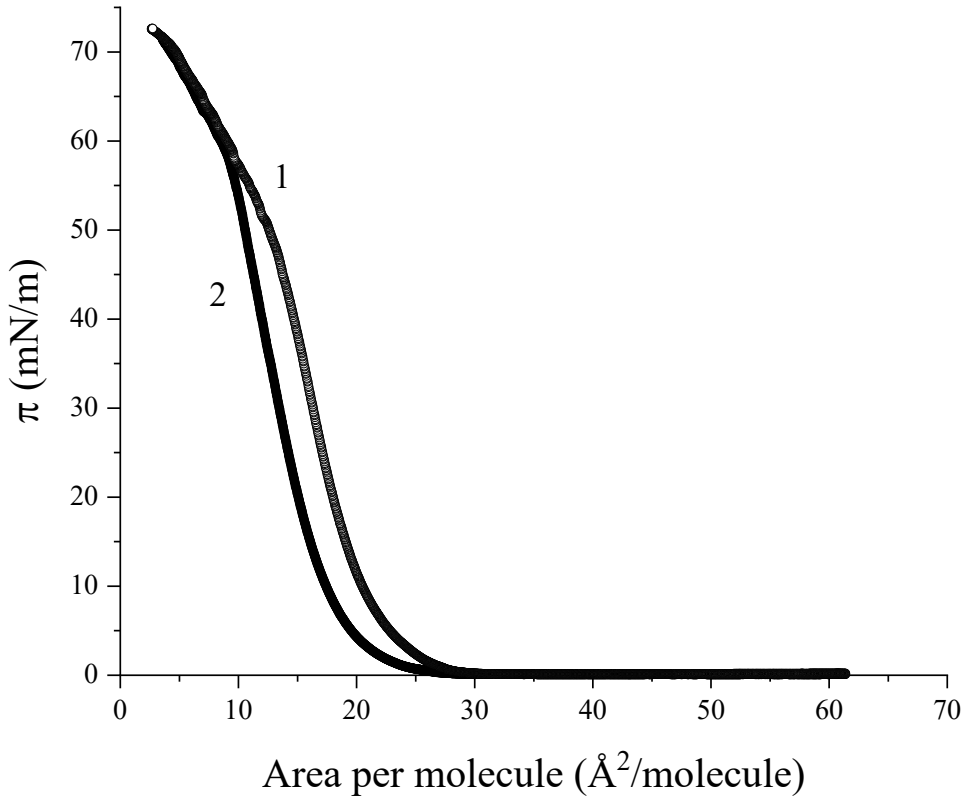

Figure 83. Compression isotherms of deposited films of pure fullerene C_{60} (1) and MRC_{60} (2). Spreading volume – 100 μl.

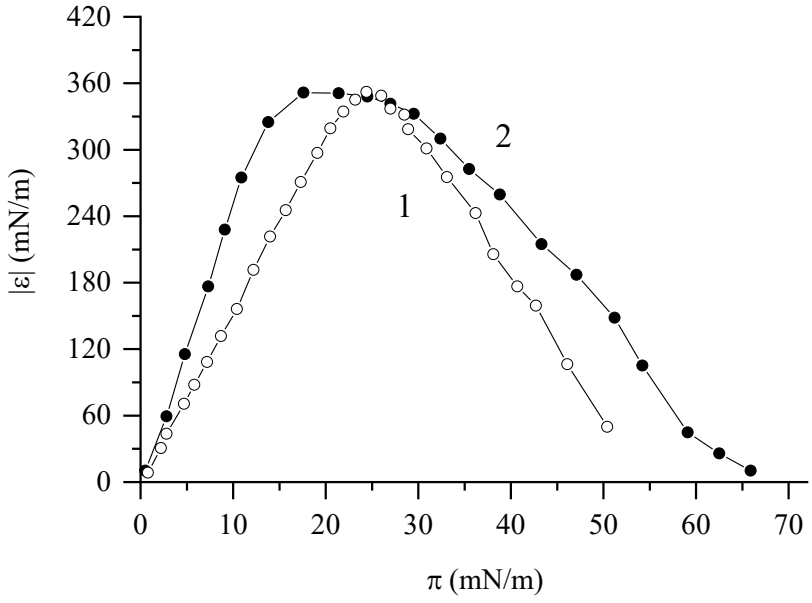

Figure 84. Dependences of dynamic surface elasticity on surface pressure of deposited films of pure fullerene C_{60} (1) and MRC_{60} (2). Application volume – 100 μl.

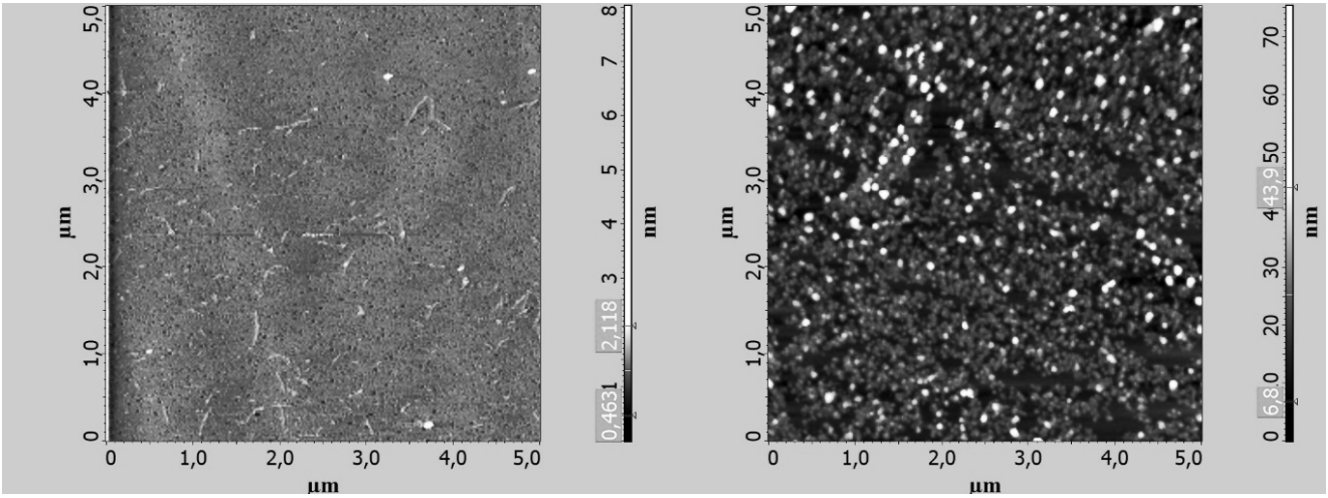

а) б)

Figure 85. AFM images of a deposited MRC_{60} film at a surface pressure of 5 (A), 60 (B) mN/m.

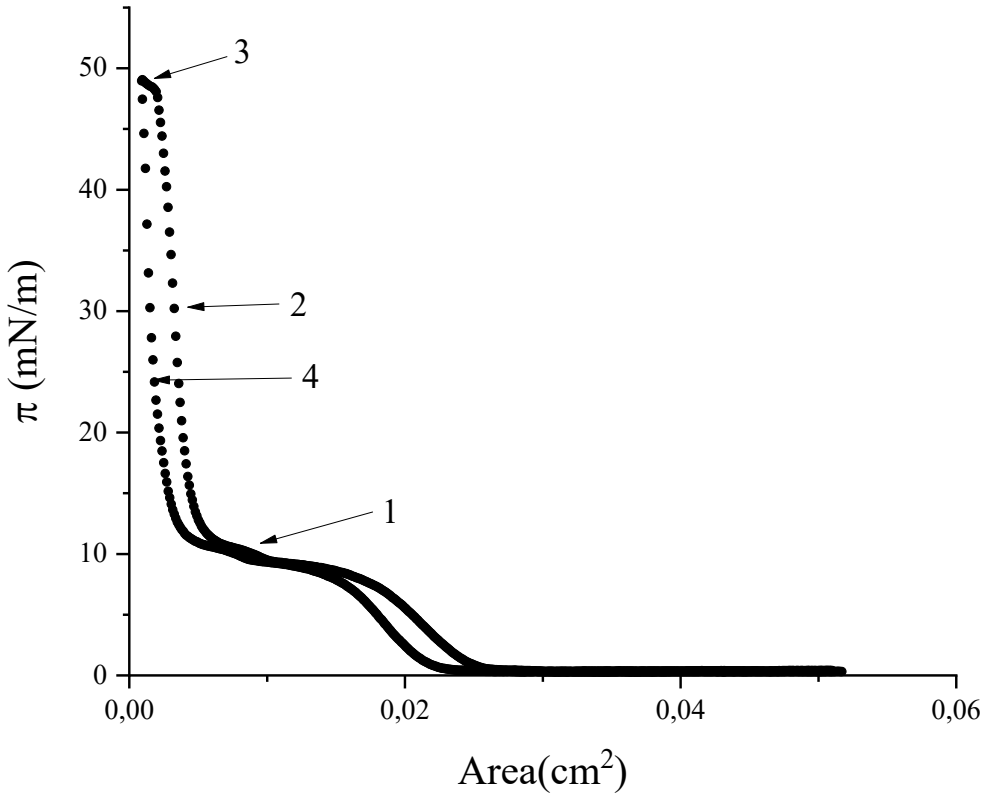

Figure 86. Compression and extension isotherms of a deposited layer of NTC_{60} dispersion on a water surface.

In this case, the film of particles on the water surface can be characterized as a monolayer. As compression proceeds, the NTC_{60} particles come closer together and begin to interact, which leads to an increase in surface pressure, starting from approximately 0.025 cm^2. SEM images obtained after transferring the film from the water surface to the surface of the silicon wafer (figure 87), show that in the initial section of the compression isotherm (figure 86, plateau region, section 1) the number of contacts of NTC_{60} particles is relatively small. The deposited film turns out to be microhetergeneous: in the region of the plateau of the compression isotherm, areas with varying degrees of overlap of nanotubes coexist in it. Concentrated regions of the film with a relatively large number of contacts between nanotubes can be considered as a separate surface phase. Then the plateau region of the compression isotherm corresponds to a two-dimensional phase transition. In this region, the surface pressure is approximately constant, and the dynamic surface elasticity is close to zero (figure 88). Further compression of the film gradually leads to the formation of a continuous concentrated surface phase with a large number of contacts between nanotubes (figure 86, section 2 on the compression isotherm). In this case, the surface pressure and surface elasticity increase rapidly during compression (figure 88). At a surface pressure of about 35 mN/m, the surface elasticity reaches its maximum value. With a further increase in surface pressure, the nanotubes apparently begin to collapse. If the surface pressure reaches approximately 48 mN/m (figure 86, участок 3), area 3), then SEM images indicate the formation of relatively short nanotubes. In this case, the number of intersections of nanotubes increases (figure 90), and the surface film becomes a multilayer. The rapid increase in surface pressure stops (figure 86), the surface pressure remains almost unchanged with further compression of the film, and the surface elasticity decreases (figure 88). This state can be characterized as the collapse of the NTC_{60} film. On the film stretching isotherm, a two-dimensional phase transition can again be observed, corresponding to the formation of a surface phase with a relatively low concentration of nanotubes (figure 86, section 4).

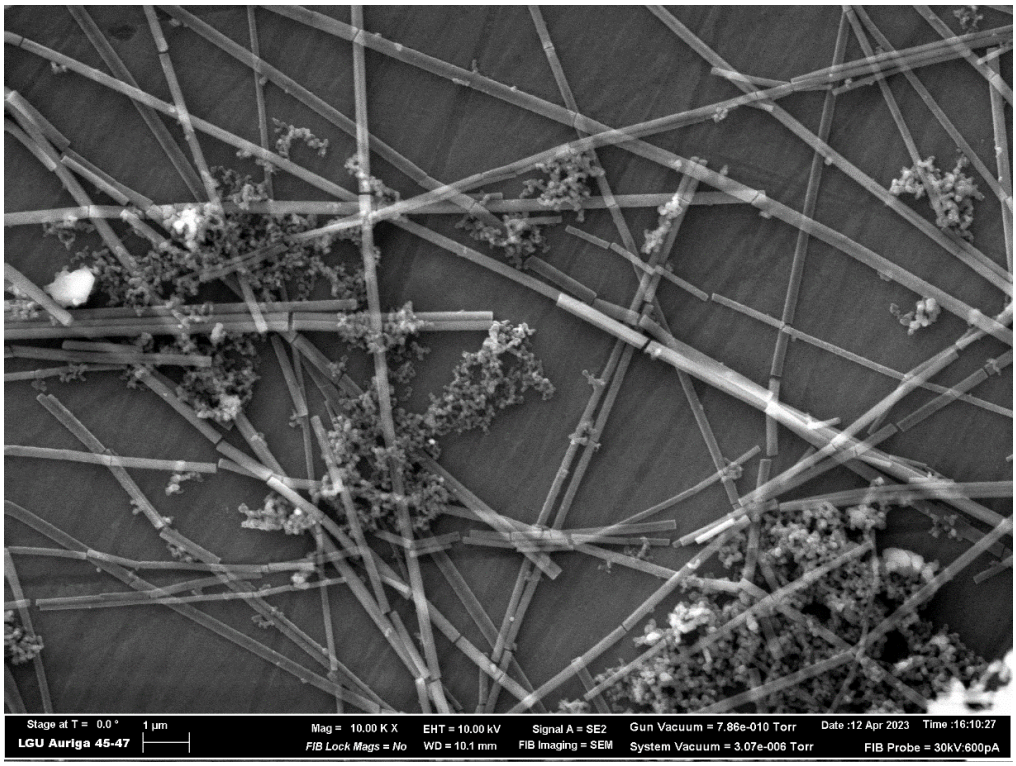

Figure 87. SEM image of the HTC60 film in the plateau region of the compression isotherm (section 1).

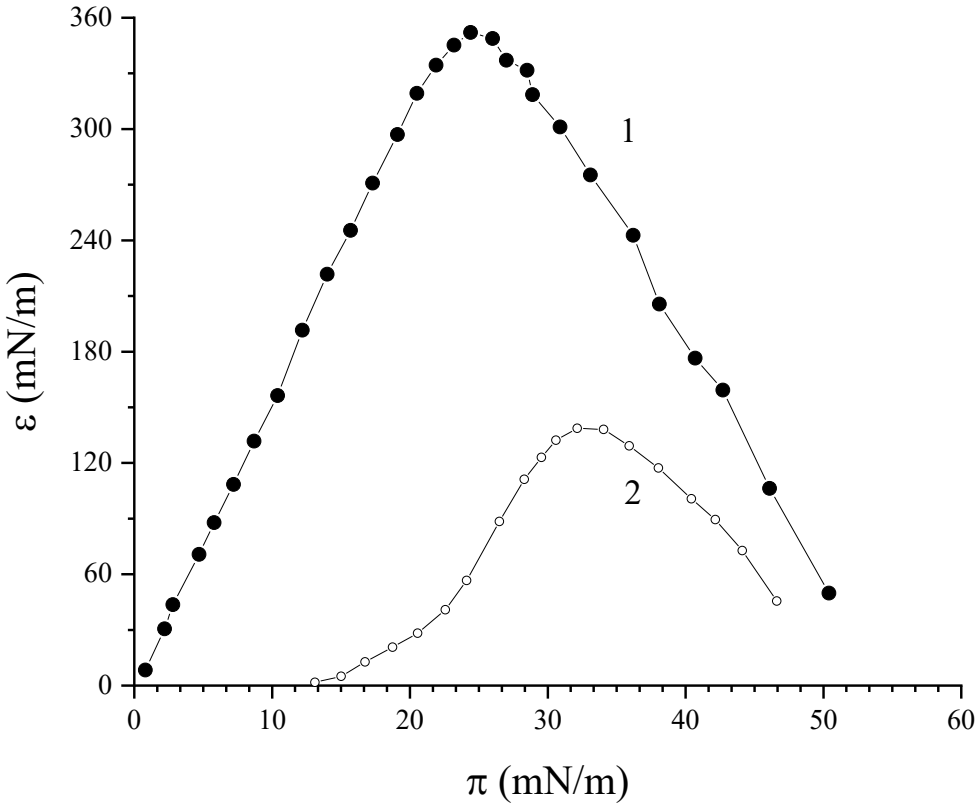

Figure 88. Dependence of dynamic surface elasticity on surface pressure for a film of fullerene C_{60} (1) and NTC_{60} (2).

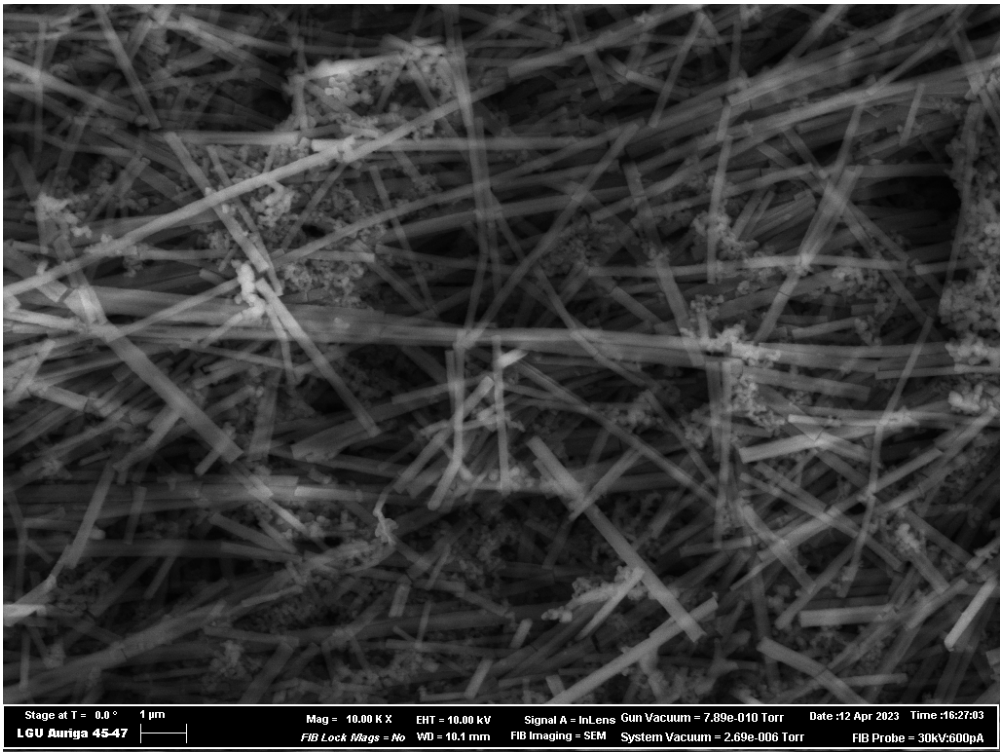

Figure 89. SEM image of the HTC_{60} film for section 2 of the compression isotherm.

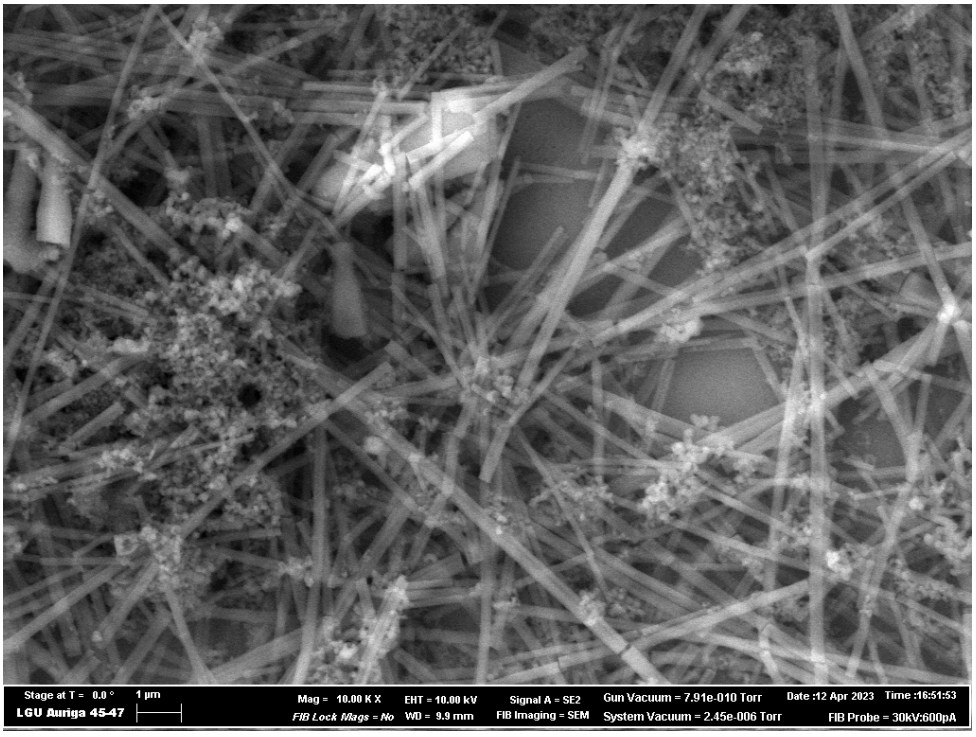

Figure 90. SEM image of the HTC_{60} film for section 3 of the compression isotherm.

Conclusion

This work shows that fullerenol $C_{60}(OH)_{30}$ molecules form a macroscopically homogeneous adsorption layer with high dynamic surface elasticity up to 170 mN/m at the solution-air interface. At the same time, the surface activity of $C_{60}(OH)_{30}$ is low. It reduces surface tension at low concentrations (<0.3 g/L) to only 71 mN/m. Despite the relatively low molecular weight of fullerenol. $C_{60}(OH)_{30}$, the surface properties of its solutions are more reminiscent of the properties of dispersions of solid nanoparticles than of surfactant solutions, and are very sensitive to small mechanical disturbances of the surface. The $C_{60}(OH)_30$ adsorption layer is characterized by a nonlinear response even to small amplitude fluctuations in the surface area (3 mm (2.5%)). These vibrations can lead to the destruction of the continuous structure of the layer and the formation of cracks between dense areas. AFM shows that the adsorption layer at the microlevel is heterogeneous and contains surface microaggregates consisting of two to three layers of fullerenol molecules. Surface $C_{60}(OH)_{30}$ aggregates are not adsorbed from the bulk phase, but are formed in the surface layer as a result of structural rearrangements of adsorbed molecules. The slow adsorption of fullerenols is determined by the electrostatic adsorption barrier.

Fullerenol $C_{60}(OH)_{20}$ also forms a macroscopically homogeneous layer at the solution-air interface. Small changes in surface tension (about 5 mN/m) are accompanied by a strong increase in the dynamic elasticity of the surface up to 300 mN/m. The surface elasticity of $C_{60}(OH)_{20}$ solutions turns out to be significantly higher than that of $C_{60}(OH)_{30}$ solutions. Adsorption of $C_{60}(OH)_{20}$ occurs faster due to the lower charge of the molecules and, therefore, the lower adsorption barrier. The adsorption layer of $C_{60}(OH)_{20}$ is more fragile than the layer of $C_{60}(OH)_{30}$. Compressing the surface by a factor of 2 leads to a decrease in dynamic surface elasticity by approximately 25% in the first case, while in the second case the surface elasticity increases after compression. Continuous fluctuations in surface area also lead to a decrease in the elasticity of the surface of $C_{60}(OH)_{20}$ solutions as a result of partial destruction of the adsorption layer. The adsorption layer of $C_{60}(OH)_{20}$ is heterogeneous on a microscopic scale and contains surface aggregates.

The surface activity of another C_{60} fullerene derivative, carboxyfullerene $C_{60}(C(COOH)_2)_3$, is close to the results for conventional surfactants and significantly exceeds the surface activity of fullerenols. Adsorption of carboxyfullerene occurs much faster, and the

kinetic dependences of surface properties do not have an induction period. The dynamic surface elasticity of carboxyfullerene solutions changes within several hours after surface formation, while the surface tension remains almost unchanged after an initial rapid decrease. The adsorption layer of carboxyfullerene is less fragile than the adsorption layers of fullerenols, and its properties change to a lesser extent under external mechanical influences. BAM images of adsorption layers of carboxyfullerene indicate their liquid-like nature. The adsorption layer $C_{60}(C(COOH)_2)_3$ contains numerous surface aggregates, the size and number of which increase during the adsorption process.

The properties of deposited films of unmodified C_{60} fullerene at the water-air interface indicate its strong adhesion to water. The layers can withstand high surface pressures of up to 70 mN/m. In this case, the dynamic elasticity of the films reaches very high values (about 370 mN/m) at surface pressures close to 25 mN/m. The thickness of the deposited layer of C_{60} fullerene varies from point to point. According to AFM data, bilayers or trilayers are primarily formed at low surface pressure, but as surface pressure increases, surface aggregates up to 100 nm in size in the Z direction can form.

The dependences of dynamic elasticity on surface pressure of mixed deposited C_{60} films with amphiphilic polymers PVP and PNIPAM have two local maxima and can be divided into two parts, for which the surface elasticity is determined by the polymer or fullerene, respectively. The polymer has little effect on surface elasticity at high surface pressures (> 50 mN/m).

The properties of deposited C_{60} and C_{60}/polymer films at high surface pressure are due to the strong adhesion of the layers to water. It can be assumed that this is caused by hydroxylation of the fullerene layer adjacent to water, as in the case of hydroxylation of fullerene aggregates in the bulk phase of water.

The properties of deposited layers of fullerene nanotubes on an aqueous surface are very different from the properties of fullerene deposited from a solution in toluene. In the first case, the dynamic surface elasticity turns out to be several times lower. A plateau region appears on the compression isotherms, corresponding to a two-dimensional phase transition.

References

1. Kang H. et al. From Fullerene-Polymer to All-Polymer Solar Cells: The Importance of Molecular Packing, Orientation, and Morphology Control // Acc Chem Res. 2016. Vol. 49, № 11. P. 2424–2434.
2. Dini D., Calvete M.J.F., Hanack M. Nonlinear Optical Materials for the Smart Filtering of Optical Radiation // Chem Rev. 2016. Vol. 116, № 22. P. 13043–13233.
3. Richter M. et al. Carbon Photodetectors: The Versatility of Carbon Allotropes // Adv Energy Mater. 2017. Vol. 7, № 10.
4. Yin H. et al. The recent advances in C60 micro/nanostructures and their optoelectronic applications // Organic Electronics. Elsevier B.V., 2021. Vol. 93.
5. Masuhara A. et al. Fullerene fine crystals with unique shapes and controlled size // Jpn J Appl Phys. 2009. Vol. 48, № 5. P. 0502061–0502063.
6. Akada M. et al. Superconducting phase sequence in Rx C60 fullerides (R=Sm and Yb) // Phys Rev B Condens Matter Mater Phys. 2006. Vol. 73, № 9.
7. Matz D.L. et al. Deciphering the metal-C60 interface in optoelectronic devices: Evidence for C60 reduction by vapor deposited Al // ACS Appl Mater Interfaces. 2013. Vol. 5, № 13. P. 6001–6008.
8. Roy J.K., Kar S., Leszczynski J. Optoelectronic properties of C60 and C70 fullerene derivatives: Designing and evaluating novel candidates for efficient P3HT polymer solar cells // Materials. MDPI AG, 2019. Vol. 12, № 14.
9. Zhu R. et al. Experimental research on C60 concrete strength evolution under different curing conditions // E3S Web of Conferences. EDP Sciences, 2020. Vol. 198.
10. Sekkal W., Zaoui A. Novel properties of nano-engineered cementitious materials with fullerene buckyballs // Cem Concr Compos. Elsevier Ltd, 2021. Vol. 118.
11. Zhao W. et al. Experimental study on the influence of mixing time on concrete performance under different mixing modes // Science and Engineering of Composite Materials. De Gruyter Open Ltd, 2021. Vol. 28, № 1. P. 638–651.
12. Lundin J.G. et al. Self-cleaning photocatalytic polyurethane coatings containing modified C 60 fullerene additives // Coatings. MDPI AG, 2014. Vol. 4, № 3. P. 614–629.
13. Liu D. et al. Comparative tribological and corrosion resistance properties of epoxy composite coatings reinforced with functionalized fullerene C60 and graphene // Surf Coat Technol. Elsevier B.V., 2016. Vol. 286. P. 354–364.
14. Xing M., Wang R., Yu J. Application of fullerene C60 nano-oil for performance enhancement of domestic refrigerator compressors // International Journal of Refrigeration. Elsevier Ltd, 2014. Vol. 40. P. 398–403.

15. Huang J.S. et al. Study on Dispersion Stability and Friction Characteristics of C60 Nanomicrosphere Lubricating Additives for Improving Cutting Conditions in Manufacturing Process // Math Probl Eng. Hindawi Limited, 2021. Vol. 2021.

16. Pikhurov D. v., Zuev V. v. The study of mechanical and tribological performance of fulleroid materials filled PA 6 composites // Lubricants. MDPI AG, 2016. Vol. 4, № 2.

17. Zhang M. et al. C60 as fine fillers to improve poly(phenylene sulfide) electrical conductivity and mechanical property // Sci Rep. Nature Publishing Group, 2017. Vol. 7, № 1.

18. Alekseeva O. v., Bagrovskaya N.A., Noskov A. v. Effect of C60 filling on structure and properties of composite films based on polystyrene // Arabian Journal of Chemistry. Elsevier B.V., 2018. Vol. 11, № 7. P. 1160–1164.

19. Vinogradova L.V. et al. C60 fullerene-containing polymer stars in mixed matrix membranes // Nanosystems: Physics, Chemistry, Mathematics. ITMO University, 2016. P. 118–124.

20. Goodarzi S. et al. Fullerene: biomedical engineers get to revisit an old friend // Materials Today. 2017. Vol. 20, № 8. P. 460–480.

21. Castro E. et al. Fullerenes in biology and medicine // J Mater Chem B. 2017. Vol. 5, № 32. P. 6523–6535.

22. Bosi S. et al. Fullerene derivatives: An attractive tool for biological applications // Eur J Med Chem. 2003. Vol. 38, № 11–12. P. 913–923.

23. Heredia D.A. et al. Fullerene C60 derivatives as antimicrobial photodynamic agents // Journal of Photochemistry and Photobiology C: Photochemistry Reviews. Elsevier B.V., 2022. Vol. 51.

24. Aoshima H et al. Antimicrobial activity of fullerenes and their hydroxylated derivatives // Biocontrol Sci. 2009. Vol. 14, № 2. P. 69–72.

25. Hou W. et al. Application of Fullerenes as Photosensitizers for Antimicrobial Photodynamic Inactivation: A Review // Frontiers in Microbiology. Frontiers Media S.A., 2022. Vol. 13.

26. Skivka L.M. et al. C60 fullerene and its nanocomplexes with anticancer drugs modulate circulating phagocyte functions and dramatically increase ROS generation in transformed monocytes // Cancer Nanotechnol. BioMed Central Ltd., 2018. Vol. 9, № 1.

27. Prylutska S. et al. C60 Fullerene as Synergistic Agent in Tumor-Inhibitory Doxorubicin Treatment // Drugs in R and D. Springer International Publishing, 2014. Vol. 14, № 4. P. 333–340.

28. Ye L. et al. Antitumor activity and potential mechanism of novel fullerene derivative nanoparticles // Molecules. MDPI AG, 2021. Vol. 26, № 11.

29. Conyers J.L. Biomedical Applications of Functionalized Nanomaterials // Biomedical Applications of Functionalized Nanomaterials. 2018. P. 261–275.

30. Grebinyk A. et al. C60 fullerene as an effective nanoplatform of alkaloid berberine delivery into leukemic cells // Pharmaceutics. MDPI AG, 2019. Vol. 11, № 11.

31. Giannopoulos G.I. Fullerene Derivatives for Drug Delivery against COVID-19: A Molecular Dynamics Investigation of Dendro[60]fullerene as Nanocarrier of Molnupiravir // Nanomaterials. MDPI, 2022. Vol. 12, № 15.

32. Montellano A. et al. Fullerene C60 as a multifunctional system for drug and gene delivery // Nanoscale. 2011. Vol. 3, № 10. P. 4035–4041.

33. Felder D. et al. Synthesis of amphiphilic fullerene derivatives and their incorporation in Langmuir and Langmuir-Blodgett films // Helv Chim Acta. 2002. Vol. 85, № 1. P. 288–319.

34. Obeng Y.S., Bard A.J. Langmuir Films of C60 at the Air-Water Interface // J Am Chem Soc. 1991. Vol. 113, № 16. P. 6279–6280.

35. Kolker A.M., Borovkov N.Y. Three-dimensional aggregation of fullerene C60 at the air-water interface // Colloids Surf A Physicochem Eng Asp. Elsevier B.V., 2012. Vol. 414. P. 433–439.

36. Guldi D.M., Prato M. Excited-state properties of C60 fullerene derivatives // Acc Chem Res. 2000. Vol. 33, № 10. P. 695–703.

37. Semenov K.N. et al. Solubility of light fullerenes in organic solvents // J Chem Eng Data. 2010. Vol. 55, № 1. P. 13–36.

38. Milliken J. et al. Incorporation of buckminsterfullerene (C60) in Langmuir Blodgett films // Chemistry of Materials . 1992. Vol. 4, № 2. P. 252–254.

39. Jonas U. et al. Synthesis of a Fullerene[60] Cryptate and Systematic Langmuir-Blodgett and Thin-Film Investigations of Amphiphilic Fullerene Derivatives // Chemistry a European Journal. 1995. Vol. 1, № 4. P. 243–251.

40. Semenov K.N. et al. Fullerenols: Physicochemical properties and applications // Progress in Solid State Chemistry. Elsevier Ltd, 2016. Vol. 44, № 2. P. 59–74.

41. Wang Z., Yang S. Effects of fullerenes on phospholipid membranes: A langmuir monolayer study // ChemPhysChem. Wiley-VCH Verlag, 2009. Vol. 10, № 13. P. 2284–2289.

42. Miyazawa K. et al. C60 Nanowhiskers Formed by the Liquid–liquid Interfacial Precipitation Method // J Mater Res. 2002. Vol. 17, № 1. P. 83–88.

43. Ringor C.L., Miyazawa K. Synthesis of C60 nanotubes by liquid–liquid interfacial precipitation method: Influence of solvent ratio, growth temperature, and light illumination // Diam Relat Mater. 2008. Vol. 17, № 4–5. P. 529–534.

44. Kroto H.W. et al. C60: Buckminsterfullerene // Nature. 1985. Vol. 318. P. 162–163.

45. Taylor R. et al. Isolation, Separation and Characterisation of the Fullerenes C60 and C70: The Third Form of Carbon // J. Chem. Soc. Chem. Commun. 1990. № 20. P. 1423–1425.

46. Hawkins J.M. et al. Crystal Structure of Osmylated C60: Confirmation of the Soccer Ball Framework // Science (1979). 1991. Vol. 252. P. 312.

47. Haddon R.C., Brus L.E., Raghavachari K. Rehybridization and π-orbital alignment: the key to the existence of spheroidal carbon clusters // Chem. Phys. Lett. 1986. Vol. 131. P. 165.

48. Kolodziejski W., Klinowski J. 13C → 1H → 13C cross-polarization NMR in toluene-solvated fullerene-70 // Chem Phys Lett. 1995. Vol. 247, № 4–6. P. 507–509.

49. Sivaraman N. et al. Solubility of C70/ in Organic Solvents // Fullerene Science and Technology. 1994. Vol. 2, № 3. P. 233–246.

50. Ruoff R.S. et al. Solubility of fullerene (C60) in a variety of solvents // J Phys Chem. 1993. Vol. 97, № 13. P. 3379–3383.

51. Huang Y.-Y. et al. Functionalized Fullerenes in Photodynamic Therapy // J Biomed Nanotechnol. 2014. Vol. 10, № 9. P. 1918–1936.

52. Hebard A.F. et al. Superconductivity at 18 K in potassium-doped C60 // Nature. 1991. Vol. 350, № 6319. P. 600–601.

53. Saunders M. et al. Incorporation of helium, neon, argon, krypton, and xenon into fullerenes using high pressure // J Am Chem Soc. 1994. Vol. 116, № 5. P. 2193–2194.

54. Schick G. et al. Opening and Closure of the Fullerene Cage incis-Bisimino Adducts of C60: The Influence of the Addition Pattern and the Addend // Chemistry - A European Journal. 1996. Vol. 2, № 8. P. 935–943.

55. Hirsch A., Nuber B. Nitrogen Heterofullerenes // Acc Chem Res. 1999. Vol. 32, № 9. P. 795–804.

56. Iijima S. Helical microtubules of graphitic carbon // Nature. 1991. Vol. 354, № 6348. P. 56–58.

57. Ebbesen T.W., Ajayan P.M. Large-scale synthesis of carbon nanotubes // Nature. 1992. Vol. 358, № 6383. P. 220–222.

58. Wang N. et al. Single-walled 4 Å carbon nanotube arrays // Nature. 2000. Vol. 408, № 6808. P. 50–51.

59. Ding R.G. et al. Recent Advances in the Preparation and Utilization of Carbon Nanotubes for Hydrogen Storage // J Nanosci Nanotechnol. 2001. Vol. 1, № 1. P. 7–29.

60. Van Oss C.J., Chaudhury M.K., Good R.J. Interfacial Lifshitz-van der Waals and polar interactions in macroscopic systems // Chem Rev. 1988. Vol. 88, № 6. P. 927–941.

61. Andrievsky G.V. et al. Comparative analysis of two aqueous-colloidal solutions of C60 fullerene with help of FTIR reflectance and UV–Vis spectroscopy // Chem Phys Lett. 2002. Vol. 364, № 1–2. P. 8–17.

62. Ma X., Bouchard D. Formation of Aqueous Suspensions of Fullerenes // Environ Sci Technol. 2009. Vol. 43, № 2. P. 330–336.

63. Duncan L.K., Jinschek J.R., Vikesland P.J. C60 Colloid Formation in Aqueous Systems: Effects of Preparation Method on Size, Structure, and Surface Charge // Environ Sci Technol. 2008. Vol. 42, № 1. P. 173–178.

64. Prilutski Yu.I. et al. Theoretical predictions and experimental studies of self-organized C60 nanoparticles in water solution and on the support // The European Physical Journal D. 1999. Vol. 9, № 1. P. 341–343.

65. Andrievsky G.V. et al. Studies of aqueous colloidal solutions of fullerene C60 by electron microscopy // Chem Phys Lett. 1999. Vol. 300, № 3–4. P. 392–396.

66. Ma X., Wigington B., Bouchard D. Fullerene C60: Surface Energy and Interfacial Interactions in Aqueous Systems // Langmuir. 2010. Vol. 26, № 14. P. 11886–11893.

67. Labille J. et al. Hydration and Dispersion of C60 in Aqueous Systems: The Nature of Water−Fullerene Interactions // Langmuir. 2009. Vol. 25, № 19. P. 11232–11235.

68. Mchedlov-Petrossyan N.O. Fullerenes in Liquid Media: An Unsettling Intrusion into the Solution Chemistry // Chem Rev. 2013. Vol. 113, № 7. P. 5149–5193.

69. Sayes C.M. et al. The Differential Cytotoxicity of Water-Soluble Fullerenes // Nano Lett. 2004. Vol. 4, № 10. P. 1881–1887.

70. Torres V.M. et al. Fullerenol C60(OH)24 prevents doxorubicin-induced acute cardiotoxicity in rats // Pharmacological Reports. 2010. Vol. 62, № 4. P. 707–718.

71. Zhang J. et al. Synergistic effect of phosphite with fullerene C60 and fullerenol C60(OH)24 as antioxidants in polypropylene // Chinese Journal of Polymer Science. 2014. Vol. 32, № 10. P. 1357–1362.

72. Injac R. et al. Potential hepatoprotective effects of fullerenol C60(OH)24 in doxorubicin-induced hepatotoxicity in rats with mammary carcinomas // Biomaterials. 2008. Vol. 29, № 24–25. P. 3451–3460.

73. Espinasse B., Hotze E.M., Wiesner M.R. Transport and Retention of Colloidal Aggregates of C_{60} in Porous Media: Effects of Organic Macromolecules, Ionic Composition, and Preparation Method // Environ Sci Technol. 2007. Vol. 41, № 21. P. 7396–7402.

74. Brettreich M., Hirsch A. A highly water-soluble dendro[60]fullerene // Tetrahedron Lett. 1998. Vol. 39, № 18. P. 2731–2734.

75. Guldi D.M., Hungerbühler H., Asmus K.-D. Radiolytic Reduction of a Water-Soluble Fullerene Cluster // J Phys Chem A. 1997. Vol. 101, № 10. P. 1783–1786.

76. Andersson T. et al. NMR and UV–VIS Investigation of water-soluble fullerene-60–γ-cyclodextrin complex // J. Chem. Soc., Perkin Trans. 2. 1994. № 5. P. 1097–1101.

77. Guldi D.M., Hungerbuehler H., Asmus K.-D. Redox and Excitation Studies with C60-Substituted Malonic Acid Diethyl Esters // J Phys Chem. 1995. Vol. 99, № 23. P. 9380–9385.

78. Andersson T. et al. C60 embedded in γ-cyclodextrin: a water-soluble fullerene // J. Chem. Soc., Chem. Commun. 1992. № 8. P. 604–606.

79. Yoshida Z. et al. Molecular Recognition of C60 withγ-Cyclodextrin // Angewandte Chemie International Edition in English. 1994. Vol. 33, № 1516. P. 1597–1599.

80. Beeby A., Eastoe J., Heenan R.K. Solubilisation of C60 in aqueous micellar solution // J Chem Soc Chem Commun. 1994. № 2. P. 173.

81. Eastoe J. et al. Structure and photophysics in C60-micellar solutions // Chem Phys Lett. 1995. Vol. 245, № 6. P. 571–577.

82. Guldi D.M. et al. Excitation of C60, solubilized in water by triton X-100 and γ-cyclodextrin, and subsequent charge separation via reductive quenching // Chem Phys Lett. 1994. Vol. 223, № 5–6. P. 511–516.

83. Kanazawa K. et al. An NMR Study of the Buckminster Fullerene Complex with Cyclodextrin in Aqueous Solution // Fullerene Science and Technology. 1994. Vol. 2, № 2. P. 189–194.

84. Priyadarsini I.K., Mohan H., Mittal P.J. Characterization and Properties of γ-Cyclodextrin-C_{60} Complex In Aqueous Solution // Fullerene Science and Technology. 1995. Vol. 3, № 5. P. 479–493.

85. Barcza Á.B. et al. The Interaction of Buckminsterfullerene with Gamma-Cyclodextrin // Fullerene Science and Technology. 1997. Vol. 5, № 2. P. 311–323.

86. Ala-Kleme T. et al. Blue and red photoluminescence of bicapped [60]fullerene-γ-cyclodextrin complex in aqueous solutions // Anal Chim Acta. 2002. Vol. 472, № 1–2. P. 83–87.

87. Greisch J.-F. et al. Mass spectrometric study of the ionized C60: (γ-Cyclodextrin)2 inclusion complex by collision induced dissociation // Journal of Mass Spectrometry. 2008. Vol. 43, № 2. P. 242–250.

88. Murthy C.N. Nanoencapsulation of Fullerenes in Organic Structures with Nonpolar Cavities // Hyperfine Interact. 2005. Vol. 160, № 1–4. P. 189–192.

89. Komatsu K. et al. Aqueous solubilization of crystalline fullerenes by supramolecular complexation with γ-cyclodextrin and sulfocalix[8]arene under mechanochemical high-speed vibration milling // J Chem Soc Perkin 1. 1999. № 20. P. 2963–2966.

90. Wang H.M., Wenz G. Molecular solubilization of fullerene C_{60} in water by γ-cyclodextrin thioethers // Beilstein Journal of Organic Chemistry. 2012. Vol. 8. P. 1644–1651.

91. Guldi D.M. Electron transfer to buckminster-fullerenes and functionalized fullerene derivatives in aqueous and protic media, as studied by radiolytic techniques // Research on Chemical Intermediates. 1997. Vol. 23, № 7. P. 653–673.

92. Ikeda A. et al. Water-soluble [60]fullerene–cationic homooxacalix[3]arene complex which is applicable to the photocleavage of DNA // Chemical Communications. 1999. № 15. P. 1403–1404.

93. Hungerbuehler H., Guldi D.M., Asmus K.D. Incorporation of C60 into artificial lipid membranes // J Am Chem Soc. 1993. Vol. 115, № 8. P. 3386–3387.

94. Bensasson R. V. et al. C60 in Model Biological Systems. A Visible-UV Absorption Study of Solvent-Dependent Parameters and Solute Aggregation // J Phys Chem. 1994. Vol. 98, № 13. P. 3492–3500.

95. Metanawin T. et al. Cytotoxicity and photocytotoxicity of structure-defined water-soluble C_{60} / micelle supramolecular nanoparticles // Nanotechnology. 2011. Vol. 22, № 23. P. 235604.

96. Lee J., Kim J.-H. Effect of Encapsulating Agents on Dispersion Status and Photochemical Reactivity of C_{60} in the Aqueous Phase // Environ Sci Technol. 2008. Vol. 42, № 5. P. 1552–1557.

97. Torres V.M. et al. Solubilization of fullerene C60 in micellar solutions of different solubilizers // Colloids Surf B Biointerfaces. 2011. Vol. 82, № 1. P. 46–53.

98. Zhang W., Honeychuck R. V., Hussam A. Buckminsterfullerene-Containing Microemulsions // Langmuir. 1996. Vol. 12, № 5. P. 1402–1403.

99. Šaponjić Z. V., Nedeljković J.M., Dimitrijević N.M. Charge-transfer reactions of C60 in surfactant-based complex fluid media // Chem Phys Lett. 1997. Vol. 277, № 4. P. 335–339.

100. Guldi D.M. Electron Transfer Studies in C_{78} (C_{2v} ‘) , C_{76} (D_2), C_{70} (D_{5h}), and C_{60} (I_h) Surfactant Aqueous Solutions // J Phys Chem B. 1997. Vol. 101, № 46. P. 9600–9605.

101. Matarredona O. et al. Dispersion of Single-Walled Carbon Nanotubes in Aqueous Solutions of the Anionic Surfactant NaDDBS // J Phys Chem B. 2003. Vol. 107, № 48. P. 13357–13367.

102. Marković Z. et al. Comparative study on modification of single wall carbon nanotubes by sodium dodecylbenzene sulfonate and melamine sulfonate superplasticiser // Appl Surf Sci. 2009. Vol. 255, № 12. P. 6359–6366.

103. Shinohara N. et al. In vitro and in vivo genotoxicity tests on fullerene C60 nanoparticles // Toxicol Lett. 2009. Vol. 191, № 2–3. P. 289–296.

104. Litvinova L.S. et al. Physicochemical properties of Water-Soluble Fullerene C60-Carbohydrate Composites // Russian Journal of Applied Chemistry. 2004. Vol. 77, № 3. P. 438–440.

105. Tabata Y., Murakami Y., Ikada Y. Photodynamic Effect of Polyethylene Glycol-modified Fullerene on Tumor // Japanese Journal of Cancer Research. 1997. Vol. 88, № 11. P. 1108–1116.

106. Yamakoshi Y.N. et al. Solubilization of fullerenes into water with polyvinylpyrrolidone applicable to biological tests // J Chem Soc Chem Commun. 1994. № 4. P. 517.

107. Ungurenasu C., Airinei A. Highly Stable C60/Poly(vinylpyrrolidone) Charge-Transfer Complexes Afford New Predictions for Biological Applications of Underivatized Fullerenes // J Med Chem. 2000. Vol. 43, № 16. P. 3186–3188.

108. Li Q. et al. Antimicrobial nanomaterials for water disinfection and microbial control: Potential applications and implications // Water Research. Elsevier Ltd, 2008. Vol. 42, № 18. P. 4591–4602.

109. Benn T.M., Westerhoff P., Herckes P. Detection of fullerenes (C60 and C70) in commercial cosmetics // Environmental Pollution. 2011. Vol. 159, № 5. P. 1334–1342.

110. Datta K., Mukherjee A.K. Aggregation of [70]fullerene in presence of acetonitrile: A chemical kinetic experiment // J Chem Phys. 2006. Vol. 124, № 14. P. 144509.

111. Yevlampieva N.P. et al. Molecular properties of C60 fullerene complexes with cycle-containing polymers in solutions // Physics of the Solid State. 2002. Vol. 44, № 3. P. 563–566.

112. Podol'skii I.Ya. et al. Fullerene C60 complexed with poly(N-vinyl-pyrrolidone) prevents the disturbance of long-term memory consolidation // Physics of the Solid State. 2002. Vol. 44, № 3. P. 578–580.

113. Wang P. et al. Preparation and deposition of stable monolayers of fullerene derivatives // J Mater Chem. 1997. Vol. 7, № 12. P. 2397–2400.

114. Back R., Lennox R.B. Fullerenes, C60 and C70 at the air-water interface // J Phys Chem. 1992. Vol. 96, № 20. P. 8149–8152.

115. Sha Shiratori S., Shimizu M., Ikezaki K. Molecular sifter using space controlled Langmuir–Blodgett films by fullerene molecules // Thin Solid Films. 1998. Vol. 327–329. P. 655–658.

116. Effing J. et al. C60 and C70 in a Basket?– Investigations of Mono- and Multilayers from Azacrown Compounds and Fullerenes // Angewandte Chemie International Edition in English. 1992. Vol. 31, № 12. P. 1599–1602.

117. Dei L. et al. Langmuir Films of p-tert-Butylcalix[8]arene. Conformations at the Water−Air Interface and Complexation of Fullerene C60 // Langmuir. 1998. Vol. 14, № 15. P. 4143–4147.

118. Guldi D.M. et al. Formation, Characterization, and Properties of Nanostructured [Ru(bpy)3]2+-C60 Langmuir−Blodgett Films in Situ at the Air−Water Interface and ex Situ on Substrates // Langmuir. 2000. Vol. 16, № 3. P. 1311–1318.

119. Cardullo F. et al. Stable Langmuir and Langmuir−Blodgett Films of Fullerene−Glycodendron Conjugates // Langmuir. 1998. Vol. 14, № 8. P. 1955–1959.

120. Nierengarten J.-F. et al. Amphiphilic Diblock Dendrimers: Synthesis and Incorporation in Langmuir and Langmuir−Blodgett Films // J Am Chem Soc. 2001. Vol. 123, № 40. P. 9743–9748.

121. Uchida K. et al. Dependence of the dispersion behavior of [60]fullerene in aqueous media on the chain length of poly(N-isopropylacrylamide) as a dispersing agent // Colloid Polym Sci. 2011. Vol. 289, № 1. P. 73–78.

122. Yoshida R. et al. Modulating the phase transition temperature and thermosensitivity in N-isopropylacrylamide copolymer gels // J Biomater Sci Polym Ed. 1995. Vol. 6, № 6. P. 585–598.

123. Yoshida R. et al. Comb-type grafted hydrogels with rapid deswelling response to temperature changes // Nature. 1995. Vol. 374, № 6519. P. 240–242.

124. Xia Y. et al. Thermal Response of Narrow-Disperse Poly(N-isopropylacrylamide) Prepared by Atom Transfer Radical Polymerization // Macromolecules. 2005. Vol. 38, № 14. P. 5937–5943.

125. Xia Y., Burke N.A.D., Stöver H.D.H. End Group Effect on the Thermal Response of Narrow-Disperse Poly(N-isopropylacrylamide) Prepared by Atom Transfer Radical Polymerization // Macromolecules. 2006. Vol. 39, № 6. P. 2275–2283.

126. Uchida K., Tamura A., Yajima H. Effect of the polymer chain length of poly(N - isopropylacrylamide) on the temperature-responsive phase transition behavior of its conjugates with [60]fullerene // Biointerphases. 2010. Vol. 5, № 1. P. 17–21.

127. Sushko M.L., Tenhu H., Klenin S.I. Static and dynamic light scattering study of strong intermolecular interactions in aqueous solutions of PVP/C60 complexes // Polymer (Guildf). 2002. Vol. 43, № 9. P. 2769–2775.

128. Behera M., Ram S. Mechanism of Solubilizing Fullerene C60 in Presence of Poly(Vinyl pyrrolidone) Molecules in Water // Fullerenes, Nanotubes and Carbon Nanostructures. 2015. Vol. 23, № 10. P. 906–916.

129. Tarassova E. et al. Structure of poly(vinyl pyrrolidone) – C70 complexes in aqueous solutions // Polymer (Guildf). 2007. Vol. 48, № 15. P. 4503–4510.

130. Chaban V. V., Fileti E.E. Which fullerenols are water soluble? Systematic atomistic investigation // New Journal of Chemistry. Royal Society of Chemistry, 2016. Vol. 41, № 1. P. 184–189.

131. Semenov K.N., Charykov N.A., Keskinov V.N. Fullerenol synthesis and identification. properties of the fullerenol water solutions // J Chem Eng Data. 2011. Vol. 56, № 2. P. 230–239.

132. Tsai M.-C., Chen Y.H., Chiang L.Y. Polyhydroxylated C60, Fullerenol, a Novel Free-radical Trapper, Prevented Hydrogen Peroxide- and Cumene Hydroperoxide-elicited Changes in Rat Hippocampus In-vitro // Journal of Pharmacy and Pharmacology. 2011. Vol. 49, № 4. P. 438–445.

133. Djordjevic A. et al. Review of Synthesis and Antioxidant Potential of Fullerenol Nanoparticles // J Nanomater. 2015. Vol. 2015. P. 1–15.

134. Krokosz A. et al. Carbon nanoparticles as possible radioprotectors in biological systems // Radiation Physics and Chemistry. 2016. Vol. 128. P. 143–150.

135. Dawid A., Górny K., Gburski Z. The influence of distribution of hydroxyl groups on vibrational spectra of fullerenol C60(OH)24 isomers: DFT study // Spectrochim Acta A Mol Biomol Spectrosc. Elsevier B.V., 2015. Vol. 136, № PC. P. 1993–1997.

136. Semenov K.N. et al. Electrochemical properties of aqueous solutions of fullerenol-d // Russian Journal of Applied Chemistry. 2011. Vol. 84, № 1. P. 79–83.

137. Wolff D.J. et al. Inhibition of nitric oxide synthase isoforms by tris-malonyl-C60-fullerene adducts // Arch Biochem Biophys. Academic Press Inc., 2000. Vol. 378, № 2. P. 216–223.

138. Sumizawa T., Igisu H. Suppression of acrylamide toxicity by carboxyfullerene in human neuroblastoma cells in vitro // Arch Toxicol. 2009. Vol. 83, № 9. P. 817–824.

139. Cui J. et al. Protective effects of carboxyfullerene in irradiated cells and BALB/c mice. // Free Radic Res. 2013. Vol. 47, № 4. P. 301–308.

140. Liu Q. et al. C70-carboxyfullerenes as efficient antioxidants to protect cells against oxidative-induced stress // ACS Appl Mater Interfaces. 2013. Vol. 5, № 21. P. 11101–11107.

141. Dugan L.L. et al. Fullerene-based antioxidants and neurodegenerative disorders.

142. Takada H. et al. Antioxidant activity of supramolecular water-soluble fullerenes evaluated by β-carotene bleaching assay // Biosci Biotechnol Biochem. 2006. Vol. 70, № 12. P. 3088–3093.

143. Beuerle F. et al. Cytoprotective activities of water-soluble fullerenes in zebrafish models // J Exp Nanosci. 2007. Vol. 2, № 3. P. 147–170.

144. Penkova A. v. et al. Novel mixed-matrix membranes based on polyvinyl alcohol modified by carboxyfullerene for pervaporation dehydration // Sep Purif Technol. Elsevier B.V., 2018. Vol. 204. P. 1–12.

145. Tsao N. et al. Inhibition of group A streptococcus infection by carboxyfullerene // Antimicrob Agents Chemother. 2001. Vol. 45, № 6. P. 1788–1793.

146. Wang Y.H. et al. Inhibition of middle cerebral artery occlusion-induced focal cerebral ischemia by carboxyfullerene // J Drug Deliv Sci Technol. Editions de Sante, 2004. Vol. 14, № 1. P. 45–49.

147. Lin A.M.Y. et al. Differential effects of carboxyfullerene on MPP+/MPTP-induced neurotoxicity // Neurochem Int. Elsevier Ltd, 2004. Vol. 44, № 2. P. 99–105.

148. Fumelli C. et al. Carboxyfullerenes Protect Human Keratinocytes from Ultraviolet-B-Induced Apoptosis.

149. Manyakina O.S. et al. Physico-chemical properties of the water-soluble C70-tris-malonic solutions // J Mol Liq. 2015. Vol. 211. P. 487–493.

150. Semenov K.N. et al. Mass transport properties of water soluble light fullerene tris-malonate C60[=C(COOH)2]3 in aqueous solutions // Nanosystems: Physics, Chemistry, Mathematics. 2015. P. 435–441.

151. Semenov K.N. et al. Dependence of the dimension of the associates of water-soluble tris-malonate of light fullerene C60[=C(COOH)2]3 in water solutions at 25 °C // Nanosystems: Physics, Chemistry, Mathematics. 2015. P. 294–298.

152. Semenov K.N. et al. Physico-chemical properties of the C60-tris-malonic derivative water solutions // J Mol Liq. 2015. Vol. 201. P. 50–58.

153. Sitharaman B. et al. Nanoscale Aggregation Properties of Neuroprotective Carboxyfullerene (C_3) in Aqueous Solution // Nano Lett. 2004. Vol. 4, № 9. P. 1759–1762.

154. Ageev S. V. et al. Density, speed of sound, viscosity, refractive index, surface tension and solubility of C60[C(COOH)2]3 // J Mol Liq. 2019. Vol. 291. P. 111256.

155. Semenov K.N. et al. Carboxylated fullerenes: Physico-chemical properties and potential applications // Progress in Solid State Chemistry. Elsevier Ltd, 2017. Vol. 47–48. P. 19–36.

156. Noskov B.A. et al. Dynamic surface properties of C60-arginine and C60-L-lysine aqueous solutions // Colloids Surf A Physicochem Eng Asp. Elsevier, 2017. Vol. 529, № March. P. 1–6.

157. Rincón M.E. et al. Electrical and Optical Properties of Fullerenol Langmuir−Blodgett Films Deposited on Polyaniline Substrates // J Phys Chem B. 2003. Vol. 107, № 17. P. 4111–4117.

158. Miyazawa K., Obayashi A., Kuwabara M. C60 Nanowhiskers in a Mixture of Lead Zirconate Titanate Sol-C60 Toluene Solution // Journal of the American Ceramic Society. 2001. Vol. 84, № 12. P. 3037–3039.

159. Tsuchiya T. et al. Nanorods of Endohedral Metallofullerene Derivative // J Am Chem Soc. 2008. Vol. 130, № 2. P. 450–451.

160. Hou Y. et al. Comparative study of pressure-induced polymerization in C60 nanorods and single crystals // Journal of Physics: Condensed Matter. 2007. Vol. 19, № 42. P. 425207.

161. Geng J. et al. Crystal Structure and Growth Mechanism of Unusually Long Fullerene (C60) Nanowires // J Am Chem Soc. 2008. Vol. 130, № 8. P. 2527–2534.

162. Malik S. et al. Creation of 1D [60]fullerene superstructures and its polymerization by γ-ray irradiation // J. Mater. Chem. 2007. Vol. 17, № 23. P. 2454–2458.

163. Ji H.-X. et al. Controllable Preparation of Submicrometer Single-Crystal C60 Rods and Tubes Trough Concentration Depletion at the Surfaces of Seeds // The Journal of Physical Chemistry C. 2007. Vol. 111, № 28. P. 10498–10502.

164. Kobayashi T. et al. Microelectromechanical Systems-Based Electrostatic Field Sensor Using Pb(Zr,Ti)O3 Thin Films // Jpn J Appl Phys. 2008. Vol. 47, № 9. P. 7533–7536.

165. Ji H.-X. et al. Controllable crystalline structure of fullerenenanorods and transport properties of an individual nanorod // J. Mater. Chem. 2008. Vol. 18, № 3. P. 328–332.

166. Liu H. et al. Imaging As-Grown [60]Fullerene Nanotubes by Template Technique // J Am Chem Soc. 2002. Vol. 124, № 45. P. 13370–13371.

167. Miyazawa K., Suga T. Transmission electron microscopy investigation of tubular and capsular needlelike crystals of C_{60} produced by the liquid–liquid interfacial precipitation method // J Mater Res. 2004. Vol. 19, № 11. P. 3145–3148.

168. Miyazawa K. et al. Structural characterization of the fullerene nanotubes prepared by the liquid–liquid interfacial precipitation method // J Mater Res. 2005. Vol. 20, № 3. P. 688–695.

169. Miyazawa K., Ringor C. Platinum chloride deposition into C60 nanotubes // Mater Lett. 2008. Vol. 62, № 3. P. 410–413.

170. Sathish M., Miyazawa K. Size-Tunable Hexagonal Fullerene (C60) Nanosheets at the Liquid−Liquid Interface // J Am Chem Soc. 2007. Vol. 129, № 45. P. 13816–13817.

171. Tachibana M. et al. Photo-assisted growth and polymerization of C60 ‘nano’whiskers // Chem Phys Lett. 2003. Vol. 374, № 3–4. P. 279–285.

172. Kobayashi K., Tachibana M., Kojima K. Photo-assisted growth of C60 nanowhiskers from solution // J Cryst Growth. 2005. Vol. 274, № 3–4. P. 617–621.

173. Miyazawa K. et al. Structural investigation of heat-treated fullerene nanotubes and nanowhiskers // Diam Relat Mater. 2006. Vol. 15, № 4–8. P. 1143–1146.

174. Minato J., Miyazawa K., Suga T. Morphology of C60 nanotubes fabricated by the liquid–liquid interfacial precipitation method // Sci Technol Adv Mater. 2005. Vol. 6, № 3–4. P. 272–277.

175. Akasaka T. et al. Novel Metal-Free Bis-silylation: C60-Sensitized Reaction of Disilirane with Benzonitrile // Org Lett. 1999. Vol. 1, № 10. P. 1509–1512.

176. Wang L. et al. Synthesis of Thin, Rectangular C60 Nanorods Usingm-Xylene as a Shape Controller // Advanced Materials. 2006. Vol. 18, № 14. P. 1883–1888.

177. Gupta V., Scharff P., Miura N. Ultrasound induced growth of C60 fullerites over KBr // Mater Lett. 2006. Vol. 60, № 25–26. P. 3156–3159.

178. Gupta V., Scharff P., Miura N. Synthesis of three-dimensional C60 micro-flowers: A scanning electron microscopy study // Mater Lett. 2006. Vol. 60, № 17–18. P. 2278–2281.

179. Lamparth I., Hirsch A. Water-soluble malonic acid derivatives of C60 with a defined three-dimensional structure // J Chem Soc Chem Commun. 1994. № 14. P. 1727–1728.

180. Miyazawa K. et al. Structural characterization of C60 nanowhiskers formed by the liquid/liquid interfacial precipitation method // Surface and Interface Analysis. 2003. Vol. 35, № 1. P. 117–120.

181. Mahdaoui D. et al. Optimization of the liquid–liquid interfacial precipitation method for the synthesis of C60 nanotubes // Bulletin of Materials Science. 2018. Vol. 41, № 6. P. 165.

182. De Feijter J.A., Benjamins J., Veer F.A. Ellipsometry as a tool to study the adsorption behavior of synthetic and biopolymers at the air–water interface // Biopolymers. 1978. Vol. 17, № 7. P. 1759–1772.

183. Noskov B.A. et al. Dilational surface viscoelasticity of polymer solutions // Adv Colloid Interface Sci. 2003. Vol. 104, № 1–3. P. 245–271.

184. Noskov B.A. et al. Dynamic Surface Properties of Fullerenol Solutions // Langmuir. 2019. Vol. 35, № 10.

185. Campbell R.A. et al. Adsorption of Denaturated Lysozyme at the Air–Water Interface: Structure and Morphology // Langmuir. 2018. Vol. 34, № 17. P. 5020–5029.

186. Yazhgur P.A. et al. Dynamic properties of mixed nanoparticle/surfactant adsorption layers // Soft Matter. 2013. Vol. 9, № 12. P. 3305.

187. Noskov B.A. Protein conformational transitions at the liquid–gas interface as studied by dilational surface rheology // Adv Colloid Interface Sci. 2014. Vol. 206. P. 222–238.

188. Noskov B.A. Fast adsorption at the liquid-gas interface // Adv Colloid Interface Sci. 1996. Vol. 69, № 1–3. P. 63–129.

189. Akentiev A. V. et al. Surface properties of fullerenol C60(OH)20 solutions // J Mol Liq. Elsevier B.V., 2020. Vol. 306.

190. Noskov B.A. et al. Dilational rheology of spread and adsorbed layers of silica nanoparticles at the liquid-gas interface // Colloid Journal. Maik Nauka Publishing / Springer SBM, 2014. Vol. 76, № 2. P. 127–138.

191. van den Tempel M., Lucassen-Reynders E.H. Relaxation processes at fluid interfaces // Adv Colloid Interface Sci. 1983. Vol. 18, № 3–4. P. 281–301.

192. Noskov B.A. et al. Dynamic surface properties of poly(N-isopropylacrylamide) solutions // Langmuir. 2004. Vol. 20, № 22. P. 9669–9676.

193. Akentiev A.V. et al. Dynamic elasticity of films formed by poly(N-isopropylacrylamide) microparticles on a water surface // Colloid Journal. 2017. Vol. 79, № 5.

194. Akentiev A. V. et al. Scanning probe microscopy of adsorption layers of sodium polystyrenesulfonate/dodecyltrimethylammonium bromide complexes // Colloid Journal. 2011. Vol. 73, № 4. P. 437–444.

195. Timoshen K.A. et al. Dynamic surface properties of carboxyfullerene solutions // J Mol Liq. 2023. Vol. 372. P. 121174.

196. Sitharaman B. et al. Nanoscale aggregation properties of neuroprotective carboxyfullerene (C3) in aqueous solution // Nano Lett. 2004. Vol. 4, № 9. P. 1759–1762.

197. Noskov B.A., Timoshen K.A., Bykov A.G. Langmuir layers of fullerene C60 and its mixtures with amphiphilic polymers // J Mol Liq. Elsevier B.V., 2020. Vol. 320. P. 114440.

198. Berzina T.S. et al. Deposition of uniform fullerene films by LB technique // Thin Solid Films. 1995. Vol. 256, № 1–2. P. 186–191.

199. Bykov A.G. et al. Dilational surface elasticity of spread monolayers of polystyrene microparticles // Soft Matter. Royal Society of Chemistry, 2014. Vol. 10, № 34. P. 6499–6505.

200. Bykov A.G. et al. Kinetics of adsorption layer formation in solutions of polyacid/surfactant complexes // Journal of Physical Chemistry C. 2009. Vol. 113, № 14. P. 5664–5671.

201. Bykov A.G. et al. Dilational surface elasticity of monolayers of charged polystyrene nano- and microparticles at liquid/fluid interfaces // Colloids Surf A Physicochem Eng Asp. Elsevier B.V., 2015. Vol. 485. P. 42–48.

202. Noskov B.A., Bykov A.G. Dilational rheology of monolayers of nano- and micropaticles at the liquid-fluid interfaces // Curr Opin Colloid Interface Sci. Elsevier Ltd, 2018. Vol. 37, № May. P. 1–12.

203. Noskov B.A. et al. Dynamic surface properties of solutions of poly(ethylene oxide) and polyethylene glycols // Journal of Physical Chemistry B. American Chemical Society, 2000. Vol. 104, № 33. P. 7923–7931.

204. Noskov B.A., Akentiev A. V., Miller R. Dynamic surface properties of poly(vinylpyrrolidone) solutions // J Colloid Interface Sci. 2002. Vol. 255, № 2. P. 417–424.

205. Pinaud F. et al. Adsorption of microgels at an oil-water interface: Correlation between packing and 2D elasticity // Soft Matter. 2014. Vol. 10, № 36. P. 6963–6974.

206. Chen S. et al. Incorporating Pendent Fullerenes with High Refractive Index Backbones: A Conjunction Effect Method for High Refractive Index Polymers // Macromolecules. 2015. Vol. 48, № 23. P. 8480–8488.

207. Lucassen J. Dynamic dilational properties of composite surfaces // Colloids and Surfaces. 1992. Vol. 65, № 2–3. P. 139–149.

208. Leahy B.D. et al. Geometric stability and elastic response of a supported nanoparticle film // Phys Rev Lett. 2010. Vol. 105, № 5. P. 8–10.

209. Kim K. et al. Governing factors in stress response of nanoparticle films on water surface // J Appl Phys. 2011. Vol. 110, № 10.

210. Razavi S. et al. Collapse of Particle-Laden Interfaces under Compression: Buckling vs Particle Expulsion // Langmuir. 2015. Vol. 31, № 28. P. 7764–7775.

211. Kosif I. et al. Robust Gold Nanoparticle Sheets by Ligand Cross-Linking at the Air-Water Interface // ACS Nano. 2017. Vol. 11, № 2. P. 1292–1300.

212. Ries H.E. Stable ridges in a collapsing monolayer // Nature. 1979. Vol. 281, № 5729. P. 287–289.

213. Vollhardt D. Nucleation in monolayers // Adv Colloid Interface Sci. 2006. Vol. 123–126, № SPEC. ISS. P. 173–188.

214. Lee K.Y.C. Collapse Mechanisms of Langmuir Monolayers // Annu Rev Phys Chem. 2008. Vol. 59, № 1. P. 771–791.

215. Bordács S., Agod A., Hórvölgyi Z. Compression of langmuir films composed of fine particles: Collapse mechanism and wettability // Langmuir. 2006. Vol. 22, № 16. P. 6944–6950.

216. Lenis J. et al. Mechanical Stability of Polystyrene and Janus Particle Monolayers at the Air/Water Interface // J Am Chem Soc. 2015. Vol. 137, № 49. P. 15370–15373.

217. Razavi S. et al. Impact of Surface Amphiphilicity on the Interfacial Behavior of Janus Particle Layers under Compression // Langmuir. 2019. Vol. 35, № 48. P. 15813–15824.

218. Garbin V. Collapse mechanisms and extreme deformation of particle-laden interfaces // Curr Opin Colloid Interface Sci. Elsevier Ltd, 2019. Vol. 39. P. 202–211.

219. Aveyard R. et al. Compression and structure of monolayers of charged latex particles at air/water and octane/water interfaces // Langmuir. 2000. Vol. 16, № 4. P. 1969–1979.

220. Prylutskyy Yu.I. et al. On the Origin of C60 Fullerene Solubility in Aqueous Solution // Langmuir. 2014. Vol. 30, № 14. P. 3967–3970.

221. Labille J. et al. Hydration and dispersion of C60 in aqueous systems: The nature of water-fullerene interactions // Langmuir. 2009. Vol. 25, № 19. P. 11232–11235.